

IMPORTANT NOTICE: The current official version of this document is available via the Sandia National Laboratories WIPP Online Documents web site. A printed copy of this document may not be the version currently in effect.

Sandia National Laboratories
Waste Isolation Pilot Plant (WIPP)
Test Plan (TP)

Iron and Lead Corrosion in WIPP-Relevant Conditions Test Plan TP 06-02

Rev. 3

Effective Date: January 26, 2016

Prepared by:
Charlotte Sisk-Scott
Jonathan Icenhower
Repository Performance Dept. 6932
Sandia National Laboratories
Carlsbad, NM

APPROVAL PAGE

Author:	<u>Original signed by Charlotte Sisk-Scott</u> Charlotte Sisk-Scott (6932)	<u>01/25/2016</u> Date
Author:	<u>Original signed by Jonathan Icenhower</u> Jonathan Icenhower (6932)	<u>1/25/2016</u> Date
Technical Reviewer:	<u>Original signed by Je-Hun Jang</u> Je-Hun Jang (6932)	<u>1/25/2016</u> Date
QA Reviewer:	<u>Original signed by Shelly R. Nielsen</u> Shelly R. Nielsen (6930)	<u>1-25-16</u> Date
Management Reviewer:	<u>Original signed by Christi Leigh</u> Christi Leigh (6932)	<u>1/25/2016</u> Date

TABLE OF CONTENTS

1 LIST OF FIGURES	5
2 LIST OF TABLES	6
3 DEFINITION OF ABBREVIATIONS AND ACRONYMS, AND INITIALISMS.....	7
4 REVISION HISTORY.....	9
5 PURPOSE AND SCOPE.....	10
6 INTRODUCTION	12
6.1 The Corrosion Process	13
6.2 Microbial Gases and Engineered Barrier Reactions in the WIPP.....	15
7 THERMODYNAMIC CALCULATIONS.....	17
7.1 Generalities	17
7.2 Fe Systems	19
7.2.1 Fe/H ₂ O System.....	20
7.2.2 Fe/H ₂ O/CO ₂ System.....	23
7.2.3 Fe/H ₂ O/H ₂ S System.....	24
7.2.4 Fe/H ₂ O/CO ₂ /H ₂ S System.....	26
7.3 Pb Systems.....	27
7.3.1 Pb/H ₂ O System	28
7.3.2 Pb/H ₂ O/CO ₂ System	29
7.3.3 Pb/H ₂ O/H ₂ S System.....	30
7.3.4 Pb/H ₂ O/CO ₂ /H ₂ S System.....	31
7.4 Summary of the Thermodynamic Calculations	31
7.5 Calculations Involving Microbial Gas Generation	33
7.5.1 Impact of Fe on Microbial Gases.....	33
7.5.2 Pb Impact on Microbial Gases.....	40
7.6 Summary of the Results of Interactions of Fe and Pb with Microbially Generated Gases	45
7.7 Additional Aspects on the Influence of Fe and Pb on the System.....	47
8 REVIEW OF DATA FOUND ON CORROSION IN THE WIPP.....	49
9 EXPERIMENTAL PROCESS DESCRIPTION.....	52
9.1 Materials	52
9.1.1 Alloys.....	52
9.1.2 Gas Composition.....	61
9.1.3 Presence of Organic Ligands in the Brine	62
9.2 Tasks List	63
9.2.1 Task 1: Brine Preparation	63
9.2.2 Task 2: Construction and Validation of a Mixed Flowing Gas Exposure System	66
9.2.3 Task 3: Software Qualification - Monitoring System and Software for the Mixed Flowing Gas Exposure System	73
9.2.4 Task 4: Evaluation of Carbonation of Fe in WIPP Internal Atmosphere and Likely Equilibrium Brines.....	75

9.2.5 Task 5: Evaluation of Carbonation of Pb in WIPP Internal Atmosphere and Likely Equilibrium Brines.....	76
9.2.6 Task 6: Systematic Evaluation of Fe Corrosion in Sulfide-Bearing Brines	76
9.2.7 Task 7: Determination of Fe Corrosion Products from Roselle (2013) Study	76
9.3 Test Matrix.....	77
9.3.1 General Environmental Parameters	77
9.3.2 Materials to be Evaluated.....	77
9.3.3 Atmosphere	78
9.3.4 Brine Compositions	78
9.3.5 Sample Positioning	78
9.3.6 Experimental design.....	79
9.3.7 Systematic Evaluation of Fe Corrosion in Sulfide-Bearing Brines	79
10 SAMPLE CONTROL – DATA QUALITY CONTROL	85
10.1 Sample Control	85
10.2 Data Acquisition Plan	85
10.3 Data Identification and Use	85
11 EQUIPMENT	86
11.1 Measuring and Test Equipment (M&TE).....	86
11.2 Weighing Equipment	86
11.3 Temperature Measuring Equipment	86
11.4 Liquid Measuring Equipment	86
11.5 Other Analytical Equipment	87
11.5.1 Ovens and Furnace.....	87
11.5.2 pH Meters and Autotitrators	87
11.5.3 Equipment for Chemical Analysis.....	87
11.5.4 Equipment for Mineralogical, and Textural Characterization	87
12 TRAINING	88
13 HEALTH AND SAFETY	89
13.1 Electrical	89
13.2 Chemical	89
13.2.1 General Chemical Compounds	89
13.2.2 Inert Gases	89
13.2.3 Hydrogen Sulfide.....	90
13.3 Thermal.....	93
13.4 Pressure.....	94
13.5 Readiness Review	94
14 PERMITTING/LICENSING	95
15 REFERENCES	96

1 LIST OF FIGURES

Figure 1. Simplified view of the anodic and potential cathodic reactions for the corrosion process.....	14
Figure 2. Pourbaix Diagram for the Fe System.....	23
Figure 3. N ₂ gas circuit for the gas exposure system. This circuit includes the wet N ₂ streams (top portion) as well as the dry N ₂ streams. Also shown are two O ₂ traps – a large capacity trap in the main supply line, and an indicating trap in one of the wet supply lines.	69
Figure 4. Contaminant gas streams for the gas exposure system. Upper portion of the figure illustrates the CO ₂ supply (equipped with O ₂ traps similar to those described above). The lower portion illustrates the H ₂ S gas supply system – note that the supply gas for this leg is dry N ₂ and as illustrated in Figure 2.	70
Figure 5. Schematic representation of the gas flow streams passing into each of the four exposure chambers.	71
Figure 6. Schematic representation of the gas composition analysis system. This system consists of a series of perma-pure gas dryers, a gas manifold (controlled by solenoid valves) to route the gas to each analyzer, and the two gas analyzers themselves.....	72

2 LIST OF TABLES

Table 1. Abbreviations, Acronyms, and Initialisms.	7
Table 2. Standard Free Energies Selected by Brush (1990) and Chivot (2004).	20
Table 3. Free Energies Selected by the USGS (1995) and Chivot (2004).	28
Table 4. Result Summaries for Fe-Gas Reactions With the Denitrification And Sulfate Reduction Processes, but Without Methanogenesis.	35
Table 5. Summary of the Results for Fe-Gas Reactions With Denitrification, Sulfate Reduction, and Methanogenesis Processes, Case 1.	37
Table 6. Summary of Results for Fe-Gas Reactions with the Denitrification, Sulfate Reduction, and Methanogenesis Processes, Case 2.	39
Table 7. Summary of the Result of Pb-Gas Reactions with Denitrification and Sulfate Reduction Processes, and Without Methanogenesis.	41
Table 8. Result Summaries for Pb-Gas Reactions With Denitrification, Sulfate Reduction, and Methanogenesis Processes, Case 1.	43
Table 9. Result Summaries for Pb-Gas Reactions with Denitrification, Sulfate Reduction, and Methanogenesis Processes, Case 2.	45
Table 10. Percentage of Carbon Involved in the Microbial Gas Generation Reactions and Moles of Gases Generated from the Reactions between Metallic Fe and Pb and the Microbially Generated Gas.	47
Table 11. Materials of Construction for the Various Waste Containers.	53
Table 12. Material Compositions Defined by ASTM Specifications (all compositions in wt %).	56
Table 13. ASTM Specifications.	59
Table 14. Size and Number of the Pb-Lined Containers.	60
Table 15. Concentrations of Organic Ligands for a Homogeneous 10-Panel Repository.	63
Table 16. Compositions of GWB and ERDA-6 Prior to Equilibration with MgO.	64
Table 17. Compositions of GWB and ERDA-6 after Equilibration with MgO, in the Presence of Organic Ligands (Brush, 2005).	65
Table 18. Solubility of H ₂ S in NaCl Solutions.	79
Table 19. Henry's Law Constants.	80
Table 20. Experimental Test Matrix.	85
Table 21. Symptoms Observed after Different H ₂ S Exposure.	92

3 DEFINITION OF ABBREVIATIONS AND ACRONYMS, AND INITIALISMS

Table 1 defines the abbreviations, acronyms, and initialisms used within this Test Plan (TP).

Table 1. Abbreviations, Acronyms, and Initialisms.

Abbreviation or Acronym	Definition
ACGIH	American Conference of Governmental Industrial Hygienists
ASTM	American Society for Testing and Materials
CO ₃ ²⁻	carbonate ion
CH	contact handled
CH ₄	methane
CPR	cellulosic, plastic, and rubber
CO ₂	carbon dioxide
DOE	Department of Energy
EDTA	ethylenediaminetetraacetic acid
ERDA-6	Energy Research and Development Administration (WIPP Well) 6. Synthetic Castile Formation brine
ES&H	Environmental Safety and Health
Fe	elemental (metallic) iron
FMT	Fracture-Matrix Transport, a geochemical speciation and solubility code
GWB	Generic Weep Brine, a synthetic Salado Formation brine.
H ₂	hydrogen gas
H ₂ S	hydrogen sulfide
HSLA	high-strength, low-alloy
ICP-OES	Inductively-coupled plasma-optical emission spectrometer
LC50	Lethal concentration for 50% of humans
m	molal (mol/kg)
M	molar (mol/L)
M&TE	measuring and test equipment

Table 1. Abbreviations, Acronyms, and Initialisms. (cont.)

Abbreviation or Acronym	Definition
MSDS	Material Safety Data Sheet
N ₂	nitrogen gas
NHE	normal hydrogen electrode
NP	(SNL WIPP) Nuclear Waste Management (QA) Procedure
O ₂ (g)	oxygen gas
OSHA	Occupational Safety and Health Administration
PA	performance assessment
Pb	elemental lead
PEL	permissible exposure limit
Pu	plutonium
QA	quality assurance
PABC	(WIPP) performance assessment baseline calculations
PPE	personal protection equipment
RH	remote handled
sccm	Standard cubic centimeters per minute (i.e., milliliters per minute)
SNL	Sandia National Laboratories
SOP	Standard Operating Procedure
SP	(SNL WIPP) Activity/Project Specific Procedure
S ²⁻	sulfide ion
TP	test plan
TVL	Threshold Limit Value
TRU	Transuranic
WIPP	Waste Isolation Pilot Plant
XRD	X-ray diffractometer

4 REVISION HISTORY

This is the third revision of this TP. The work performed on the Pb samples pertaining to corrosion in the presence of CO₂(g) is considered finished and no further work will be performed. However, this revision includes the completion of characterizing the Fe corrosion samples relevant to experiments previously performed under the original TP 06-02 by Roselle (2013).

The second revision (2015) addresses a change in methodology for determining the dissolution kinetics of iron under anoxic conditions. That revision also maps out a new approach for quantifying the effects of sulfide on iron corrosion.

The first revision includes a detailed section addressing the Environmental Safety and Health (ES&H) concerns that this work might raise.

Subsequent versions will be prepared in accordance with the following Sandia National Laboratories (SNL) Waste Isolation Pilot Plant (WIPP) Quality Assurance (QA) Procedures: NP 6-1, NP 6-2, and NP 20-1 (Subsection 5.2).

5 PURPOSE AND SCOPE

This document describes the experimental work that will be performed to assess the corrosion behavior of carbon steel and lead (Pb) alloys used to contain contact handled (CH) and remote handled (RH) waste under WIPP-relevant conditions. More specifically, the objective is to determine to what extent the aforementioned materials consume carbon dioxide (CO₂) through the formation of carbonates, potentially supporting magnesium oxide (MgO) in its role of CO₂ sequestration; MgO is the WIPP engineered barrier, chosen to mitigate the effect of microbial CO₂ generation on actinide mobility in a post-closure repository environment and to buffer brine pH at a moderately basic level, thus minimizing the solubilities of actinides in WIPP brines. Furthermore, the rate at which the waste-container materials consume other microbially-produced gasses, such as hydrogen sulfide (H₂S), within the post closure WIPP environment will also be explored. The design of the overall test system, as well as the applicable calculations (brine composition, likely corrosion product compositions, etc.) are also presented.

The work proposed in this document can be loosely broken down into four stages. The first stage will be the acquisition, assembly, and calibration of the equipment as well as the production of the software interface necessary to conduct the test themselves. This is anticipated to take three months, barring any unanticipated delays. The second stage of the work is the execution of the experiments defined in this document, and will continue for a period of two years. The third stage will be to qualitatively identify the corrosion reaction products of low carbon steel in an anoxic environment by examining Roselle's coupons. This is projected to be completed within six months. The analysis and official documentation of the results will be the fourth and final stage of the program. In this portion, the quantity and nature of any carbonates which form, along with the general electrochemical behavior of each material will be documented. A final report will be generated and submitted to DOE at the end of this stage, which is anticipated to take approximately 3 months. Once complete, the results of this study will provide considerable insight into the extent to which the metals within the WIPP (specifically iron and lead) might augment the actions of the engineered barrier through the consumption of carbon dioxide.

The purpose of this revision is to continue and augment the work begun by Natalie Wall and Greg Roselle (e.g., Roselle, 2009; 2010; 2011a, 2011b) in quantifying the dissolution and reaction of low carbon steel in an anoxic environment with solutions containing HS⁻ and NaCl. A large volume of data has already been collected and reported (e.g., Roselle, 2009; 2009; 2010; 2011a, 2011b) and the additional experiments described herein are meant to complete the objectives laid out in the original version of TP 06-02, but with some modifications to the experiments. The data collected and reported in Roselle (2009; 2010; 2011a, 2011b) pertained to the anoxic dissolution of Fe and Pb in the presence of CO₂. Because of the thoroughness of these experiments, we will not attempt to reproduce prior data. Rather, the modifications described below are designed to more effectively determine the dissolution rate of low carbon steel in aqueous solution over an ionic strength and a_{HS⁻} interval. Experiments will be performed in an anoxic glove box over a temperature interval (25 to 90 °C). A greater emphasis on characterization of the starting steel coupons will also be enacted. The corrosion products in Roselle's experiments have also not been completely identified, and therefore further investigation of those steel coupons is warranted. Roselle's study on steel coupons provided an

updated H₂ gas generation rate and show formation of several phases dependent on the partial pressure of CO₂ (P_{CO_2}). Scanning electron microscope (SEM) analysis with energy dispersive spectroscopy (EDS) showed the presence of a green Fe (\pm Mg) chlorhydroxide phase at P_{CO_2} values $<10^{-2.82}$ atm. At higher P_{CO_2} , the dominant corrosion product was a Fe-Mg-Ca hydroxycarbonate phase. In the analysis, Roselle (2013) expanded his conclusions saying: “It is possible that other corrosion products (e.g., green rust, hibbingite, etc.) may also form (Nemer et al., 2011).” Unfortunately, no further characterization of Roselle’s corrosion products was carried out. And even though SEM/EDS is an extremely useful tool in identifying corrosion products, phase identification by SEM/EDS is difficult, because identity can be based only on morphological observations. On the other hand, use of Energy Dispersive Spectrometry (EDS) coupled with analyses using X-ray diffraction (XRD), UV-Vis, Electron Probe Microbe Analysis (EPMA) Mossbauer and/or Raman Spectroscopy will be able to determine the extent of corrosion products formed. Therefore, corrosion products can be identified by utilizing multiple complementary techniques. This information will then be used to formulate the appropriate corrosion reactions for iron.

The data produced in these experiments will be used to more effectively model the generation of gases in the repository and to identify potential effects of steel corrosion on the mobility of radionuclide elements.

Because of the newly-placed emphasis on anoxic corrosion in the presence of sulfide described in this revision (Rev. 2), much of what was described in the earlier versions can be considered as obsolete. We will not, for example, use the apparatus described in Task 2 (Section 9.2.2) to test the corrosion resistance of Fe. Furthermore, the discussion of iron solubility (Section 7.2; Fe systems) refers to thermodynamic databases that have been replaced by a newer one (NEA, 2013). Thus, the discussion of Fe solubility and the choice of which thermodynamic database to use is also obsolete, but is retained for illustrative purposes. Finally, at the first writing of this Test Plan (Rev. 0), very little was known about the important corrosion product, “green rust”, a double-layered oxyhydroxide that contains water, carbonate and variable Fe³⁺/Fe²⁺. Since this earlier writing, the importance of green rust is now understood, and in this revision, the role played by this phase in corrosion of steel is discussed. A more up-to-date Pourbaix diagram for iron is presented that contains a stability field for green rust.

6 INTRODUCTION

The WIPP is a repository for transuranic (TRU) wastes, located within the bedded salts of the Permian Salado Formation, southern New Mexico. This formation consists of an interbedded halite-and-anhydrite formation overlaying the Castile Formation. The repository will consist of eight seven-room panels upon completion. Additionally, there are two access drifts in the waste region that will also be available for waste disposal and will constitute two supplementary panels. The WIPP performance assessment (PA) analyzes the performance of the repository, including the consequences of future inadvertent human intrusions into the repository by drilling for resources; such intrusions could lead to a postulated release of radionuclides to the accessible environment before the end of the 10,000-year regulatory period. To accomplish this, the U.S. Department of Energy (DOE) has examined different drilling scenarios, which involve the penetration of the repository by one or more drill holes; some of the scenarios also involve the possibility of the penetration of a pressurized Castile brine reservoir (U.S. DOE, 2004, Chapter 6). The estimated quantity of radionuclides released to the accessible environment following penetration of the repository depends on the chemistry of these radioelements. As an example, consider plutonium (Pu), which is less soluble when it speciates in lower oxidation states, such as Pu(III) and Pu(IV), than in higher oxidation states, such as Pu(VI). Thus it follows that in order to minimize the release of such radionuclides from the repository, it is desirable to maintain all such species in their least-soluble form (i.e., low oxidation states). It is also advisable to understand the role played by pH in the repository.

The nature of the environment within the WIPP following closure will, to a large extent, control the speciation of the radionuclides within the waste. More specifically, there are components contained within the waste that can impact the oxidative or reductive nature of the environment, such as the metals undergoing active corrosion. If the metals undergo active corrosion within the WIPP, the corrosion process will serve to maintain electrochemically reducing conditions. The predominant metals within the WIPP will be iron (Fe) and Pb, present within the waste itself, as well as the containers used to hold the waste until emplacement. The current inventory predicts that 280 and 599 kg/m³ of Fe and Fe-base alloys will be present in the contact handled (CH) and remote handled (RH) wastes, respectively. Also, 0.013 and 420 kg/m³ of Pb will be present in the CH and RH wastes, respectively. The corrosion behavior of these materials, specifically the kinetics of the corrosion reaction, will be controlled by the availability of water (in brine) at the metal surface, as well as the internal atmosphere within the WIPP. It should be noted that if the corrosion process is stifled, for example due to passivation of the metal surfaces, electrochemically reducing conditions will no longer be maintained by the corrosion process.

In addition to Fe and Pb, the waste disposed within the WIPP contains significant quantities of cellulosic, plastic, and rubber (CPR) materials. With time, microbial activity may consume some portion of the CPR materials, resulting in the generation of significant quantities of CO₂, H₂S, hydrogen (H₂), nitrogen (N₂), and methane (CH₄). Some of these gasses, namely CO₂ and H₂S, may interact with the metallic Fe and Pb, altering their electrochemical behavior. Elevated concentrations of both gasses have been demonstrated to passivate Fe under certain conditions (Telander and Westerman, 1993; 1997). If the Fe and Pb within the WIPP passivate, they will no longer contribute to maintaining the reducing environment within the WIPP through

the corrosion process. Under these conditions, Fe and Pb would not be available to prevent oxidation of the radionuclides, although other reductants may still be available.

The sections below provide a brief introduction to the corrosion process, as well as detail the potential microbial activity and reaction pathways within the WIPP.

6.1 The Corrosion Process

Corrosion is the destructive attack of a metal by chemical or electrochemical reaction with its environment. (For a more complete discussion, see Uhlig and Revie, 1985) In this study, we are concerned with the corrosion of Fe- and Pb-base alloys under WIPP-relevant environmental conditions. More specifically, this study will focus on the products of the corrosion process and their implications for the TRU components within the waste. This section will provide a very basic description of the corrosion process. A more complete discussion is beyond the scope of this section, but can be found in the text referenced above.

Broadly speaking, the corrosion reaction may be broken down into two components: the anodic reaction (oxidation) and the cathodic reaction (reduction). The anodic reaction is typically metal oxidation, while the cathodic reaction can include processes such as oxygen (O₂) reduction, water reduction, etc. An important concept here is that the sum of all the anodic reactions (i.e., total oxidative current) must be equal to the sum of all cathodic reactions (i.e., total reductive current); changes in one will have an equal impact on the other. As an example, consider the transition from an O₂-containing environment to one where O₂ has been depleted. In an O₂-rich environment, the cathodic reaction is typically O₂ reduction:



If the total supply of O₂ is limited (as will be the case in the WIPP upon closure), O₂ will become depleted with time, and thus the rate of the reaction will become concentration limited, eventually becoming negligible in magnitude. At this point, if no other viable cathodic reactions were available, the anodic reaction would also stop, as there would be no cathodic reaction to support it. However, in an aqueous environment, there are other cathodic reactions that could take place, such as water reduction;



This transition from O₂ reduction as the primary cathodic reaction to water reduction as the O₂ concentration is depleted is illustrated in Figure 1. Three reactions are shown in the figure, the anodic reaction (metal oxidation), expressed as:



and the two cathodic reactions we are concerned with here, O₂ reduction and water reduction. As the rate of the reaction increases, O₂ reduction transitions from a charge transfer-controlled reaction to a mass transport-controlled process; its maximum rate is limited by how quickly dissolved O₂ can get to the metal surface. (i.e., as the cathodic overpotential is increased, the rate of O₂ reduction cannot similarly increase, as it is already consuming all of the dissolved O₂ as it

reaches the metal surface). As the O₂ concentration decreases, so does the limiting current density for the O₂ reduction.

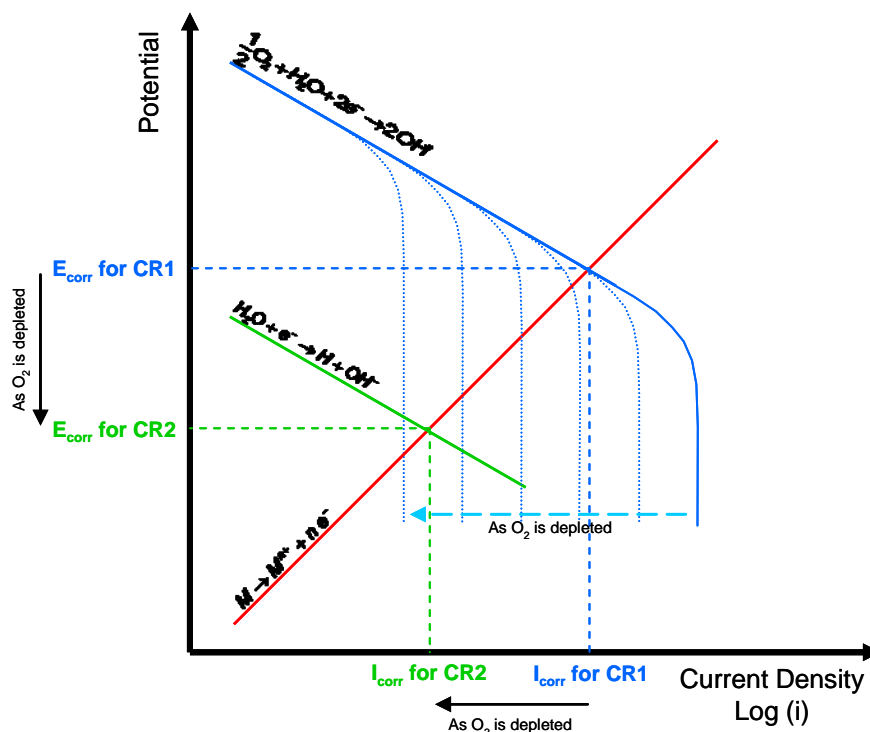


Figure 1. Simplified view of the anodic and potential cathodic reactions for the corrosion process.

As discussed above, the total anodic rate will be equal to the total cathodic rate. In the figure, that rate is the point at which the anodic and cathodic curves cross. (Note that the anodic and cathodic electrode areas are important here, as the total current is equal to the total active area for each process multiplied by the current density) In the figure, the rate of the cathodic and anodic reactions will initially be equal to the value of I_{corr} for CR1. As the O₂ concentration decreases, the limiting current for O₂ reduction decreases, resulting in the shift shown in the figure. Eventually, another cathodic reaction (in this case, water reduction) can become thermodynamically viable, and it will then dictate the total anodic and cathodic reaction rates (indicated by I_{corr} for CR2).

In the context of this study, a number of other cathodic reactions may become operative. Due to the potential for an elevated concentration of CO₂, another potential cathodic reaction is the direct oxidation of H through the H₂CO₃/HCO₃⁻ equilibrium:



It has also been suggested that in CO₂ solutions at elevated pH (i.e., >5), the direct oxidation of the hydrogen ion through the HCO₃⁻/CO₃²⁻ equilibrium could become important (Nordsveen, 2003):



Furthermore, the presence of CO_2 in significant quantities can also result in the formation of iron carbonate ($\text{FeCO}_3(\text{s})$) through the reaction:



If the FeCO_3 forms as a sufficiently dense film on the Fe surface, it could potentially result in passivation. However, as will be illustrated below in section 7.2.4, the presence of H_2S which will likely accompany the CO_2 (see section 6.2 below) will tend to destabilize this film, preventing passivation due to carbonate formation.

There are a number of factors that will impact the rate and overall nature of the corrosion process. As with chemical reactions, electrochemical reactions are impacted by the environmental conditions under which they take place. These include the local environment at the metal-solution interface (i.e., composition, pH, etc.), temperature, availability of O_2 or other reducible species, etc. The effects of temperature, pH and concentration of sulfide on the corrosion rate of steel are addressed in this latest revision (Rev. 2) of the Test Plan.

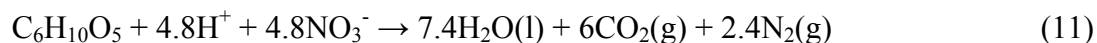
In the sulfide-bearing system, the partial pressure of hydrogen gas that will be produced will depend upon which iron sulfide phase forms during the corrosion process:



where Fe^0 represents steel, $\text{FeS}(\text{s})$ mackinawite, $\text{FeS}_2(\text{s})$ pyrite or marcasite, $\text{Fe}_3\text{S}_4(\text{s})$ greigite and $\text{Fe}_7\text{S}_8(\text{s})$ pyrrhotite. For every mole of Fe^0 consumed, between 1 and 2 moles of $\text{H}_2(\text{g})$ are produced. Although mackinawite or its amorphous equivalent typically precipitate in steel corrosion experiments in the presence of sulfide, it is clear that this phase is not the thermodynamically stable phase. A number of investigators have documented that mackinawite transforms over time to troilite (hexagonal FeS) and pyrite (FeS_2) (e.g., Bai et al., 2014). At relatively high pH values (>7), the stable phase in anoxic conditions is Fe_7S_8 , or pyrrhotite. From the standpoint of the experiments discussed in this revision, it is imperative to know which phase is stable in order to model the partial pressure of $\text{H}_2(\text{g})$ in the repository.

6.2 Microbial Gases and Engineered Barrier Reactions in the WIPP

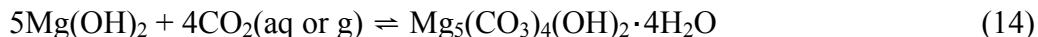
Microbial activity, if it occurs to a significant extent in the WIPP, will consume CPR materials by one or more of the following reactions (Brush, 1990; Francis and Gillow, 1994; Brush, 1995; Wang and Brush, 1996; Francis and Gillow, 1997):





As a result of microbial activity via these reactions, significant quantities of gases could be generated - in particular $\text{CO}_2(\text{g})$.

The microbially generated $\text{CO}_2(\text{g})$ will then react with the MgO , the WIPP engineered barrier. Laboratory and modeling studies have shown that the carbonation reaction (Equation (10)) of MgO will buffer f_{CO_2} at a value of $10^{-5.50}$ atm in WIPP brines (DOE, 2004, Appendix BARRIERS), where $\text{Mg}(\text{OH})_2$ is the main hydration product of the mineral periclase (MgO) expected in the WIPP and $\text{Mg}_5(\text{CO}_3)_4(\text{OH})_2 \cdot 4\text{H}_2\text{O}$ is the form of the mineral hydromagnesite predicted by the repository models.



Moreover, the brucite-dissolution reaction, described in Equation (11), will buffer pH in the WIPP at a value of 8.69 in Generic Weep Brine (GWB) and 9.02 in Energy Research and Development Administration (WIPP Well) 6 Synthetic Castile Formation brine (ERDA-6), where ERDA-6 represents fluids from reservoirs in the Castile Formation and GWB represents intergranular brines from the Salado Formation at or near the stratigraphic horizon of the repository. (DOE, 2004, Appendix BARRIERS)



The large quantities of Fe and Pb present in WIPP may also contribute to the consumption of the microbially generated gases, primarily through the formation of carbonates (CO_3^{2-}) and sulfides (S^{2-}). After the limited concentration of O_2 trapped within the repository at the time of closure is depleted via the corrosion process and the aerobic microbial consumption of CPR materials, anoxic corrosion of Fe and Pb will occur (Brush, 1990). WIPP-specific experiments (Telander and Westerman, 1993; 1997) verified Brush's (1990) hypothesis that carbon steels will corrode under such conditions. A more thorough discussion of their results, along with several similar studies, is presented in Section 8 of this document.

7 THERMODYNAMIC CALCULATIONS

In the following sections, a series of thermodynamic calculations are performed to assess the potential Fe and Pb compounds that might form under WIPP-relevant conditions. Following the thermodynamic calculations is a discussion of their implications in terms of interactions of both Fe and Pb with the gas compositions likely to result from microbial activity within the WIPP.

A number of key assumptions were made prior to conducting these calculations. First, these calculations illustrate the phases that are most stable thermodynamically; they provide no information on the kinetics of the formation process or the formation of any metastable phases produced prior to the potential conversion to the most thermodynamically stable state (i.e., reaction pathways other than direct production of the most thermodynamically stable state). In addition, for simplicity, all of these calculations were performed assuming that the environment was essentially pure water with only the reactive species of interest (i.e., carbon and sulfur) being present. As such, they may or may not indicate what might exist within a brine, which will contain, among other things, up to 5 M chloride. It is possible that the impact of the omitted species will dominate the actual behavior of the system, rendering the results discussed below partially or completely invalid. Thus it is critical that the reader understand that the calculations made in the following sections only provide an indication as to whether or not something might happen; they are not conclusive evidence that a given phase, such as FeCO_3 , will or will not form.

7.1 Generalities

The chemical equilibrium, in which b mol of B reacts with c mol of C to produce d mol of D and e mol of E is expressed as Equation (12):



Phase designators immediately follow the chemical formula and appear in parenthesis: (l) for liquid, (aq) for aqueous, (g) for gas, and (s) for solid. The designators “cr” and “am” are used for solid in crystalline and amorphous phases, respectively.

The thermodynamic equilibrium constant of reaction 12 is expressed as:

$$K = \frac{\{D\}^d \times \{E\}^e}{\{B\}^b \times \{C\}^c} \quad (17)$$

where $\{X\}$ is the activity of X and is expressed as:

$$\{X\} = [X] \times \gamma_X \quad (18)$$

where $[X]$ is the concentration of X and γ_X the activity coefficient of X.

Equilibrium constants involving a solid compound as the reactant and nonsolid species as products are denoted as solubility products. An example of such an equilibrium and its associated solubility product are presented below:



The term “standard state,” often used in thermodynamics, defines a baseline of behaviors. The standard state pressure is 1 atm. The standard state of a gaseous substance is defined as the pure gaseous substance at the standard-state pressure, in which it behaves as an ideal gas; for a liquid, it is the pure liquid at the standard-state pressure; for a solid, it is the pure solid at the standard-state pressure; and for a solute X in solution, it is a liquid solution at the standard-state pressure and in which the molality of X is 1 mol of solute per kg of solvent and its activity coefficient is 1.

The standard free energy of a chemical reaction is the difference between the sum of the free energies of formation of the products in their standard states and the sum of the free energies of formation of the reactants in their standard states:

$$\Delta G_R^0 = \Delta G_f^0 \text{ products} - \Delta G_f^0 \text{ reactants} \quad (20)$$

The standard free energy of the equilibrium is also related to the thermodynamic equilibrium constant, as shown in the following equation:

$$\Delta G_R^0 = -R \times T \times \ln(K) = -R \times T \times \ln(10) \times \log(K) \quad (21)$$

where R is the gas constant (8.3145 J/mol K) and T the absolute temperature.

Redox reactions are usually expressed in terms of their electrode (half-cell) potential E_h , given as reduction potentials relative to the standard hydrogen electrode. The standard electrode potential E_h^0 is the potential relative to the standard hydrogen electrode, when all the components are in their respective standard state. The general equation for a half-cell reaction:



where O and R are the oxidized and reduced species of a specific entity, respectively (e.g. Fe(III) vs. Fe(II)) and n is the number of electrons involved in the reaction. The Nernst equation is the expression of the electrochemical potential of the redox reaction:

$$E_h = E_h^0 + \frac{R \times T}{n \times F} \times \ln \left(\frac{\{R\}^r \times \{C\}^c}{\{O\}^o \times \{B\}^b} \right) \quad (23)$$

where F is the Faraday constant, 96485 C/mol. E_h may also be expressed as a function of the free energy of the thermodynamic equilibrium:

$$E_h = -\frac{\Delta G_R}{n \times F} \quad (24)$$

Visualization of the region of predominance for the different species of a system is quite important to predict the species encountered at specific conditions. A plot of the electrochemical potential of the chemical, electrochemical, and redox reactions as a function of pH, commonly referred to as a Pourbaix diagram, allows the prediction of the most thermodynamically stable species as a function of the electrochemical conditions that exist within the system. Note, however, that this diagram is based entirely on thermodynamic data, and as such does not provide any kinetic information (e.g., rates of reaction, presence of metastable phases, etc.) Several examples of Pourbaix diagrams are presented throughout this document. As each of the chemical and electrochemical reactions represented on the diagram are a function of concentration, for all instances in this paper they will be presented at a concentration of 10^{-6} M.

7.2 Fe Systems

Metallic Fe will oxidize in water at 25 °C and 1 atm. This oxidation results in the formation of a number of solid corrosion products, including $\text{Fe(OH)}_2(\text{s})$, $\text{Fe(OH)}_3(\text{s})$, $\text{Fe}_2\text{O}_3(\text{s})$, and $\text{Fe}_3\text{O}_4(\text{s})$. In solution, Fe typically exhibits two oxidation states, Fe(II) (ferrous) and Fe(III) (ferric). The standard potential for the couple $\text{Fe}^{2+}/\text{Fe}^{3+}$ is 0.771 V.

Brush (1990) conducted a series of thermodynamic calculations and estimated the amount of gas generated by the corrosion of Fe by H_2O , CO_2 , and H_2S . In the following text, his results are compared to similar calculations performed using Chivot's (2004) selection of thermodynamic data. Because of the reducing conditions within the WIPP, only the thermodynamic functions of Fe(II) will be considered. The standard free energies of formation selected by Brush (1990) and Chivot (2004) are included in Table 2. All values are expressed in kJ/mol (where 1 kJ/mol is equivalent to 4.184 J/cal.)

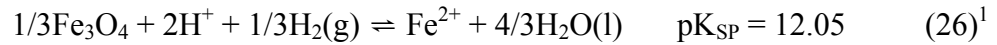
Table 2. Standard Free Energies Selected by Brush (1990) and Chivot (2004).

Compound	ΔG_f^0 selected by Brush (1990) (kcal/mol)	ΔG_f^0 selected by Brush (1990) (kJ/mol)	ΔG_f^0 selected by Chivot (2004) (kJ/mol)
H ₂ O(l)	-56.6781	-237.1	-237.140
H ₂ (g)	0	0	0
H ⁺	0	0	0
CO ₂ (g)	-94.2579	-394.4	-394.373
H ₂ S(g)	-8.017	-33.54	-33.44
Fe(s)	0	0	0
Fe ₃ O ₄ (s)	-242.0091	-1012	-1013.73
Fe(OH) ₂ (s)	-116.3	-486.6	-491.96
FeCO ₃ (s)	-159.345	-666.7	-680.076
FeS ₂ (s)	-38.2956	-160.2	-156.17
FeS(am)	-	-	-95.17
FeS(s, troilite)	-	-	-101.954

7.2.1 Fe/H₂O System

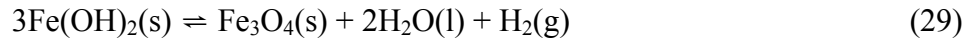
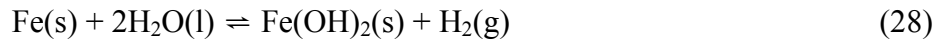
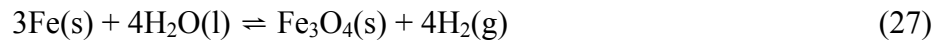
As explained by Brush (1990), two possible anoxic corrosion products of metallic Fe in the absence of CO₂ are Fe₃O₄ and (Fe,Mg)(OH)₂. Chivot (2004) selected the following solubilities for these materials:





Fe_3O_4 , which contains both ferric and ferrous species ($\text{Fe(II)Fe}_2\text{(III)O}_4$), is the stable Fe corrosion product encountered. It can be obtained by oxidation of $(\text{Fe,Mg})(\text{OH})_2$, Fe oxidation by water vapor, or through the reduction of $\gamma\text{FeOOH}(\text{s})$. $\text{Fe}(\text{OH})_2(\text{s})$ is a pale green (crystalline) or white (amorphous) solid obtained by preparing a basic Fe solution in the total absence of O_2 .

Brush (1990) calculated the amount gas generated from the formation of $\text{Fe}_3\text{O}_4(\text{s})$ and $\text{Fe}(\text{OH})_2(\text{s})$ via the following equilibria:



The free energy of the chemical equilibria (23), (24), and (25) can be expressed as:

$$\Delta G_{23}^0 = -2.303 \times R \times T \times \log \left(\frac{\{\text{Fe}_3\text{O}_4(\text{s})\} \times f_{\text{H}_2}^4}{\{\text{Fe}(\text{s})\}^3 \times \{\text{H}_2\text{O}(\text{l})\}^4} \right) \quad (30)$$

$$\Delta G_{24}^0 = -2.303 \times R \times T \times \log \left(\frac{\{\text{Fe}(\text{OH})_2(\text{s})\} \times f_{\text{H}_2}}{\{\text{Fe}(\text{s})\} \times \{\text{H}_2\text{O}(\text{l})\}^2} \right) \quad (31)$$

$$\Delta G_{25}^0 = -2.303 \times R \times T \times \log \left(\frac{\{\text{Fe}_3\text{O}_4(\text{s})\} \times \{\text{H}_2\text{O}(\text{l})\}^2 \times f_{\text{H}_2}}{\{\text{Fe}(\text{OH})_2(\text{s})\}^3} \right) \quad (32)$$

Using $\{\text{Fe}_3\text{O}_4(\text{s})\} = \{\text{Fe}(\text{OH})_2(\text{s})\} = \{\text{Fe}(\text{s})\} = 1$, $\{\text{H}_2\text{O}(\text{l})\} = 0.7$ (the activity of water in a WIPP brine), and Brush's selection of free energies presented in Table 2, the chemical equilibria (23) and (24), which describe the formations of $\text{Fe}_3\text{O}_4(\text{s})$ and $\text{Fe}(\text{OH})_2(\text{s})$ from the anoxic corrosion of $\text{Fe}(\text{s})$ by $\text{H}_2\text{O}(\text{l})$, H_2 fugacities of about 447 and 71 atm are obtained, respectively. However, the formation of $\text{Fe}_3\text{O}_4(\text{s})$ through conversion of $\text{Fe}(\text{OH})_2(\text{s})$ yields a much larger H_2 fugacity of 10^5 atm. The same calculations conducted with the free energies selected by Chivot

¹ In a reducing environment

(2004), presented in Table 2 yield H_2 fugacities of 503, 616, and 273 atm, for the equilibria (23), (24), and (25), respectively.

The vast difference in the calculated fugacities for the equilibria involving $Fe(OH)_2(s)$ (71 versus 616 atm, for Equation (27) and 10^5 versus 273 atm, for Equation (28)) is due to the high sensitivity of the calculation to the value selected for the standard free energy of formation of $Fe(OH)_2(s)$, $\Delta G_{f(Fe(OH)_2(s))}^0$. Brush selected the value of $\Delta G_{f(Fe(OH)_2(s))}^0$ from Wagman et al. (1969). However, Chivot had access to 10 data published between 1952 and 1999; he rejected four of them on a technical basis and calculated his selected value based on the $Fe(OH)_2(s)$ standard enthalpy of formation, $\Delta H_{f(Fe(OH)_2(s))}^0$ and standard entropy, $\Delta S_{f(Fe(OH)_2(s))}^0$ published by Chase (1998). It is difficult at this point to favor one database over the other, as small variations in $\Delta G_{f(Fe(OH)_2(s))}^0$ have a large effect on the calculated H_2 fugacity. However, the $\Delta G_{f(Fe(OH)_2(s))}^0$ values published after 1990 are consistently smaller than the one published prior to 1990: the average is -493 ± 10 kJ/mol (or -490 ± 6 kJ/mol without the data rejected by Chivot) versus -484 ± 3 kJ/mol, which suggests that the data available in 1990 for $\Delta G_{f(Fe(OH)_2(s))}^0$ were slightly overestimated. Consequently, we favor the Chivot's database versus Brush's.

Chivot constructed the Pourbaix diagram for a Fe/H_2O system at $25^\circ C$, containing 10^{-6} m of dissolved Fe (Chivot, 2004, Figure 7). Under such conditions and at pH 9, $FeOOH(s)$, Fe_3O_4 , and $Fe(s)$ are the solid stable phases for potentials (relative to the normal hydrogen electrode (NHE)) higher than $-0.35 V_{NHE}$, between -0.35 and $-0.50 V_{NHE}$, and lower than $-0.50 V_{NHE}$, respectively. The dissolved species are $Fe(OH)_3^0$ and $Fe(OH)_4^-$, for a positive potential and Fe^{2+} for a negative potential.

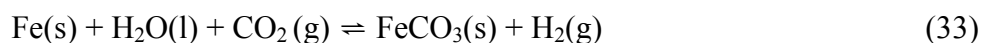
A Pourbaix diagram, based on a more current set of thermodynamic data (i.e., post Chivot, 2004), is shown in Figure 2 below (from Jové-Colón et al., 2014). In previous thermodynamic databases, phases such as magnetite (Fe_3O_4), and $Fe(OH)_2$ had large stability fields in the lower right-hand side of the diagram. Note, however, that the stability field for green rust takes up this part of the diagram. As previously mentioned, green rust refers to a series of carbonate-bearing hydrated double-layer oxyhydroxide minerals whose composition varies with the ferric-ferrous ratio. Thus, there is a complete solid solution between fougèrite $[Fe^{2+}_4Fe^{3+}_2(OH)_{12}][CO_3] \cdot 3H_2O$ and mössbauerite $[Fe^{3+}_6O_4(OH)_8][CO_3] \cdot 3H_2O$.

In the present case, we are concerned with reactions that take place under anoxic conditions in the presence of sulfide. The relevant Pourbaix diagram for these conditions can be found in Barnes and Langmuir (1978). For condition in which we will run our experiments, the relevant phases will be FeS_2 (pyrite or marcasite) or Fe_7S_8 . The latter phase is also designated as $Fe_{1-x}S$ ($x = 0.0$ to 0.2) and is known to mineralogists as pyrrhotite. The stability fields for the iron sulfides run parallel to the lower water stability field on the low E_h side of the diagram and likely supplant the stability field for green rust.

In this revision, we consider the reactions that take place at 90 °C. Accordingly, we will construct a Pourbaix diagram of the relevant reactions at 90 °C and compare the results to those obtained at 25 °C.

7.2.2 Fe/H₂O/CO₂ System

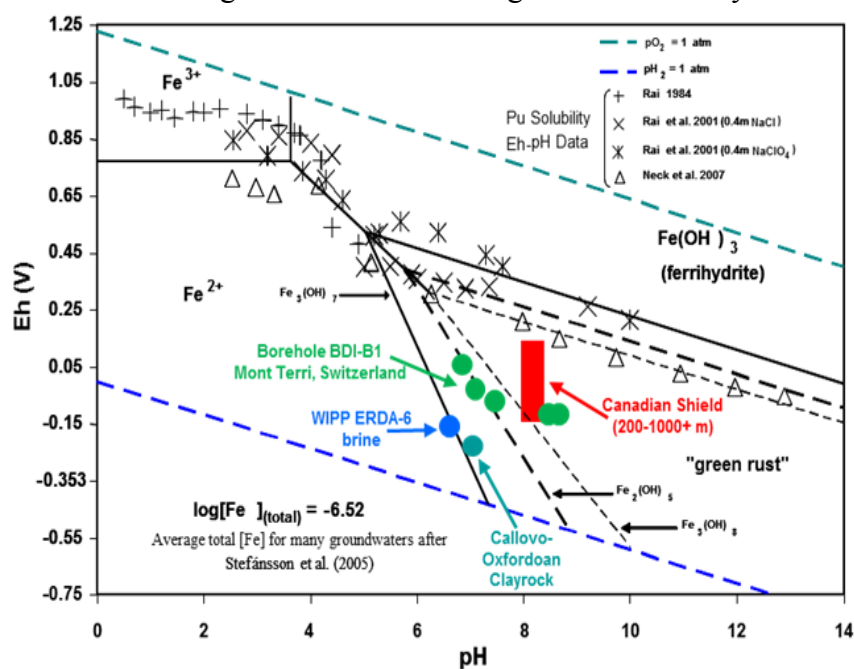
Microbes may produce CO₂(g), as illustrated by equations (7), (8), and (9). CO₂(g) can interact with Fe(s) to form FeCO₃(s). Brush (1990) describes the most likely corrosion reaction for this process as:



The dissociation reaction for FeCO₃ is described in Equation (30); the solubility product was selected by Chivot as:



Figure 2. Pourbaix Diagram for the Fe System



Plot of Eh versus pH relationships for the iron system with relevance to solution redox control for a corroding metallic barrier material (see text). Diagram was constructed using thermodynamic data from Bourrie et al. (1999, 2004) for green rust phases, YMP Pitzer thermodynamic database (Mariner, 2007) for ferrihydrite (Fe(OH)₃(s)), and ancillary data used obtained from the YMP thermodynamic database (Wolery and Jové-Colón, 2007), Robie et al. (1979), Stefánsson et al. (2005), and Parker and Khodakovskii (1995). The Eh-pH data depicted in the diagram for the Canadian Shield waters, WIPP ERDA-6 brine, Callovo-Oxfordian clayrock, and Mont Terri Opalinus Clay (borehole BDI-B1) are from Gascoyne et al. (2004), D'Appolonia Consulting Engineers (1983), Gaucher et al. (2009), and Turrero et al. (2006), respectively.

The reaction pathway is the same whether Fe₃O₄(s) or Fe(OH)₂(s) is the intermediate product. The free energy of the chemical equilibrium (29) can be expressed as:

$$\Delta G_{29}^0 = -R \times T \times \ln(10) \times \log \left(\frac{\{FeCO_3(s)\} \times f_{H_2}}{\{Fe(s)\} \times \{H_2O(l)\} \times f_{CO_2}} \right) \quad (35)$$

Using $\{FeCO_3(s)\} = \{Fe(s)\} = 1$, $\{H_2O(l)\} = 0.7$, and Brush's selection of free energies (see Table 2), the chemical equilibrium (29) yields a ratio of fugacities, $\log \frac{f_{H_2}}{f_{CO_2}}$, of 6.01.

With Chivot's selection of free energy values, this ratio increases 8.36. In both cases, the value indicates that the H₂(g) fugacity will exceed that of CO₂(g).

Chivot has calculated the Pourbaix diagram for a Fe/H₂O/CO₂ system at 25 °C, containing 10⁻⁶ m of dissolved Fe and several dissolved carbon concentrations: 10⁻⁴, 10⁻³, and 10⁻² m (Chivot, 2005, Figures 11-12). Total dissolved carbon concentrations of 10⁻⁴, 10⁻³, and 10⁻² m are in equilibrium with CO₂(g) fugacities of 10^{-5.2}, 10^{-4.2}, and 10^{-3.2} atm, respectively, at pH 9. These fugacities were calculated using Chivot's values for the CO₂(g)/CO₂⁰/HCO₃⁻/CO₃²⁻ system:



With: $\log \alpha = \log \frac{\{CO_2^0\}}{P_{CO_2}} = -1.47$, $\log K_{33} = \log \left(\frac{\{HCO_3^-\} \times \{H^+\}}{\{CO_2^0\}} \right) = -6.35$, and

$$\log K_{34} = \log \left(\frac{\{CO_3^{2-}\} \times \{H^+\}}{\{HCO_3^-\}} \right) = -10.33$$

An increase of total dissolved carbon concentrations from 10⁻⁴ to 10⁻² m leads to a substantially larger region of stability for FeCO₃. At pH 9, FeCO₃ occurs at potentials between -0.61 and -0.52 V_{NHE}, for a P_{CO₂(g)} of 10^{-5.2} atm, and at potentials between -0.67 and -0.37 V_{NHE}, for a P_{CO₂(g)} of 10^{-3.2} atm.

7.2.3 Fe/H₂O/H₂S System

Microbes may reduce sulfate (SO₄²⁻) to produce H₂S(aq or g), as shown in Equation (8). H₂S(g) interaction with Fe(s) may produce a number of solids, including (Fe,Ni)S(s), FeS_{1-x}(s)

(with $x = 0$ to 0.2), FeS(s) , $\text{FeS} \cdot n\text{H}_2\text{O(s)}$, $\text{Fe}_3\text{S}_4\text{(s)}$, and $\text{FeS}_2\text{(s)}$. The formation $\text{FeS}_2\text{(s)}$ can be described by the following equilibria (Equations (35) to (37)):



However, the WIPP PA considers only the formation of FeS(s) , the sole iron sulfide specie observed by Telander and Westerman (1997) in WIPP brines. FeS(s) formation can be described by the following equilibrium:



The solubility product of FeS(s) defined as Equation (39) was selected by Chivot (2004) as:



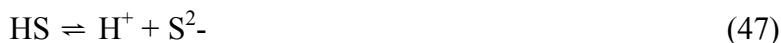
The free energy of the chemical equilibrium (38) can be expressed as:

$$\Delta G_{38}^0 = -R \times T \times \ln(10) \times \log \left(\frac{\{\text{FeS(s)}\} \times f_{\text{H}_2}}{\{\text{Fe(s)}\} \times f_{\text{H}_2\text{S}}} \right) \quad (44)$$

Using $\{\text{FeS(s)}\} = \{\text{Fe(s)}\} = 1$ and Chivot's (2004) selection of free energies for $\text{H}_2\text{S(g)}$ and amorphous FeS(s) (see Table 2), the ratio of gas fugacities, $\log \frac{f_{\text{H}_2}}{f_{\text{H}_2\text{S}}}$, is 10.80. This indicates that the $\text{H}_2\text{(g)}$ fugacity will exceed that of $\text{H}_2\text{S(g)}$.

Chivot constructed the Pourbaix diagram for a $\text{Fe}/\text{H}_2\text{O}/\text{H}_2\text{S}$ system at 25°C , containing 10^{-6} m of dissolved Fe and several dissolved carbon concentrations: 10^{-4} , 10^{-3} , and 10^{-2} m, for the solid and dissolved species, respectively. Total dissolved sulfur concentrations of 10^{-4} , 10^{-3} , and 10^{-2} m are in equilibrium with $\text{H}_2\text{S(g)}$ fugacities of $10^{-5.0}$, 10^{-4} , and $10^{-3.0}$ atm, respectively, at pH 9. These fugacities are calculated using Chivot's (2004) values for the $\text{H}_2\text{S(g)}/\text{H}_2\text{S}^0/\text{HS}^-/\text{S}^{2-}$ system:





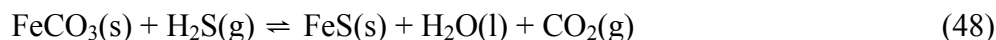
$$\text{With: } \log \alpha = \log \frac{\{\text{H}_2\text{S}^0\}}{P_{\text{H}_2\text{S}(\text{g})}} = -1.02, \quad \log K_{42} = \log \left(\frac{\{\text{HS}^-\} \times \{\text{H}^+\}}{\{\text{H}_2\text{S}^0\}} \right) = -6.99, \quad \text{and}$$

$$\log K_{43} = \log \left(\frac{\{\text{S}^{2-}\} \times \{\text{H}^+\}}{\{\text{HS}^-\}} \right) = -17.10$$

An increase of the total dissolved sulfur concentrations from 10^{-4} to 10^{-2} m expands the region of stability of the solid iron sulfides. At 10^{-4} m, $\text{FeS}_2(\text{s})$ is stable from pH 1.2 to 11.7 and $\text{FeS}(\text{s})$ from pH 6 to 11, but at 10^{-3} m, the stability region of $\text{FeS}_2(\text{s})$ ranges from pH 0.5 to 13.5 and $\text{FeS}(\text{s})$ from pH 5 to 14.5. At pH 9, $\text{FeS}_2(\text{s})$ can be found between -0.43 and -0.26 V at 10^{-4} m $\text{H}_2\text{S}(\text{g})$ and between -0.54 and -0.29 V_{NHE} at 10^{-2} m $\text{H}_2\text{S}(\text{g})$; $\text{FeS}(\text{s})$ can be found between -0.7 and -0.43 V_{NHE} at 10^{-4} m $\text{H}_2\text{S}(\text{g})$ and between -0.77 and -0.54 V_{NHE} at 10^{-2} m $\text{H}_2\text{S}(\text{g})$. As for the dissolved species, an increase of the total dissolved sulfur concentrations from 10^{-4} to 10^{-2} m leads to an increase of the stability region of FeSO_4^+ , the disappearance for FeOH^{2+} , and the appearance of FeSO_4^0 , which replaces part of the stability region of Fe^{2+} .

7.2.4 Fe/H₂O/CO₂/H₂S System

In the presence of both $\text{CO}_2(\text{g})$ and $\text{H}_2\text{S}(\text{g})$, the resulting FeCO_3 , formed from the interaction of $\text{Fe}(\text{s})$ and $\text{CO}_2(\text{g})$, reacts with $\text{H}_2\text{S}(\text{g})$ to form $\text{FeS}(\text{s})$:



The free energy of the chemical equilibria (44) can be expressed as:

$$\Delta G_{44}^0 = -R \times T \times \ln(10) \times \log \left(\frac{\{\text{FeS}(\text{s})\} \times \{\text{H}_2\text{O}\} \times f_{\text{CO}_2}}{\{\text{FeCO}_3(\text{s})\} \times f_{\text{H}_2\text{S}}} \right) \quad (49)$$

Using $\{\text{FeS}(\text{s})\} = \{\text{FeCO}_3(\text{s})\} = 1$ and $\{\text{H}_2\text{O}(\text{l})\} = 0.7$, and Chivot's selection of free energies presented in Table 2, the chemical equilibria (44) leads to the ratio of gas fugacities, $\log \frac{f_{\text{CO}_2}}{f_{\text{H}_2\text{S}}} = 2.44$. Therefore, the $\text{CO}_2(\text{g})$ produced always exceeds the amount of $\text{H}_2\text{S}(\text{g})$ consumed by the process. Moreover, laboratory and modeling studies have shown that the carbonation reaction of the MgO engineered barrier will buffer f_{CO_2} at a value of $10^{-5.50}$ atm in WIPP brines (see Section 7.2). Therefore, the fugacity of $\text{H}_2\text{S}(\text{g})$ resulting from the formation of $\text{FeS}(\text{s})$ in the WIPP is predicted to be $10^{-6.9}$ atm.

The instability of FeCO_3 in the presence of $\text{H}_2\text{S}(\text{g})$ has been illustrated with several diagrams. Garrels and Christ published a Pourbaix diagram for the system $\text{Fe}/\text{H}_2\text{O}/\text{CO}_2/\text{H}_2\text{S}$ (Garrels and Christ, 1990, Figure 7.23), merely a superposition of the diagrams they calculated for the systems $\text{Fe}/\text{H}_2\text{O}/\text{CO}_2$ and $\text{Fe}/\text{H}_2\text{O}/\text{H}_2\text{S}$. A system containing total dissolved concentrations of

10^{-4} M for S and 1 M for the carbonate (i.e. $f_{\text{H}_2\text{S}} = 10^{-5}$ atm and $f_{\text{CO}_2} = 10^{-1.2}$ atm, at pH 9) shows that Fe oxides ($\text{Fe}_2\text{O}_3(\text{s})$, $\text{Fe}_3\text{O}_4(\text{s})$), carbonate ($\text{FeCO}_3(\text{s})$), and sulfide ($\text{FeS}_2(\text{s})$) are stable. $\text{FeS}(\text{s})$, however, has totally disappeared, its stability region replaced by that of $\text{FeCO}_3(\text{s})$. This contradicts Equation (44), where the free energy ΔG^0 is negative, indicating that the reaction is spontaneous as written. This is clearly an artifact of the superposition of the Fe/ $\text{H}_2\text{O}/\text{CO}_2$ and Fe/ $\text{H}_2\text{O}/\text{H}_2\text{S}$ diagrams, which does not account for the equilibrium described in Equation (44). Garrels and Christ demonstrated that with lower and more realistic f_{CO_2} (e.g. $10^{-3.2}$ atm, at pH 9), only Fe oxides and sulfide ($\text{FeS}_2(\text{s})$) are stable and that FeCO_3 completely disappears from the diagram. This observation is particularly evident in Figure 6.10 of Garrels and Christ's publication (1990), which shows a partial pressure diagram of the system Fe/ $\text{O}_2/\text{CO}_2/\text{S}_2$. $\text{FeCO}_3(\text{s})$ is the stable specie for relatively high f_{CO_2} . In quasi-total absence of $\text{O}_2(\text{g})$ (10^{-100} atm), FeCO_3 is stable for f_{CO_2} greater than $10^{1.4}$ atm. However, with a slightly larger f_{O_2} (10^{-88} – 10^{-68} atm), FeCO_3 occurs at f_{CO_2} as low as $10^{-4.5}$ atm.

7.3 Pb Systems

Metallic Pb is oxidized in water, at 25 °C and 1 atm, though at lower rates than Fe. This oxidation process results in a number of species, as detailed below.

In the following text, thermodynamic calculations are performed which result in an estimated quantity of gas generated by the corrosion of Pb by H_2O , CO_2 , and H_2S . The standard free energies utilized in these calculations are presented in Table 3.

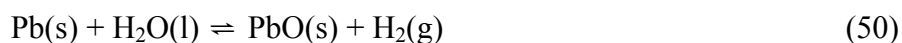
Table 3. Free Energies Selected by the USGS (1995) and Chivot (2004).

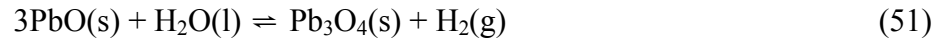
Compound	ΔG_f^0 selected by USGS (1995) (kJ/mol)	ΔG_f^0 selected by Chivot (2004) (kJ/mol)
H ₂ O(l)		-237.140
H ₂ (g)		0
H ⁺		0
CO ₂ (g)		-394.373
H ₂ S(g)		-33.44
Pb(s)	0	
PbO(s) litharge	-188.9	
PbO(s) massicot	-187.9	
Pb ₃ O ₄ (s)	-601.6	
PbCO ₃ (s)	-625.5	
PbS(s)	-96.8	

7.3.1 Pb/H₂O System

Metallic Pb will oxidize in water to form a number of species, including PbO(s), Pb₃O₄(s), Pb₂O₃(s), and PbO₂(s). Pb(OH)₂(s) is also a Pb(II) solid, but no evidence of its formation from metallic Pb could be found in the literature. The species likely to occur in an anoxic environment are PbO(s) and Pb₃O₄(s); both of which are soluble in acid. However, metallic Pb is thermodynamically stable in the presence of neutral or alkaline aqueous solutions in an anoxic environment, as a portion of its stability domain is located above the H₂/H₂O line of the Pourbaix diagram, as illustrated in by Pourbaix (1974, p. 489 Figure 1).

The formation of PbO(s) and Pb₃O₄(s) in an anoxic environment is described in equations (46) and (47).





The free energy of the chemical equilibria (46) and (47) can be expressed as:

$$\Delta G_{46}^0 = -R \times T \times \ln(10) \times \log \left(\frac{\{\text{PbO(s)}\} \times f_{\text{H}_2}}{\{\text{Pb(s)}\} \times \{\text{H}_2\text{O(l)}\}} \right) \quad (52)$$

$$\Delta G_{47}^0 = -R \times T \times \ln(10) \times \log \left(\frac{\{\text{Pb}_3\text{O}_4\text{(s)}\} \times f_{\text{H}_2}}{\{\text{PbO(s)}\}^3 \times \{\text{H}_2\text{O(l)}\}} \right) \quad (53)$$

Using $\{\text{Pb}_3\text{O}_4\text{(s)}\} = \{\text{PbO(s)}\} = \{\text{Pb(s)}\} = 1$, $\{\text{H}_2\text{O(l)}\} = 0.7$, and the free energies presented in Table 3, the chemical equilibria (46) and (47), which describe the formations of PbO(s) and $\text{Pb}_3\text{O}_4\text{(s)}$ from the anoxic corrosion of Pb(s) and PbO(s) by $\text{H}_2\text{O(l)}$, yield H_2 fugacities of approximately 10^{-9} and 10^{-36} atm, respectively.

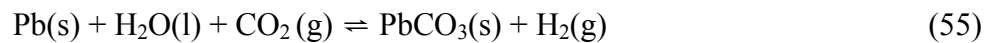
A E_h -pH diagram for the $\text{Pb}/\text{H}_2\text{O}$ system at 25°C was produced by Pourbaix (1974, p.489 Figure 1). It shows the stability regions of the Pb solid and dissolved species for different Pb concentrations and $\text{PbH}_2\text{(g)}$ pressures. At pH 9, with 1 M Pb , and 1 atm $\text{P}_{\text{PbH}_2\text{(g)}}$, Pb(s) , PbO(s) , $\text{Pb}_3\text{O}_4\text{(s)}$, and $\text{PbO}_2\text{(s)}$ are the solid stable phases for potentials between -0.2 than $-0.3 V_{\text{NHE}}$, between -0.3 and $0.4 V_{\text{NHE}}$, between 0.4 and $0.6 V_{\text{NHE}}$, and above $0.6 V_{\text{NHE}}$, respectively.

7.3.2 $\text{Pb}/\text{H}_2\text{O}/\text{CO}_2$ System

Pb(s) reacts with $\text{CO}_2\text{(g)}$ to form $\text{PbCO}_3\text{(s)}$, cerussite. The solubility product of this solid is obtained from Lide (2004-2005):



The formation of $\text{PbCO}_3\text{(s)}$ is described in Equation (51):



The free energy of the reaction shown in Equation (51) can be expressed as:

$$\Delta G_{51}^0 = -R \times T \times \ln(10) \times \log \left(\frac{\{\text{PbCO}_3\text{(s)}\} \times f_{\text{H}_2}}{\{\text{Pb(s)}\} \times \{\text{H}_2\text{O(l)}\} \times f_{\text{CO}_2}} \right) \quad (56)$$

Using $\{\text{PbCO}_3(\text{s})\} = \{\text{Pb}(\text{s})\} = 1$, $\{\text{H}_2\text{O}(\text{l})\} = 0.7$, and the selection of free energies presented in Table 3, the chemical equilibrium (52) leads to a ratio of fugacities $\log \frac{f_{\text{H}_2}}{f_{\text{CO}_2}}$ of -1.21, which indicates that $\text{CO}_2(\text{g})$ fugacity would slightly exceed that of $\text{H}_2(\text{g})$.

Garrels and Christ (1990) produced Pourbaix diagrams for the system $\text{Pb}/\text{H}_2\text{O}/\text{CO}_2$, for CO_2 fugacities of 10^{-4} and $10^{-2.7}$ atm (Garrels and Christ, 1990, Figures 7.26a and 7.26b). An increase in $\text{CO}_2(\text{g})$ pressure from 10^{-4} to $10^{-2.7}$ atm leads to the formation of $\text{Pb}_3(\text{OH})_2(\text{CO}_3)_2(\text{s})$, $\text{Pb}_3\text{O}_4(\text{s})$ and PbO . The increase in $\text{CO}_2(\text{g})$ also reduces the E_h at which metallic Pb is stable. At pH 9 and $f_{\text{CO}_2} = 10^{-4}$ atm, $\text{Pb}(\text{s})$, $\text{PbCO}_3(\text{s})$, and $\text{PbO}_2(\text{s})$ are stable for E_h lower than $-0.37 V_{\text{NHE}}$, between -0.37 and $+0.63 V_{\text{NHE}}$, and higher than $+0.63 V_{\text{NHE}}$, respectively.

7.3.3 $\text{Pb}/\text{H}_2\text{O}/\text{H}_2\text{S}$ System

$\text{Pb}(\text{s})$ reacts with $\text{H}_2\text{S}(\text{g})$ to form $\text{PbS}(\text{s})$. The solubility product of this solid is obtained from Lide (2004-2005):



The formation of $\text{PbS}(\text{s})$ is described by Equation (54):



The free energy of the chemical equilibrium (54) can be expressed as:

$$\Delta G_{54}^0 = -R \times T \times \ln(10) \times \log \left(\frac{\{\text{PbS}(\text{s})\} \times f_{\text{H}_2}}{\{\text{Pb}(\text{s})\} \times f_{\text{H}_2\text{S}}} \right) \quad (59)$$

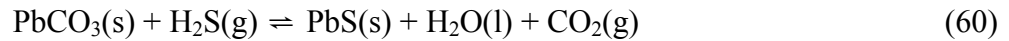
Using $\{\text{PbS}(\text{s})\} = \{\text{Pb}(\text{s})\} = 1$ and the selection of free energies presented in Table 3, the ratio of gas fugacities, $\log \frac{f_{\text{H}_2}}{f_{\text{H}_2\text{S}}}$ is 11.11. This implies that $\text{H}_2(\text{g})$ fugacity would exceed that of $\text{H}_2\text{S}(\text{g})$.

Garrels and Christ produced a Pourbaix diagram for the system $\text{Pb}/\text{H}_2\text{O}/\text{CO}_2$ (Garrels and Christ, 1990, Figure 7.26c). Even at a total S of only 10^{-5} m, (i.e., 10^{-6} atm $\text{H}_2\text{S}(\text{g})$, at pH 9), both $\text{PbSO}_4(\text{s})$ and $\text{PbS}(\text{s})$ have large stability fields and the region of stability for metallic Pb is pushed to substantially lower E_h . At pH 9, $\text{PbS}(\text{s})$, $\text{PbSO}_4(\text{s})$, and $\text{PbO}_2(\text{s})$ are the only thermodynamically stable species; they occur for E_h below $-0.26 V_{\text{NHE}}$, between -0.26 and $+0.5 V_{\text{NHE}}$, and above $+0.5 V_{\text{NHE}}$, respectively.

7.3.4 Pb/H₂O/CO₂/H₂S System

Garrels and Christ's produced a Pourbaix diagram for the system Pb/H₂O/CO₂/H₂S (1990, Figure 7.26e). This diagram pertains to relatively high sulfur and carbonate concentrations: 10^{-1.5} m (i.e., f_{H₂S} = 10^{-2.5} atm, at pH 9) and 10⁻¹ m (i.e., f_{CO₂} = 10^{-2.2} atm, at pH 9), respectively. At such f_{CO₂}, Pb₃(OH)₂(CO₃)₂(s), Pb₃O₄(s), and PbO(s) are stable within the pH and E_h boundaries described in this diagram; however, these solids do not appear at more relevant f_{CO₂} levels (e.g., 10⁻⁴ atm) where the region of stability for PbCO₃(s) extends to pH 13, above which the soluble HPbO₂²⁻ is stable. The inclusion of 10^{-1.5} m of sulfur in the Pb/H₂O/CO₂ system leads to the appearance of PbS, a small region where PbS and S are both stable, and the reduction of the region of stability for metallic Pb to very low values of E_h and high pH. Unlike Fe, for which the stability region of the sulfide minerals replaces that of the carbonates, the Pb sulfide material only reduces the stability regions of the carbonates. This is illustrated in a partial pressure diagram published by Garrels and Christ's, for the system Pb/H₂O/CO₂/S (1990, Figure 6.17). PbCO₃(s) can form at CO₂ pressures as low as 10⁻⁵ atm, a value far below the 10^{1.4} atm required for the stability of FeCO₃. At pH 9 and in the conditions described by 7.26e of Garrels and Christ (1990), the stable solids are PbS(s), PbCO₃(s), and PbO₂(s), for potentials below -0.27 V_{NHE}, between -0.27 and +0.67 V_{NHE}, and greater than +0.67 V_{NHE}, respectively.

Based upon the two figures discussed above (Garrels and Christ, 1990, Figures 7.26e and 6.17), we anticipate that PbCO₃(s) will interact with H₂S(g), in a similar fashion as iron carbonate does:



The free energy of the chemical equilibria (56) can be expressed as:

$$\Delta G_{56}^0 = -R \times T \times \ln(10) \times \log \left(\frac{\{\text{PbS}(\text{s})\} \times \{\text{H}_2\text{O}(\text{l})\} \times f_{\text{CO}_2}}{\{\text{PbCO}_3(\text{s})\} \times f_{\text{H}_2\text{S}}} \right) \quad (61)$$

Using {PbS (s)} = {PbCO₃(s)} = 1 and {H₂O(l)} = 0.7, and Chivot's selection of free energies presented in Table 3, the chemical equilibrium (57) leads to the ratio of gas fugacities, $\log \frac{f_{\text{CO}_2}}{f_{\text{H}_2\text{S}}} = 12.32$. Therefore, the CO₂(g) produced exceeds the amount of H₂S(g) consumed by the process. The fugacity of CO₂(g) in the WIPP brine is predicted to equilibrate at 10^{-5.50} atm (see Section 5.2), therefore, the fugacity of H₂S(g) resulting from the formation of PbS(s) in the WIPP is predicted to be 10^{-17.8} atm.

7.4 Summary of the Thermodynamic Calculations

In an Fe/H₂O system, the formation of Fe₃O₄(s) or Fe(OH)₂(s) from the oxidation of Fe(s), and the formation of Fe₃O₄(s) from the decomposition of Fe(OH)₂(s) produce large quantities of H₂(g) (the resulting f_{H₂(g)} are 503, 616, and 273 atm, respectively). In an Pb/H₂O system, the

formations of the Pb solids generates much less $H_2(g)$ than Fe does in similar conditions; the formations of $PbO(s)$ and $Pb_3O_4(s)$ yield $H_2(g)$ fugacities of 10^{-9} and 10^{-36} atm, respectively. In reducing environment and at pH 9, the stable Fe solid species are $FeOOH(s)$, $Fe_3O_4(s)$, and $Fe(s)$, stable in a system containing 10^{-6} m dissolved Fe for E_h higher than $-0.35 V_{NHE}$, between -0.35 and $-0.50 V_{NHE}$, and lower than $-0.50 V_{NHE}$, respectively. $Fe(OH)_2(s)$ is not stable at pH 9 in pure water. More recently, the “green rust” phases have been identified as important components of the secondary phase assemblage. Green rust is a mixed ferric-ferrous iron double-layered compound, in which the most reducing form (fougèrite) has the composition: $[Fe^{2+}_4Fe^{3+}_2(OH)_{12}][CO_3] \cdot 3H_2O$. Production of green rust phases also liberates a large volume of H_2 gas. Because we are interested in reactions in the sulfide system, the most likely phases we will find in our experiments are the FeS_2 polymorphs (pyrite, cubic and marcasite, orthorhombic) and pyrrhotite ($Fe_{1-x}S$). Although many geochemical models include mackinawite (FeS) as the equilibrium sulfide phase, it is likely that mackinawite is only a transient, metastable phase. It will be important to identify the stable phase assemblage in our experiments because knowledge of the phase assemblage will tell us how many moles of H_2 gas are produced in the iron corrosion reaction. In reducing environment and at pH 9, $PbO(s)$ and $Pb(s)$ are the stable solid species, occurring for potentials between -0.3 and $0.4 V_{NHE}$, and below $-0.3 V_{NHE}$, respectively, for a system containing 1 M total Pb. In those conditions, $Pb_3O_4(s)$ is stable for E_h values between 0.4 and $0.6 V_{NHE}$.

In an $Fe/H_2O/CO_2$ system, the formation of $FeCO_3(s)$ yields a ratio of the fugacities between $H_2(g)$ and $CO_2(g)$ equal to $10^{8.36}$. However, the stability region of $FeCO_3(s)$ is very small. For example, in a system at pH 9, containing 10^{-6} m dissolved Fe, and with a $CO_2(g)$ fugacity of $10^{-5.2}$ atm (close to that set by the brucite-hydromagnesite buffer, $10^{-5.5}$ atm), $FeCO_3$ occurs at potentials between -0.61 and $-0.52 V_{NHE}$. The stability region becomes larger with increasing $f_{CO_2(g)}$. In an $Pb/H_2O/CO_2$ system, the formation of $PbCO_3(s)$ yields a ratio of fugacities between $H_2(g)$ and $CO_2(g)$ equal to $10^{1.21}$, smaller than that for the Fe system. But the stability region of $PbCO_3(s)$ is much larger than that of $FeCO_3(s)$; at pH 9 and $f_{CO_2} = 10^{-4}$ atm, $PbCO_3(s)$ is stable for E_h ranging from -0.37 to $+0.63 V_{NHE}$.

Out of all the solid iron sulfide species, the WIPP PA considers only $FeS(s)$, which formation yields a ratio of gas fugacities between $H_2(g)$ and $H_2S(g)$ of $10^{10.80}$, for an $Fe/H_2O/H_2S$ system. If such a system contains 10^{-4} m $H_2S(g)$, $FeS(s)$ can be found between -0.7 and $-0.43 V_{NHE}$. An increase of $H_2S(g)$ only increases the stability region of $FeS(s)$ to higher pH values. In a $Pb/H_2O/H_2S$ system, the formation of $PbS(s)$ formation yields a ratio of gas fugacities between $H_2(g)$ and $H_2S(g)$ of $10^{11.11}$, quite similar to that for the Fe system. $PbS(s)$ is stable for higher E_h than $FeS(s)$ is. At pH 9, $PbS(s)$ is the thermodynamically stable species for E_h below $-0.26 V_{NHE}$.

In a system containing both $H_2S(g)$ and $CO_2(g)$, $FeCO_3(s)$ is unstable, as $FeS(s)$ can form from the sulfidization of $FeCO_3(s)$. This reaction produces slightly more $CO_2(g)$ than $H_2S(g)$ is consumed by the process; for example, for a $10^{-5.5}$ atm $CO_2(g)$ fugacity, the fugacity of the produced $H_2S(g)$ is $10^{-6.9}$ atm. This $H_2S(g)$ fugacity is much lower ($10^{-17.8}$ atm) for the formation of $PbS(s)$ in similar conditions. $FeCO_3(s)$ is very unstable in presence of sulfide; in quasi-total absence of $O_2(g)$ (10^{-100} atm), $FeCO_3$ is only stable for f_{CO_2} greater than $10^{1.4}$ atm. But $PbCO_3(s)$

can form at CO₂ pressures as low as 10⁻⁵ atm, a value far below that required for the stability of FeCO₃(s).

7.5 Calculations Involving Microbial Gas Generation

The total volume of waste to be emplaced in the WIPP is 175,564 m³, with CH and RH waste volumes of 1.69 × 10⁵ m³ and 7,080 m³, respectively (US Congress, 1992). The total quantity of C from the CPR is 1.10 × 10⁹ mol (Nemer and Stein, 2005), the total quantity of NO₃⁻ and SO₄²⁻ from the waste are 4.31 × 10⁷ and 4.61 × 10⁶ mol, respectively, as recorded in the WIPP parameter database (WIPP PA, 2001a; WIPP PA, 2001b). The following sections detail the impact which Fe and Pb could potentially have on the microbial gasses, with a clear focus on the consumption of CO₂ via the formation of metal carbonates. In order to simplify these calculations, it was assumed that all of the material (Fe or Pb) was available for consumption. As such, the values presented below represent the upper limit of CO₂ consumption and carbonate formation by the Fe and Pb present within WIPP.

7.5.1 Impact of Fe on Microbial Gases

Crawford (Crawford, 2005a) published the values for the disposal inventory for Fe-base metals and alloys; for the purpose of the following calculations, we consider the Fe-base metals and alloys (e.g. steel) to be 100 % Fe. The estimated Fe densities are 110 and 59 kg/m³, in the CH and RH waste, and 170 and 540 kg/m³, in the CH and RH waste containers, at closure time. Therefore, considering CH and RH volumes of 1.69 × 10⁵ and 7,080 m³, respectively (U.S. Congress, 1992), the estimated Fe mass in the CH and RH wastes, including the containers, is 4.7 × 10⁷ and 4.2 × 10⁶ kg, respectively, which total to 9.2 × 10⁸ mol of Fe in WIPP, or 1,094 mol Fe per equivalent drum. Lappin (1989) had estimated this number at 900 mol Fe per drum equivalent.

7.5.1.1 DENITRIFICATION, SULFATE REDUCTION, NO METHANOGENESIS

The WIPP PA simulations assume that microbial gas generation may occur only through a combination of denitrification and sulfate reduction (Equations (7) and (8)), as specified by the EPA (Cotsworth, 2004, Comment G-14). During denitrification (Equation (7)), microbes consume 6 mol of C and 4.8 mol of NO₃⁻ and produce 6 mol of CO₂(g) and 2.4 mol of N₂(g). Therefore, if all of the NO₃⁻ contained within the inventory were consumed, the total quantity of CPR C consumed would be:

$$4.31 \times 10^7 \times \frac{6}{4.8} = 5.39 \times 10^7 \text{ moles C} \quad (62)$$

Similarly, the quantities of CO₂(g) and N₂(g) generated by the denitrification process are 5.39 × 10⁷ and 2.16 × 10⁷ mol, respectively. During sulfate reduction (Equation (8)), 6 mol of C react with 3 mol of SO₄²⁻ to produce 6 mol of CO₂(g) and 3 mol of H₂S(g). Although the inventory contains 4.61 × 10⁶ mol of SO₄²⁻, additional sulfate may be available from the WIPP structure itself (i.e., from marker beds, brines), and as such it is difficult to quantify exactly how much sulfate is available for microbial activity. The EPA has required that we assume that sufficient SO₄²⁻ is available to consume all remaining C (after denitrification) in CPR materials.

The total quantity of carbon consumed by the sulfate reduction process is the difference between the total C available from the CPR (1.10×10^9) and the total quantity of C consumed by the denitrification process (5.39×10^7), which is 1.05×10^9 mol of C. The amount of $\text{H}_2\text{S}(\text{g})$ and $\text{CO}_2(\text{g})$ produced by sulfate reduction is 5.24×10^8 and 1.05×10^9 mol, respectively. As a result, if all of the carbon available within the WIPP CPR is consumed by sulfate reduction, the resulting quantity of $\text{CO}_2(\text{g})$ would be the sum of that produced by each of the aforementioned processes, or 1.10×10^9 mol.

Section 7.2.2 demonstrated that the fugacity of $\text{H}_2(\text{g})$ produced by the formation of FeCO_3 exceeds that of $\text{CO}_2(\text{g})$ consumed during the process by 8 orders of magnitude. Therefore, if sufficient $\text{Fe}(\text{s})$ was available, nearly all the $\text{CO}_2(\text{g})$ generated by the microbial activity would be consumed during FeCO_3 formation. The production of FeCO_3 from 1.10×10^9 mol $\text{CO}_2(\text{g})$ (Equation (29)) would consume 1.10×10^9 mol $\text{Fe}(\text{s})$, which exceeds the total Fe inventory (9.2×10^8 Fe mol). Therefore, if the total Fe inventory is consumed by the production of FeCO_3 , only 9.2×10^8 mol $\text{CO}_2(\text{g})$ will be consumed, 9.2×10^8 mol of $\text{FeCO}_3(\text{s})$ will be produced, and 1.8×10^8 mol $\text{CO}_2(\text{g})$ (16% of the total predicted quantity of $\text{CO}_2(\text{g})$) will remain unreacted.

Section 7.2.4 demonstrated that the fugacity of $\text{CO}_2(\text{g})$ produced during the formation of $\text{FeS}(\text{s})$, as described by Equation (44), exceeds that of $\text{H}_2\text{S}(\text{g})$ consumed during this process by over 2 orders of magnitude. Calculations presented above determined that the sulfate reduction reaction produced 5.24×10^8 mol of $\text{H}_2\text{S}(\text{g})$. However, 9.2×10^8 mol of $\text{FeCO}_3(\text{s})$ are formed. Thus the limiting reagent for the formation of $\text{FeS}(\text{s})$ is $\text{H}_2\text{S}(\text{g})$. As such, the reaction between $\text{H}_2\text{S}(\text{g})$ and $\text{FeCO}_3(\text{s})$ will generate 5.24×10^8 mol of $\text{CO}_2(\text{g})$ and leave 4.0×10^8 mol of $\text{FeCO}_3(\text{s})$ unreacted.

The total quantity of $\text{CO}_2(\text{g})$ remaining after the production of $\text{FeCO}_3(\text{s})$ and $\text{FeS}(\text{s})$ is 7.0×10^8 mol, which is then available to react with the engineered barrier MgO to form $\text{Mg}_5(\text{CO}_3)_4(\text{OH})_2 \cdot 4\text{H}_2\text{O}$. Table 4 summarizes the results of the previous series of calculations.

Table 4. Result Summaries for Fe-Gas Reactions With the Denitrification And Sulfate Reduction Processes, but Without Methanogenesis.

Material available (mol)	Reactants (mol)	Products (mol)	Unreacted Materials (mol)
$C_6H_{10}O_5 + 4.8H^+ + 4.8NO_3^- \rightarrow 7.4H_2O(l) + 6CO_2(g) + 2.4N_2(g)$			
C: 1.10×10^9 NO ₃ ⁻ : 4.31×10^7	C: 5.39×10^7 NO ₃ ⁻ : 4.31×10^7	CO ₂ (g): 5.39×10^7 N ₂ (g): 2.16×10^7	C: 1.05×10^9 NO ₃ ⁻ : 0
$C_6H_{10}O_5 + 6H^+ + 3SO_4^{2-} \rightarrow 5H_2O(l) + 6CO_2(g) + 3H_2S(g)$			
C: 1.05×10^9 SO ₄ ²⁻ : unknown	C: 1.05×10^9 SO ₄ ²⁻ : 1.05×10^9	CO ₂ (g): 1.05×10^9 H ₂ S(g): 5.24×10^8	C: 0 SO ₄ ²⁻ : unknown
$Fe(s) + H_2O(l) + CO_2(g) \rightleftharpoons FeCO_3(s) + H_2(g)$			
Fe: 9.2×10^8 CO ₂ (g): 1.10×10^9	Fe: 9.2×10^8 CO ₂ (g): 9.2×10^8	FeCO ₃ (s): 9.2×10^8 H ₂ (g): 9.2×10^8	Fe: 0 CO ₂ (g): 1.8×10^8
$FeCO_3(s) + H_2S(g) \rightleftharpoons FeS(s) + H_2O(l) + CO_2(g)$			
FeCO ₃ (s): 9.2×10^8 H ₂ S(g): 5.24×10^8	FeCO ₃ (s): 5.24×10^8 H ₂ S(g): 5.24×10^8	FeS(s): 5.24×10^8 CO ₂ (g): 5.24×10^8	FeCO ₃ (s): 4.0×10^8 H ₂ S(g): 0

7.5.1.2 DENITRIFICATION, SULFATE REDUCTION, AND METHANOGENESIS

The calculations in this section include the methanogenesis process. Two cases have been considered here. In the first case, we consider that the sulfate available from both the waste and the WIPP rooms, which includes sulfate contained in marker beds and brines, will react with CPR carbon during sulfate reduction. In this case, the total quantity of sulfate available for reaction is unknown. In the second case, only the sulfate contributed by the waste emplaced within the WIPP is considered.

Case 1: 50% of the CPR Carbon Remaining After Denitrification Reacts With Sulfate and 50% Reacts With Water to Form CH₄

Calculations similar to those presented above were conducted with the assumption that half of the remaining unreacted CPR carbon following denitrification (i.e. 5.24×10^8 mol) will react through the sulfate reduction process and the other half through methanogenesis. Denitrification produces 5.39×10^7 mol of CO₂(g) and 2.16×10^7 mol of N₂(g) and leaves 1.05×10^9 mol of CPR carbon unreacted. Sulfate reduction will produce 5.24×10^8 mol of CO₂(g) and 2.62×10^8 mol H₂S(g) and methanogenesis will produce 2.62×10^8 mol of each CH₄(g) and CO₂(g). A total of 8.39×10^8 mol of CO₂(g) can then react with metallic Fe to form 8.39×10^8 mol of each FeCO₃(s) and H₂(g), leaving 8.4×10^7 mol of Fe(s) unreacted. The reaction between FeCO₃(s) and H₂S(s) produces 2.62×10^8 mol of each FeS(s) and CO₂(g). This newly generated CO₂(g) can then react with the unreacted Fe(s) to form an additional 8.4×10^7 mol of FeCO₃(s), leaving 1.8×10^8 mol of CO₂(g) unreacted. This remaining CO₂(g) can interact with the engineered barrier as described previously. This calculation is summarized in Table 5.

Table 5. Summary of the Results for Fe-Gas Reactions With Denitrification, Sulfate Reduction, and Methanogenesis Processes, Case 1.

Material available (mol)	Reactants (mol)	Products (mol)	Unreacted Materials (mol)
$C_6H_{10}O_5 + 4.8H^+ + 4.8NO_3^- \rightarrow 7.4H_2O(l) + 6CO_2(g) + 2.4N_2(g)$			
C: 1.10×10^9 NO ₃ ⁻ : 4.31×10^7	C: 5.39×10^7 NO ₃ ⁻ : 4.31×10^7	CO ₂ (g): 5.39×10^7 N ₂ (g): 2.16×10^7	C: 1.05×10^9 NO ₃ ⁻ : 0
$C_6H_{10}O_5 + 6H^+ + 3SO_4^{2-} \rightarrow 5H_2O(l) + 6CO_2(g) + 3H_2S(g)$			
C: 5.24×10^8 SO ₄ ²⁻ : unknown	C: 5.24×10^8 SO ₄ ²⁻ : 5.24×10^8	CO ₂ (g): 5.24×10^8 H ₂ S(g): 2.62×10^8	C: 0 SO ₄ ²⁻ : unknown
$C_6H_{10}O_5 + H_2O(l) \rightarrow 3CH_4(g) + 3CO_2(g)$			
C: 5.24×10^8	C: 5.24×10^8	CO ₂ (g): 2.62×10^8 CH ₄ (g): 2.62×10^8	C: 0
$Fe(s) + H_2O(l) + CO_2(g) \rightleftharpoons FeCO_3(s) + H_2(g)$			
Fe: 9.2×10^8 CO ₂ (g): 8.39×10^8	Fe: 8.39×10^8 CO ₂ (g): 8.39×10^8	FeCO ₃ (s): 8.39×10^8 H ₂ (g): 8.39×10^8	Fe: 8.4×10^7 CO ₂ (g): 0
$FeCO_3(s) + H_2S(g) \rightleftharpoons FeS(s) + H_2O(l) + CO_2(g)$			
FeCO ₃ (s): 8.39×10^8 H ₂ S(g): 2.62×10^8	FeCO ₃ (s): 2.62×10^8 H ₂ S(g): 2.62×10^8	FeS(s): 2.62×10^8 CO ₂ (g): 2.62×10^8	FeCO ₃ (s): 5.8×10^8 H ₂ S(g): 0
$Fe(s) + H_2O(l) + CO_2(g) \rightleftharpoons FeCO_3(s) + H_2(g)$			
Fe: 8.4×10^7 CO ₂ (g): 2.62×10^8	Fe: 8.4×10^7 CO ₂ (g): 8.4×10^7	FeCO ₃ (s): 8.4×10^7 H ₂ (g): 8.4×10^7	Fe: 0 CO ₂ (g): 1.8×10^8

Case 2: The CPR Carbon Remaining After Denitrification Reacts With Sulfates and Then With Water to Form CH₄

Calculations similar to those conducted for Case 1 were performed, with the additional assumption that the CPR carbon remaining unreacted after denitrification (i.e. 1.05×10^9 mol of C) will react with the entire waste sulfate inventory (4.61×10^6 mol SO₄²⁻) but with none of the sulfate contained in the marker beds or the brines. The remaining CPR carbon will then react to produce CH₄. Denitrification produces 5.39×10^7 mol of CO₂(g) and 2.16×10^7 mol of N₂(g) leaving 1.05×10^9 mol of CPR carbon unreacted. Sulfate reduction will produce 9.22×10^6 mol of CO₂(g) and 4.61×10^6 mol H₂S(g), and methanogenesis will produce 5.19×10^8 mol each of CH₄(g) and CO₂(g). Thus, a total of 5.82×10^8 mol of CO₂(g) can then react with metallic Fe to form 5.8×10^8 mol each of FeCO₃(s) and H₂(g), leaving 3.4×10^8 mol of Fe(s) unreacted. The reaction between FeCO₃(s) and H₂S(s) produces 4.6×10^6 mol each of FeS(s) and CO₂(g). This newly generated CO₂(g) can then react with the remaining Fe(s) to form an additional 4.6×10^6 mol of FeCO₃(s), consuming all of the available CO₂(g) and leaving 3.4×10^8 mol of Fe(s) unreacted. These calculations are summarized in Table 6.

Table 6. Summary of Results for Fe-Gas Reactions with the Denitrification, Sulfate Reduction, and Methanogenesis Processes, Case 2.

Material available (mol)	Reactants (mol)	Products (mol)	Unreacted Materials (mol)
$C_6H_{10}O_5 + 4.8H^+ + 4.8NO_3^- \rightarrow 7.4H_2O(l) + 6CO_2(g) + 2.4N_2(g)$			
C: 1.10×10^9 NO ₃ ⁻ : 4.31×10^7	C: 5.39×10^7 NO ₃ ⁻ : 4.31×10^7	CO ₂ (g): 5.39×10^7 N ₂ (g): 2.16×10^7	C: 1.05×10^9 NO ₃ ⁻ : 0
$C_6H_{10}O_5 + 6H^+ + 3SO_4^{2-} \rightarrow 5H_2O(l) + 6CO_2(g) + 3H_2S(g)$			
C: 1.05×10^9 SO ₄ ²⁻ : 4.61×10^6	C: 9.22×10^6 SO ₄ ²⁻ : 4.61×10^6	CO ₂ (g): 9.22×10^6 H ₂ S(g): 4.61×10^6	C: 1.04×10^9 SO ₄ ²⁻ : 0
$C_6H_{10}O_5 + H_2O(l) \rightarrow 3CH_4(g) + 3CO_2(g)$			
C: 1.04×10^9	C: 1.04×10^9	CO ₂ (g): 5.19×10^8 CH ₄ (g): 5.19×10^8	C: 0
$Fe(s) + H_2O(l) + CO_2(g) \rightleftharpoons FeCO_3(s) + H_2(g)$			
Fe: 9.2×10^8 CO ₂ (g): 5.82×10^8	Fe: 5.8×10^8 CO ₂ (g): 5.8×10^8	FeCO ₃ (s): 5.8×10^8 H ₂ (g): 5.8×10^8	Fe: 3.4×10^8 CO ₂ (g): 0
$FeCO_3(s) + H_2S(g) \rightleftharpoons FeS(s) + H_2O(l) + CO_2(g)$			
FeCO ₃ (s): 5.8×10^8 H ₂ S(g): 4.61×10^6	FeCO ₃ (s): 4.6×10^6 H ₂ S(g): 4.6×10^6	FeS(s): 4.6×10^6 CO ₂ (g): 4.6×10^6	FeCO ₃ (s): 5.8×10^8 H ₂ S(g): 0
$Fe(s) + H_2O(l) + CO_2(g) \rightleftharpoons FeCO_3(s) + H_2(g)$			
Fe: 3.4×10^8 CO ₂ (g): 4.6×10^6	Fe: 4.6×10^6 CO ₂ (g): 4.6×10^6	FeCO ₃ (s): 4.6×10^6 H ₂ (g): 4.6×10^6	Fe: 3.4×10^8 CO ₂ (g): 0

7.5.2 Pb Impact on Microbial Gases

The densities of Pb within the WIPP originating from the containers for CH and RH wastes have been estimated by Crawford to be 1.3×10^{-2} and $4.2 \times 10^2 \text{ kg/m}^3$, respectively (Crawford, 2005a). Therefore, considering the CH and RH volumes of 1.69×10^5 and 7080 m^3 , respectively (U.S. Congress, 1992), the total masses of Pb from the CH and RH waste containers are 2.2×10^3 and $3.0 \times 10^6 \text{ kg}$, respectively. Crawford also estimated the total quantity of Pb and cadmium metal present within the “lead/cadmium” waste stream for both CH and RH wastes at closure time (Crawford, 2005b). As no differentiation was made between Pb and cadmium for the data discussed above, for this study we will assume that the total quantity is exclusively Pb. Although more Pb may be present in the WIPP from sources other than the “lead/cadmium” waste stream, this contribution to the total quantity has not been quantified, and thus will be neglected here. As a result, by considering only material contributed by the “lead/cadmium” waste stream, the estimated quantity from this calculation represents the lower limit of Pb present within the WIPP at closure. From Crawford, the estimated volumes of Pb within the CH and RH wastes are 2.6×10^2 and 19 m^3 , respectively, yielding associated densities of $1.5 \times 10^2 \text{ kg/m}^3$ and 74 kg/m^3 (Crawford, 2005b). Therefore, the Pb masses contained in the CH and RH wastes are 3.9×10^4 and $1.4 \times 10^3 \text{ kg}$, respectively. Combining the above information, the lower limit of the total quantity of Pb within the WIPP at closure is estimated to be $3.0 \times 10^6 \text{ kg}$ ($1.5 \times 10^7 \text{ mol}$), which translates to 17 mol of Pb per equivalent drum.

The maximum quantity, or upper limit, of Pb present within the WIPP can be estimated by using the density of the material denoted as “other metal/alloys” in the CH and RH wastes. This category contains all of the metals present in the wastes with the exception of Fe and aluminum, and has been estimated to be 32 and 57 kg/m^3 for CH and RH waste, respectively (Crawford, 2005a). Applying this to the volumes of CH and RH waste, the maximum quantity which may present within the WIPP at closure time is $8.6 \times 10^6 \text{ kg}$ ($4.2 \times 10^7 \text{ mol}$), or 49 mol of Pb per equivalent drum.

7.5.2.1 DENITRIFICATION, SULFATE REDUCTION, NO METHANOGENESIS

Calculations similar to those developed in section 7.5.1.1 for Fe were performed for Pb. The denitrification process generates 5.39×10^7 and $2.16 \times 10^7 \text{ mol}$ of $\text{CO}_2(\text{g})$ and $\text{N}_2(\text{g})$, respectively and $1.05 \times 10^9 \text{ mol}$ of CPR carbon is left unreacted. In absence of methanogenesis, all the unreacted C reacts with sulfate and form $1.05 \times 10^9 \text{ mol}$ of $\text{CO}_2(\text{g})$ and $5.24 \times 10^8 \text{ mol}$ of $\text{H}_2\text{S}(\text{g})$. Then $1.10 \times 10^9 \text{ mol}$ of $\text{CO}_2(\text{g})$ is available to react with $\text{Pb}(\text{s})$ to generate $1.5 \times 10^7 \text{ mol}$ of each $\text{PbCO}_3(\text{s})$ and $\text{H}_2(\text{g})$, leaving $1.1 \times 10^9 \text{ mol}$ of unreacted $\text{CO}_2(\text{g})$. The reaction between $\text{PbCO}_3(\text{s})$ and $\text{H}_2\text{S}(\text{g})$ generates $1.5 \times 10^7 \text{ mol}$ of each $\text{PbS}(\text{s})$ and $\text{CO}_2(\text{g})$. Finally, a total of $1.1 \times 10^9 \text{ mol}$ of $\text{CO}_2(\text{g})$ is available to react with MgO . These calculations are summarized in Table 7.

Table 7. Summary of the Result of Pb-Gas Reactions with Denitrification and Sulfate Reduction Processes, and Without Methanogenesis.

Material available (mol)	Reactants (mol)	Products (mol)	Unreacted Materials (mol)
$C_6H_{10}O_5 + 4.8H^+ + 4.8NO_3^- \rightarrow 7.4H_2O(l) + 6CO_2(g) + 2.4N_2(g)$			
C: 1.10×10^9 NO ₃ ⁻ : 4.31×10^7	C: 5.39×10^7 NO ₃ ⁻ : 4.31×10^7	CO ₂ (g): 5.39×10^7 N ₂ (g): 2.16×10^7	C: 1.05×10^9 NO ₃ ⁻ : 0
$C_6H_{10}O_5 + 6H^+ + 3SO_4^{2-} \rightarrow 5H_2O(l) + 6CO_2(g) + 3H_2S(g)$			
C: 1.05×10^9 SO ₄ ²⁻ : unknown	C: 1.05×10^9 SO ₄ ²⁻ : 1.05×10^9	CO ₂ (g): 1.05×10^9 H ₂ S(g): 5.24×10^8	C: 0 SO ₄ ²⁻ : unknown
$Pb(s) + H_2O(l) + CO_2(g) \rightleftharpoons PbCO_3(s) + H_2(g)$			
Pb: 1.5×10^7 CO ₂ (g): 1.10×10^9	Pb: 1.5×10^7 CO ₂ (g): 1.5×10^7	PbCO ₃ (s): 1.5×10^7 H ₂ (g): 1.5×10^7	Pb: 0 CO ₂ (g): 1.1×10^9
$PbCO_3(s) + H_2S(g) \rightleftharpoons PbS(s) + H_2O(l) + CO_2(g)$			
PbCO ₃ (s): 1.5×10^7 H ₂ S(g): 5.24×10^8	PbCO ₃ (s): 1.5×10^7 H ₂ S(g): 1.5×10^7	PbS(s): 1.5×10^7 CO ₂ (g): 1.5×10^7	PbCO ₃ (s): 0 H ₂ S(g): 5.1×10^8

7.5.2.2 DENITRIFICATION, SULFATE REDUCTION, AND METHANOGENESIS

As in the calculations performed for Fe presented in Section 7.5.1.2, two scenarios were considered. In the first case, we consider that an unknown amount of sulfate reacts with the CPR carbon and in the second, we consider solely the sulfate issued from the waste.

Case 1: 50% of the C Remaining After Denitrification Reacts With Sulfate And 50% Reacts With Water to From CH₄

Calculations similar to those developed in section 7.5.1.2 for Fe were performed for Pb. In this section, it is assumed that half of the remaining moles of CPR C left unreacted following denitrification (i.e. 5.24×10^8 mol) will react through sulfate reduction process and the other half

through methanogenesis. Denitrification produces 5.39×10^7 mol of $\text{CO}_2(\text{g})$ and 2.16×10^7 mol of $\text{N}_2(\text{g})$, leaving 1.05×10^9 mol of CPR carbon unreacted. Sulfate reduction will produce 5.24×10^8 mol of $\text{CO}_2(\text{g})$ and 2.62×10^8 mol $\text{H}_2\text{S}(\text{g})$ and methanogenesis will produce 2.62×10^8 mol of each $\text{CH}_4(\text{g})$ and $\text{CO}_2(\text{g})$. The resulting $\text{CO}_2(\text{g})$ can then react with metallic Pb to form 1.5×10^7 mol each of $\text{PbCO}_3(\text{s})$ and $\text{H}_2(\text{g})$, leaving 8.2×10^8 mol of $\text{CO}_2(\text{g})$ unreacted. The reaction between $\text{PbCO}_3(\text{s})$ and $\text{H}_2\text{S}(\text{s})$ produces 1.5×10^7 mol each of $\text{PbS}(\text{s})$ and $\text{CO}_2(\text{g})$. At this point, there is no additional metallic Pb to react with this newly generated $\text{CO}_2(\text{g})$ and the 8.2×10^8 mol of $\text{CO}_2(\text{g})$ generated can react with the engineered barrier as described previously. These calculations are summarized in Table 8.

Table 8. Result Summaries for Pb-Gas Reactions With Denitrification, Sulfate Reduction, and Methanogenesis Processes, Case 1.

Material available (mol)	Reactants (mol)	Products (mol)	Unreacted Materials (mol)
$C_6H_{10}O_5 + 4.8H^+ + 4.8NO_3^- \rightarrow 7.4H_2O(l) + 6CO_2(g) + 2.4N_2(g)$			
C: 1.10×10^9 NO ₃ ⁻ : 4.31×10^7	C: 5.39×10^7 NO ₃ ⁻ : 4.31×10^7	CO ₂ (g): 5.39×10^7 N ₂ (g): 2.16×10^7	C: 1.05×10^9 NO ₃ ⁻ : 0
$C_6H_{10}O_5 + 6H^+ + 3SO_4^{2-} \rightarrow 5H_2O(l) + 6CO_2(g) + 3H_2S(g)$			
C: 5.24×10^8 SO ₄ ²⁻ : unknown	C: 5.24×10^8 SO ₄ ²⁻ : 5.24×10^8	CO ₂ (g): 5.24×10^8 H ₂ S(g): 2.62×10^8	C: 0 SO ₄ ²⁻ : unknown
$C_6H_{10}O_5 + H_2O(l) \rightarrow 3CH_4(g) + 3CO_2(g)$			
C: 5.24×10^8	C: 5.24×10^8	CO ₂ (g): 2.62×10^8 CH ₄ (g): 2.62×10^8	C: 0
$Pb(s) + H_2O(l) + CO_2(g) \rightleftharpoons PbCO_3(s) + H_2(g)$			
Pb: 1.5×10^7 CO ₂ (g): 8.39×10^8	Pb: 1.5×10^7 CO ₂ (g): 1.5×10^7	PbCO ₃ (s): 1.5×10^7 H ₂ (g): 1.5×10^7	Pb: 0 CO ₂ (g): 8.2×10^8
$PbCO_3(s) + H_2S(g) \rightleftharpoons PbS(s) + H_2O(l) + CO_2(g)$			
PbCO ₃ (s): 1.5×10^7 H ₂ S(g): 2.62×10^8	PbCO ₃ (s): 1.5×10^7 H ₂ S(g): 1.5×10^7	PbS(s): 1.5×10^7 CO ₂ (g): 1.5×10^7	PbCO ₃ (s): 0 H ₂ S(g): 2.5×10^8

Case 2: The C Remaining After Denitrification Reacts With The Waste Sulfates And Then With Water to Form CH₄

Calculations similar to those developed in section 7.5.1.2 , Case 2 for Fe were performed for Pb: it is assumed that the remaining moles of CPR carbon left unreacted following

denitrification (i.e. 1.05×10^9 mol of C) will react with the entire waste sulfate inventory, but with none of the sulfate of the marker beds or brines; the inventory contains 4.61×10^6 mol SO_4^{2-} . The remaining CPR carbon will then react to form CH_4 . Denitrification produces 5.39×10^7 mol of $\text{CO}_2(\text{g})$ and 2.16×10^7 mol of $\text{N}_2(\text{g})$ and leaves 1.05×10^9 mol of CPR carbon unreacted. Sulfate reduction will produce 9.22×10^6 mol of $\text{CO}_2(\text{g})$ and 4.61×10^6 mol $\text{H}_2\text{S}(\text{g})$ and methanogenesis will produce 5.19×10^8 mol of each $\text{CH}_4(\text{g})$ and $\text{CO}_2(\text{g})$. A total of 5.82×10^8 mol of $\text{CO}_2(\text{g})$ can then react with metallic Pb to form 1.5×10^7 mol of each $\text{PbCO}_3(\text{s})$ and $\text{H}_2(\text{g})$, leaving no unreacted Pb(s). The reaction between $\text{PbCO}_3(\text{s})$ and $\text{H}_2\text{S}(\text{s})$ produces 4.6×10^6 mol each of $\text{PbS}(\text{s})$ and $\text{CO}_2(\text{g})$. At this point, unlike Fe, there is no more metallic Pb to react with this newly generated $\text{CO}_2(\text{g})$ and the 5.7×10^8 mol of $\text{CO}_2(\text{g})$ generated can react with the engineered barrier as described previously. These calculations are summarized in Table 9.

Table 9. Result Summaries for Pb-Gas Reactions with Denitrification, Sulfate Reduction, and Methanogenesis Processes, Case 2.

Material available (mol)	Reactants (mol)	Products (mol)	Unreacted Materials (mol)
$C_6H_{10}O_5 + 4.8H^+ + 4.8NO_3^- \rightarrow 7.4H_2O(l) + 6CO_2(g) + 2.4N_2(g)$			
C: 1.10×10^9 NO ₃ ⁻ : 4.31×10^7	C: 5.39×10^7 NO ₃ ⁻ : 4.31×10^7	CO ₂ (g): 5.39×10^7 N ₂ (g): 2.16×10^7	C: 1.05×10^9 NO ₃ ⁻ : 0
$C_6H_{10}O_5 + 6H^+ + 3SO_4^{2-} \rightarrow 5H_2O(l) + 6CO_2(g) + 3H_2S(g)$			
C: 1.05×10^9 SO ₄ ²⁻ : 4.61×10^6	C: 9.22×10^6 SO ₄ ²⁻ : 4.61×10^6	CO ₂ (g): 9.22×10^6 H ₂ S(g): 4.61×10^6	C: 1.04×10^9 SO ₄ ²⁻ : 0
$C_6H_{10}O_5 + H_2O(l) \rightarrow 3CH_4(g) + 3CO_2(g)$			
C: 1.04×10^9	C: 1.04×10^9	CO ₂ (g): 5.19×10^8 CH ₄ (g): 5.19×10^8	C: 0
$Pb(s) + H_2O(l) + CO_2(g) \rightleftharpoons PbCO_3(s) + H_2(g)$			
Pb: 1.5×10^7 CO ₂ (g): 5.82×10^8	Pb: 1.5×10^7 CO ₂ (g): 1.5×10^7	PbCO ₃ (s): 1.5×10^7 H ₂ (g): 1.5×10^7	Pb: 0 CO ₂ (g): 5.7×10^8
$PbCO_3(s) + H_2S(g) \rightleftharpoons PbS(s) + H_2O(l) + CO_2(g)$			
PbCO ₃ (s): 1.5×10^7 H ₂ S(g): 4.61×10^6	PbCO ₃ (s): 4.6×10^6 H ₂ S(g): 4.6×10^6	PbS(s): 4.6×10^6 CO ₂ (g): 4.6×10^6	PbCO ₃ (s): 9.9×10^6 H ₂ S(g): 0

7.6 Summary of the Results of Interactions of Fe and Pb with Microbially Generated Gases

Table 10 summarizes the results presented in sections 7.5.1 and 7.5.2. The table presents the quantity of carbon involved in each of the microbial gas generation process: denitrification, sulfate reduction and methanogenesis, and for each of the sulfate scenarios, where the sulfate

involved in the sulfate reduction is issued either from the waste or from the waste and the WIPP structure (marker beds and brines). If we assume that sulfate from both the waste and the WIPP structure are available for reaction, and that the only viable carbon consumption pathways are denitrification (Eqn. 7) and sulfate reduction (Eqn. 8), then 95% of the CPR carbon will be consumed via sulfate reduction. Under those same conditions, if we add methanogenesis (Eqn. 9) as an additional consumption pathway for the CPR carbon, the quantity consumed by sulfate reduction falls to 48%. Finally, if we then neglect sulfate originating from the WIPP structure, and consider only the sulfate within the waste, then just 1% of the CPR carbon will be consumed via sulfate reduction.

Table 10 also shows the quantity of gases produced from the reactions taking place between metallic Fe and Pb and the gases generated by microbial activities. The amount of $\text{CO}_2(\text{g})$ generated from the reaction between metallic Fe or Pb with the microbially generated gas decreases as the amount of carbon consumed through methanogenesis increases. This is due to the fact that, for a fixed amount of carbon, sulfate reduction generates twice as much $\text{CO}_2(\text{g})$ as methanogenesis. In the absence of methanogenesis, the reaction of metallic Fe and Pb with the microbially generated gases produces 7.0×10^8 and 1.1×10^9 mol of $\text{CO}_2(\text{g})$, respectively. With 48 % of carbon consumed through methanogenesis, these numbers decrease to 1.8×10^8 and 8.4×10^8 mol of $\text{CO}_2(\text{g})$, respectively. The only case where $\text{CO}_2(\text{g})$ produced by microbial activity and metal corrosion is completely consumed is for Fe corrosion after 94 % of the CPR carbon has been consumed through methanogenesis. Of course, $\text{CH}_4(\text{g})$ generation increases as the amount of carbon involved in methanogenesis increases. The amount of $\text{N}_2(\text{g})$ does not vary with methanogenesis as it is only produced through the denitrification process. Finally, the only case in which $\text{H}_2(\text{g})$ varies is when the $\text{CO}_2(\text{g})$ is completely consumed before metallic Fe is consumed. In this case, 5.9×10^8 mol of $\text{H}_2(\text{g})$ is then produced. Otherwise, 9.2×10^8 and 1.5×10^7 mol of $\text{H}_2(\text{g})$ are produced from the corrosion of Fe and Pb, respectively.

Table 10. Percentage of Carbon Involved in the Microbial Gas Generation Reactions and Moles of Gases Generated from the Reactions between Metallic Fe and Pb and the Microbially Generated Gas.

Origin of sulfate	No Methanogenesis		With Methanogenesis			
	Waste and WIPP		Waste and WIPP		Waste	
	Fe	Pb	Fe	Pb	Fe	Pb
CPR C consumed by:						
• Denitrification	5 %		4.5 % ¹		5 %	
• Sulfate Reduction	95 %		47.6 % ¹		1 %	
• Methanogenesis	0 %		47.6 % ¹		94 %	
Gases Produced and unreacted metals:						
CO ₂ (g) (mol)	7.0 × 10 ⁸	1.1 × 10 ⁹	1.8 × 10 ⁸	8.4 × 10 ⁸	0	5.7 × 10 ⁸
CH ₄ (g) (mol)	0	0	2.6 × 10 ⁸	2.6 × 10 ⁸	5.2 × 10 ⁸	5.2 × 10 ⁸
N ₂ (g) (mol)	2.2 × 10 ⁷					
H ₂ (g) (mol)	9.2 × 10 ⁸	1.5 × 10 ⁷	9.2 × 10 ⁸	1.5 × 10 ⁷	5.9 × 10 ⁸	1.5 × 10 ⁷
H ₂ S(g) (mol)	0	5.1 × 10 ⁸	0	2.5 × 10 ⁸	0	0
Unreacted metal (mol)	0	0	0	0	3.4 × 10 ⁸	0

7.7 Additional Aspects on the Influence of Fe and Pb on the System

In addition to forming a number of new solid phases, Fe and Pb will also influence the solution compositions as they slowly dissolve in the aqueous phase. Two brines will be considered in this study. The first, simulating fluids present within reservoirs in the Castile Formation, is the ERDA-6 brine. The other brine is the GWB which simulates intergranular brines from the Salado formation at or near the stratigraphic horizon of the repository. These brines, which will be discussed in more detail in Section 9.2.1, contain inorganic ligands, such as SO₄²⁻, Cl⁻, and HCO₃⁻ that will complex to the soluble species of Fe and Pb and therefore change

¹ Percentage rounding explains that the sum is not 100%.

the brine composition. Moreover, the WIPP waste will contain significant amount of acetate, oxalate, citrate, and ethylenediaminetetraacetic acid (EDTA), at closure time, as discussed later in this document in the section 9.1.3 . For example, acetate, oxalate, citrate, and EDTA will form complexes with Fe^{2+} , with the following stability constant of the first complexes: $10^{1.4}$ (at 0 M ionic strength), $10^{3.05}$ (at 1.0 M ionic strength), $10^{4.4}$ (at 0.1 M ionic strength), $10^{14.30}$ (at 0.1 M ionic strength), respectively (Martell et al., 1998). Pb^{2+} will also form complexes with those ligands; the stability constant of the first complexes with oxalate, citrate, and EDTA are $10^{4.20}$ (at 1.0 ionic strength), $10^{4.44}$ (at 1.0 ionic strength), and $10^{18.0}$ (at 0.1 ionic strength), respectively (Martell et al., 1998). As a comparison, the first stability constants of the complexes formed between americium (Am) and acetate, oxalate, citrate, and EDTA are $10^{1.51}$, $10^{4.17}$, $10^{5.2}$, and $10^{13.96}$, respectively, at 1.0 M ionic strength (Choppin et al., 2001).

8 REVIEW OF DATA FOUND ON CORROSION IN THE WIPP

There have been a number of studies which have, at least peripherally, evaluated the corrosion behavior of Fe and Pb alloys under WIPP relevant conditions. One such study was performed by Telander and Westerman beginning in 1989 and ending in 1996 (Telander and Westerman, 1993; 1997). Their study focused on determining the quantity of gas generation (specifically H₂ from water reduction) which would result from the corrosion process. Carbon steel (both hot and cold rolled material), along with a series of other nonferrous alloys were evaluated in Brine A and ERDA-6 with overpressures of N₂, CO₂, H₂, and H₂S (both singularly and in combinations). In their study, it was found that there was no statistically significant difference in behavior between the two different steels under any of the conditions evaluated – as such, the results for all of the Fe alloys were combined and averaged. Considerable H₂ production was observed in most of the test cases – however, though the corrosion rate of carbon steel did seem to decrease for moderate H₂ pressures (36 to 70 atm), they stated that the overall impact of H₂ overpressure on the corrosion rate of low carbon steels was insignificant in the long run, even at pressures as high as the lithostatic pressure.

Under a N₂ overpressure, which creates an O₂ depleted environment, samples immersed in Brine A exhibited a corrosion rate of 0.71 μm/yr. The resulting corrosion product was found to be an iron-magnesium hydroxide. Samples exposed to the vapor phase over the brine showed no discernable corrosion. In the ERDA-6 brine, the corrosion rate was found to be highly dependant on the pH of the brine, ranging from 7.9 mm/yr at pH 5 to 2 μm/yr at pH 9.

When a CO₂ overpressure was applied, samples were observed to passivate in Brine A due to the formation of protective layer of FeCO₃ or Fe,Mn(CO₃). The passivation process was found to require a minimum concentration of CO₂ in the gas phase somewhere between 0.16 and 0.32 mol CO₂/m² of steel. The steel could also be depassivated by the addition of H₂S, after which repassivation did not occur, and corrosion continued as if the samples were exposed to anoxic brine. Samples were also exposed to the vapor phase over the brine, where again no significant attack was observed.

With an overpressure of H₂S, the steel samples were again observed to passivate, with the formation of a protective iron sulfide layer (FeS). Addition of small concentrations of CO₂ to the gas mixture did not disrupt the passive layer.

Another test program which was conducted under WIPP relevant conditions was the Materials Interface Interactions Test (MIIT) performed by Molecke, et. al. (1993) The goal of that work was to evaluate the behavior of a wide range of materials, including several carbon steels (American Society for Testing and Materials (ASTM) A216 grade WCA and a Belgian carbon steel) and a Pb alloy, to WIPP relevant conditions. In this test, samples were emplaced within boreholes in room J and nominally exposed to Brine A which had equilibrated with the surrounding salt. The gas composition within the boreholes (which were mostly filled with brine) was not controlled, and did not contain the mixture of microbially generated gasses which are being explored in this proposal. Samples were monitored periodically for 5 years, and a qualitative assessment of the corrosion performance was given. In the case of the carbon steels, all samples demonstrated significant general and localized attack, with voluminous corrosion

product being produced (the composition was not determined). The Pb samples also underwent significant general and localized attack, though there was more sample to sample variability. As with the steel, the composition of the corrosion products was not analyzed.

One final test program which focused in understanding the mechanism of Fe corrosion in WIPP brines was performed by Wang, et. al (Wang, 2001). In this study, A36 cold rolled steel sheet was evaluated in G Seep and ERDA-6 brines which had been equilibrated for 7 days with $Mg(OH)_2$. While they were not able to elucidate the finer points of the corrosion process due to experimental limitations, they were able to characterize the corrosion product which resulted on the steel coupons. In this case, a green rust was produced (a layered (Fe(II), Fe(III)) hydroxide with water and anions such as chloride and sulfate occupying the interlayer spaces.

Xia et al. (2001) studied the effect of Fe on the plutonium, neptunium, and uranium solubilities and oxidation states in NaCl solutions and in ERDA-6. But they did not discuss the Fe corrosion occurring during the experiments.

More recent experiments have been carried out on a variety of steel and Fe-based alloy products to determine the reactivity in the presence of CO_2 and H_2S . Although these experiments were not carried out using WIPP-type brines, the results of these investigations provide valuable clues to the mechanism of corrosion and the types of corrosion products that are likely to form on the surface of the steel. Results from experiments with steel exposed to H_2S -bearing solutions (e.g., Liu, et al., 2014) show that corrosion products quickly form and coalesce to create “protective” layers on the steel surface. The beginning corrosion product is mackinawite, FeS_{1-x} , which over time transforms into pyrrhotite, $Fe_{1-x}S$. They concluded that the type of corrosion product that forms, which depends on the temperature and H_2S partial pressure, governs the effectiveness of the diffusion barrier. The investigation conducted by Bai et al. (2014) also concluded that the sulfide mineralogy evolved over time from mackinawite to troilite and finally to pyrite (FeS_2). The evolution of iron sulfide phases on the surface of steel has additional implications for the solubility of Fe^{2+} in WIPP brines and is the subject of another ongoing Test Plan (TP 14-05; “Test Plan for the Experimental Determination of the Solubilities of Iron and Lead in the Presence of Dissolved Hydrogen Sulfide Species”). Qi et al. (2014) investigated the relationship between H_2S partial pressure and hydrogen diffusion into steel. Diffusion of H^+ into steel is thought to impart negative properties to steel, such as embrittlement (e.g., Gonzalez et al. 1997; Huang et al. 2011; Koyama et al. 2012; Younes et al., 2013). These authors reported a direct relationship between the partial pressure of H_2S and hydrogen diffusion, which resulted in a loss of tensile strength and plasticity. These conclusions are in accord with other investigations (e.g., Zheng et al. 2014a). Brittle zones developed around inclusions of MnS in the steel, and this was related to accumulation of atomic hydrogen in defect “traps” near the inclusions. Failure of steel canisters holding waste, for example, may result in waste becoming exposed to aqueous solution sooner than through dissolution of the steel, and rupture of the steel may also expose more steel surface area to corrosion. Therefore, it is critical to understand the development of corrosion layers as a function of time, temperature (up to 200 °C), pH and the concentration of HS^- (or partial pressure of H_2S).

Note, however, that many of the experiments conducted on steel products were in low pH solutions (pH = 2 – 5) and room temperature. As described in detail below, the experiments

anticipated in this Test Plan will constitute new data that can be used to better understand the geochemistry of the repository at WIPP.

9 EXPERIMENTAL PROCESS DESCRIPTION

As discussed above, the goal of this proposed research is to determine the likely corrosion products which will result due to oxidation of the Fe and Pb contained within the WIPP. A mixed flowing gas exposure system will be constructed which allows for the simulation of the predicted in-room atmosphere within the WIPP. Exposure testing will then be performed on a number of relevant materials, after which the resulting aged surfaces will be quantitatively assessed via an array of analytical techniques.

9.1 Materials

9.1.1 Alloys

Several ferrous and non-ferrous materials were selected for evaluation in this study. Two Fe-base alloys, representative of the container materials used for CH waste along with a Pb alloy representative of potential shielding material for RH waste were selected. The text below describes the reasoning used to select the relevant alloys, along with their compositions.

9.1.1.1 Fe-BASE ALLOYS

CH waste within the WIPP is in general disposed in one of four different forms – drums (55, 85, and 100 gallons in size), standard waste boxes (Golden, 2004a), ten drum overpacks (Golden, 2004b), or standard large boxes (Golden, 2005). The materials of construction, as well as the anticipated quantity (Burns, 2005), of each storage container is presented in Table 11. The materials of construction are specified in a series of ASTM specifications, as shown in Table 12. These specifications each encompass a range of different carbon and high-strength, low-alloy (HSLA) steels. From Table 11, it is clear that the majority of the steel present in the WIPP (from waste containers) will be of a composition as defined either by ASTM A36, ASTM A1008, or ASTM A1011, with the largest quantity defined by ASTM A1008 (waste drums). The steels specified in A1008 and A1011 are similar (see Table 12) with the exception of the method of production, with the former being cold-rolled, and the latter hot-rolled. While this will yield different mechanical properties in the final product, it has been found previously by Telander and Westerman (Telander and Westerman, 1993; 1997) that the two will behave similarly from a corrosion point of view in brines of a composition relevant to the WIPP. As such, only one of them will be selected for evaluation in this study (ASTM A1008), along with a material which conforms to ASTM A36.

Table 11. Materials of Construction for the Various Waste Containers.

ASTM Specification →	A29	A36	A108	A266	A500	A510	A513	A516	A537	A576	A865	A1008	A1011	F835	SAE grade 5	ASME/ANSI B1.20.1	# in WIPP
Standard Waste Box																	17031
Body panels, Lid panel													X				
Body tubular frame; body bumper							X										
Body clips; lid frame bar		X															
Rivets						X				X							
Lid lift nut	X	X				X				X							

Table 11. Materials of Construction for the Various Waste Containers (cont.).

ASTM Specification →	A29	A36	A108	A266	A500	A510	A513	A516	A537	A576	A865	A1008	A1011	F835	SAE grade 5	ASME/ANSI B1.20.1	# in WIPP
Ten Drum Overpack																	7138
Body panels; body lift clip; lid panel; lid band		X															
Body flange				X				X	X								
Body bumper							X										
Spacer							X										
Lift nut	X	X				X				X							
Socket head cap screws														X			
Waste Drums																	
55, 85, and 100 Gallon Drums												X					396719

Table 12. Material Compositions Defined by ASTM Specifications (all compositions in wt %).

Specification		C	Mn	P	S	Si	Cu	Ni	Cr	Mo	V	Cd	Ti
A29	Grade 1018	0.15-0.20	0.60-0.90	0.04 max	0.05 max	0.1 max							
A36		0.26 max		0.04 max	0.05 max	0.4 max		0.2 min (if specified)					
A108	calls out A29 or A510												
A266	grade 3 normalized	0.35 max	0.8-1.05	0.025 max	0.025 max	0.15-0.35							
A500	unspecified Grade	0.27-0.30 max	1.40 max	0.045 max	0.045 max			0.18 min (if specified)					
A510	Grade 1008	0.10 max	0.25-0.40	0.04 max	0.05 max								
	Grade 1010	0.08-0.13	0.30-0.60	0.04 max	0.05 max								
	Grade 1018	0.15-0.20	0.60-0.90	0.04 max	0.05 max								
	Grade 1110	0.08-0.13	0.30-0.60	0.04 max	0.08-0.13	0.10 max							

Table 12. Material Compositions Defined by ASTM Specifications (cont.).

Specification		C	Mn	P	S	Si	Cu	Ni	Cr	Mo	V	Cd	Ti
		—	—	—	—	—	—	—	—	—	—	—	—
A513	Grade 1008	0.1 max	0.5 max	0.035 max	0.035 max								
	Grade 1010	0.08-0.13	0.30-0.60	0.035 max	0.035 max								
	Grade 1012	0.1-0.15	0.30-0.60	0.035 max	0.035 max								
	Grade 1015	0.12-0.18	0.30-0.60	0.035 max	0.035 max								
	Grade 1016	0.12-0.18	0.60-0.90	0.035 max	0.035 max								
	Grade 1017	0.14-0.20	0.30-0.60	0.035 max	0.035 max								
	Grade 1018	0.14-0.20	0.60-0.90	0.035 max	0.035 max								
	Grade 1019	0.14-0.20	0.70-1.00	0.035 max	0.035 max								
	Grade 1020	0.17-0.23	0.30-0.60	0.035 max	0.035 max								
A516	grade 70 Normalized	0.27 max	0.85-1.20	0.035 max	0.035 max	0.15-0.45							
A537	Class 1	0.24 max	0.64-1.46	0.035 max	0.035 max	0.13-0.55	0.38 max	0.28 max	0.29 max	0.09 max			

Table 13. ASTM Specifications.

ASTM Specification	Title
A29	Standard Specification for Steel Bars, Carbon and Alloy, Hot-Wrought, General Requirements for
A36	Standard Specification for Carbon Structural Steel
A108	Standard Specification for Steel Bar, Carbon and Alloy, Cold Finished
A266	Standard Specification for Carbon Steel Forgings for Pressure Vessel Components
A500	Standard Specification for Cold-Formed Welded and Seamless Carbon Steel Structural Tubing in Rounds and Shapes
A510	Standard Specification for General Requirements for Wire Rods and Coarse Round Wire, Carbon Steel
A513	Standard Specification for Electric-Resistance-Welded Carbon and Alloy Steel Mechanical Tubing
A516	Standard Specification for Pressure Vessel Plates, Carbon Steel, for Moderate- and Lower Temperature Service
A537	Standard Specification for Pressure Vessel Plates, Heat Treated, Carbon-Manganese-Silicon Steel
A576	Standard Specification for Steel Bars, Carbon, Hot-Wrought, Special Quality
A865	Standard Specification for Threaded Couplings, Steel, Black or Zinc Coated Welded or Seamless, for use in Steel Pipe Joints
A1011	Standard Specification for Steel Sheet and Strip, Hot Rolled, Carbon, Structural, High-Strength, Low-Alloy, and High-Strength Low Alloy with Improved Formability
A1008	Standard specification for steel, sheet, cold-rolled, carbon, structural, high-strength Low-Alloy, High-Strength Low-Alloy with Improved Formability, Solution Hardenable, and Bake Hardenable
F835	Standard specification for alloy steel socket button and flat countersunk head cap screws

9.1.1.2 Pb-BASE METALS

The estimated quantity of Pb present in the repository as a result of the waste and its containers is 3.0×10^6 kg (see Section 7.5.2). Only 1.4 % of this Pb mass is from the Pb present in the waste itself; the vast majority is due to the Pb contained in the lid of the packaging. The drawings for the RH containers (Hertelendy, 1984) do not specify the Pb alloy used.

The WIPP is planning to use Pb-lined containers for on-site storage of high radiation dose rate (i.e. RH) waste. There are six different container sizes which will be used, listed in Table 14. The nominal mass of Pb resulting from these containers is 4.4×10^6 kg, assuming that the Pb is at the external edge of the container. The Pb-lined containers are currently planned to be used exclusively for on-site storage. But in the event that they are disposed underground, the WIPP Pb inventory would increase. Several specifications are called out for the specific Pb alloy – namely military specification QQ-L-171e, which in turn calls ASTM B29. The specific grade of Pb required has not been defined. As such, referring to the mil spec, Grade C is specified for chemical use, and is what will be used here. This alloy is defined in ASTM B29 as chemical-copper lead (UNS L51121) and is nominally 99.9% Pb.

Table 14. Size and Number of the Pb-Lined Containers.

Container ID	Pb-lined thickness (nom. in.) ¹	External Height (in.) ¹	External Diameter (in.) ¹	Projected Number in WIPP ²
TS55-PB2	2	34 ¼	24	1200
TS55-PB3	3	34 ¼	24	1200
TS85-PB2	2	39 ¼	27	150
TS85-PB3	3	39 ¼	27	150
TS110-PB2	2	43	31	150
TS146-PB3	3	43	33	150

¹ Bull Run Metal (2004)

² Woolsey (2005)

9.1.2 Gas Composition

9.1.2.1 CARRIER GAS

As discussed previously, with time it has been postulated that bacteria may consume the CPR materials within the WIPP, resulting in the production of large quantities of various gasses (see Equations (7), (8) and (9)), namely CH₄, CO₂, and H₂S. In addition, it is anticipated, based upon the results of Telander and Westerman discussed above, that considerable H₂ will be produced via the corrosion process. Due to their flammable natures, the use of either H₂ or CH₄ in the experimentation described within this test plan presents serious environmental health and safety concerns. As such, it is desirable that an alternative carrier gas be identified. In order to make such a replacement, the impact which each of these gases would have on the materials of concern in this study must be considered.

The storage containers utilized within the WIPP are constructed primarily from a variety of carbon and HSLA steels. In the study performed by Telander and Westerman, these materials were exposed to environments containing various concentrations of the gas species described above, including H₂. In terms of the impact which H₂ had on the corrosion rate of these materials, they concluded that while there appeared to be a minor influence as the partial pressure of H₂ increased, that the overall impact in the long term would be negligible. As such, use of H₂ as a major component of the carrier gas is not necessary.

For CH₄, steels compositionally similar to those found within the WIPP are widely used in natural gas transmission and are specified for such applications by the Pipeline and Hazardous Materials Safety Administration's Office of Pipeline Safety (the federal safety authority for natural gas pipelines). The DOT specifies that the materials used in such gas transmission lines conform to ASTM A53. Looking at that specification, it can be seen that all of the materials utilized within the steel WIPP storage containers also conform to the rather broad compositional range defined within ASTM A53. While CH₄ has been found to inhibit corrosion to a degree in carbon steels in deoxygenated Salton Sea brines at 232°C within a glass lined autoclave (Cramer, 1980), there is no data in the literature indicating that such an effect extends to the temperatures of interest in this study. As such, it is reasonable to assume that for the temperature and pressure regimes of concern here, the steel is effectively inert in this environment. Thus any replacement chemistry must be similarly inert. One such gas which is easily handled and readily available is N₂, which consequently will be used in this study as the carrier gas.

9.1.2.2 CO₂ CONCENTRATION

Several approaches were used to determine an appropriate range of CO₂(g) concentrations to be evaluated in this study. The thermodynamic calculations performed in Section 7 demonstrated that if all the carbon from the CPR materials projected to be emplaced within the WIPP was consumed by microbial activity, it would yield a total of 1.10×10^9 , 8.39×10^8 , and 5.82×10^8 mol of CO₂(g), in the absence of methanogenesis, with 48% of the CPR carbon consumed by methanogenesis, and with 94% of the CPR carbon consumed by methanogenesis, respectively. Assuming a headspace volume in the WIPP of 26,000 m³ (Stein, 2005), and using the gas molar volume of 22.4 L (at the standard condition of temperature and

pressure, i.e. 0°C and 1 atm), these quantities of CO₂(g) result in internal pressures of 950, 720, and 500 atm., respectively. It should be noted that these values are projected generated quantities, and do not account for consumption by the engineered barrier or metals within the WIPP.

Francis et al. (1997) performed experiments to evaluate the quantity and rate of CO₂(g) generation by microbes under WIPP relevant conditions. Nemer et al. (2005) utilized Francis' data to calculate the rate of gas generation within the WIPP. The maximum CO₂(g) generation rates were found to be 0.459 and 2.015×10^{-2} μmol CO₂/g cellulose/day, for periods of time shorter than 500 days and for long term, respectively. The minimum rates are 0.0115 and 5.57×10^{-3} μmol CO₂/g cellulose/day, for short (less than 500 days) and long term conditions, respectively. Francis' experiments were performed using 5 g of cellulose with a head space of 50 mL. Using the gas molar volume of 22.4 L, we deduce that after 500 days, the minimum and the maximum pressures of CO₂(g) were 0.013 and 0.514 atm, respectively. These numbers would yield pressures of 46 and 165 atm for a 10,000 years period (if the "long term" rate extend to 10,000 years), if the CO₂(g) was not consumed. In the presence of MgO, a portion of the CO₂(g) generated by the microbes is consumed to form a magnesium hydroxyl-carbonate, as shown in Equation (10). The resulting pressure of CO₂(g) following interaction with MgO was calculated to be 10^{-5.5} atm (Brush, 2005). We suspect that the kinetics of CO₂(g) consumption by MgO would not be overwhelmingly faster than that of CO₂(g) with Fe or Pb. Therefore, we will work with pressure of CO₂(g) greater than 10^{-5.5} atm (i.e. 3.6 ppm) but below 165 atm (i.e. 10⁸ ppm). For example, we can work with the concentrations from 350 to 1,000 ppm.

9.1.2.3 H₂S CONCENTRATION

We have determined in Section 7 of this document that the sulfidization of the entire inventory of Fe and Pb would yield a ratio of CO₂(g) to H₂S(g) fugacities of 10^{2.44} and 10^{12.32}, respectively (Equations (45) and (57)). Therefore, if the equilibrium fugacity of CO₂(g) is 10^{-5.5} atm (as calculated by Brush (2005) for a system containing MgO), the fugacity of H₂S(g) is 10^{-7.9} atm (i.e. 10⁻² ppm) and 10^{-17.8} atm (i.e. 10⁻¹² ppm), for Fe and Pb, respectively. Using the same argument as preceding section, we suspect that the kinetics of the reaction between CO₂(g) and MgO would not be overwhelmingly faster than that of CO₂(g) with Fe or Pb; therefore, the pressure of CO₂(g) will probably be higher than 10^{-5.5} atm for an extended period of time and in turn the pressure of H₂S(g) will be higher than 10^{-7.9} or 10^{-17.18} atm. If we maintain CO₂(g) at 350 ppm, as explained in the previous section, the H₂S(g) fugacity should be maintained at least at 1.3 and 2×10^{-10} ppm, for the Fe and Pb systems, respectively. But if CO₂(g) is maintained at 1,000 ppm, the H₂S(g) fugacity should be maintained at least at 3.6 and 5×10^{-10} ppm, for the Fe and Pb systems, respectively. However, as with CH₄, H₂S(g) presents significant environmental health and safety concerns – as such, to mitigate these concerns the Permissible Exposure Limit (PEL) for H₂S(g) is 20ppm (ceiling); exposure to 100ppm is immediately dangerous to life or health.

9.1.3 Presence of Organic Ligands in the Brine

The WIPP waste will contain significant amounts of acetate, citrate, EDTA, and oxalate, at closure time. Brush and Xiong (2005b) calculated the concentration of these organic ligands

for the WIPP PA baseline calculations (PABC); the results are presented in Table 15. These ligands are important to consider for the WIPP PA, as they influence the solubility of the actinides in the WIPP. Furthermore, the literature indicates that all of these species can have a significant impact on the electrochemical behavior of both Fe and Pb.

Table 15. Concentrations of Organic Ligands for a Homogeneous 10-Panel Repository.

Organic Ligand	Organic Ligand concentrations in PABC (M)
Acetate	1.06×10^{-2}
Citrate	8.06×10^{-4}
EDTA	8.14×10^{-6}
Oxalate	4.55×10^{-2}

In the case of steel, acetate has been found to enhance the dissolution rate in oilfield brines by stimulating cathodic activity at the Fe surface (Pletcher, 2005). Acetic acid has been found to similarly enhance the corrosion of Pb alloys. (Sankaeapapavinasam, 1989a) Conversely, both oxalic acid (Saltykov, 2004) and EDTA (Shukla, 2004) have been found to effectively inhibit the corrosion of carbon steels. Oxalic acid has also been found to inhibit corrosion on Pb alloys (Sankaeapapavinasam, 1989b). Finally, citric acid is widely used in the removal of corrosion product from Fe surfaces, where it readily complexes with Fe (Kubal, 1995).

While none of these studies have evaluated the impact which low concentrations will have in WIPP relevant brines, they do strongly suggest that the organic ligands may have an impact on the corrosion process. As such, they will be incorporated into the brines used in this study.

9.2 Tasks List

9.2.1 Task 1: Brine Preparation

The experiments will be performed using two WIPP-representative brines or some derivative of these brines. The two brines in questions are the ERDA-6, which represents fluids from reservoirs in the Castile Formation and the GWB, which represents intergranular brines from the Salado Formation at or near the stratigraphic horizon of the repository. The

compositions of these brines are presented in Table 16. The preparation of these brines has been discussed elsewhere (Robinson, 1996; Snider, 2003).

Table 16. Compositions of GWB and ERDA-6 Prior to Equilibration with MgO.

Element or Property	GWB ¹	ERDA-6 ²
B(OH) _x ^{3-x}	158 mM	63 mM
Na ⁺	3.53 M	4.87 M
Mg ²⁺	1.02 M	19 mM
K ⁺	467 mM	97 mM
Ca ²⁺	14 mM	12 mM
SO ₄ ²⁻	177 mM	170 mM
Cl ⁻	5.86 M	4.8 M
Br ⁻	26.6 mM	11 mM
Total inorganic C (as HCO ₃ ⁻)	-	16 mM
pH	-	6.17
Sp. gr.	1.2	1.216

With time, a portion of the engineered barrier (MgO) will dissolve in the brine present within the WIPP, altering its composition. Brush (2005) published the compositions of both GWB and ERDA-6 brines following equilibration with MgO and in the presence of the anticipated concentration of organic ligands discussed in Section 9.1.3. These brine compositions were calculated for the PABC, using the geochemical speciation and solubility code Fracture-Matrix Transport (FMT) (Babb and Novak, 1997). The calculations were conducted with the assumption of instantaneous, reversible equilibria among GWB or ERDA-6, major Salado minerals such as halite (NaCl) and anhydrite (CaSO₄), and the MgO hydration and

¹ Snider, 2003

² Popielak et al., 1983

carbonation products $\text{Mg}(\text{OH})_2$ and $\text{Mg}_5(\text{CO}_3)_4(\text{OH})_2 \cdot 4\text{H}_2\text{O}$ buffering chemical conditions, such as f_{CO_2} , pH, and brine composition. These brine compositions are presented in Table 17.

Table 17. Compositions of GWB and ERDA-6 after Equilibration with MgO , in the Presence of Organic Ligands (Brush, 2005).

Element or Property	GWB ¹	ERDA-6 ²
$\text{B}(\text{OH})_x^{3-x}$	70.0 mM	23.4 mM
Na^+	4.35 M	5.243 M
Mg^{2+}	0.503 M	138 mM
K^+	0.514 M	96.1 mM
Ca^{2+}	7.40 mM	9.08 mM
SO_4^{2-}	228 mM	179 mM
Cl^-	5.65 M	5.24 M
Br^-	27.8 mM	10.9 mM
Total inorganic C (as HCO_3^-)	0.0422 mM	0.0790 mM
pH	8.69	8.94
Sp. gr.	1.23	1.22
Uncomplexed ³ Acetate	5.70 mM	6.97 mM
Uncomplexed Citrate	0.0173 mM	0.0189 mM
Uncomplexed EDTA	8.37×10^{-11} M	1.74×10^{-11} M
Uncomplexed Oxalate	0.0121 mM	0.00638 mM

¹ FMT run output 7

² FMT run output 11

³ Sum of the ligand concentration, as deprotonated or protonated, but not complexed to a metal.

However, these brine chemistries were calculated with a $\text{CO}_2(\text{g})$ partial pressure of $10^{-5.5}$ atm, which might not be appropriate for our experiments, as discussed above. We have chosen to use a higher $\text{P}_{\text{CO}_2(\text{g})}$ than $10^{-5.5}$ atm, as presented in Section 9.1.2. We will attempt to calculate the brine compositions resulting from the equilibration of ERDA-6 and GWB with MgO, under a $\text{P}_{\text{CO}_2(\text{g})}$ relevant to our experiments (e.g. 350 ppm), using the geochemical code FMT. Additionally, we will attempt to determine the brine composition resulting from the equilibrium of ERDA-6 and GWB with MgO, at pH higher and lower than pH 9. If successful, we will run experiments with the resulting brines. Brines may interact with steel and Pb alloys in the repository, prior to equilibration with MgO; in such case, the brine pH is lower than 9. On the other hand, the presence of calcite may lead to higher pH than 9. If we are unable to calculate the resulting brine composition for higher $\text{P}_{\text{CO}_2(\text{g})}$, we will use the composition presented in Table 17. Therefore, this task has two goals – first, to determine the relevant brine compositions via calculation, and second, to develop a method to synthesize the aforementioned brines. We will perform experiment in presence and in absence of organic ligands (acetate, citrate, EDTA, and oxalate). The concentration of organic ligands to be used is yet to be determined; we will probably use larger concentrations than indicated by the code calculations to compare to the results obtained without ligands. If we determine that organic ligands influence the system, we will study the influence of a variation of ligand concentrations.

9.2.2 Task 2: Construction and Validation of a Mixed Flowing Gas Exposure System

In order to perform the atmospheric and aqueous experiments needed to assess the tendency for Fe and Pb to form carbonates in the WIPP following room closure, a system capable of maintaining the applicable environmental conditions (see Section 9.1.2) must be assembled. The system described below will enable this environment to be accurately achieved and reliably maintained throughout the course of this testing.

The system itself can be broken down into three general parts – the gas supply subsystem, the gas mixing and exposure chambers, and the gas analysis subsystems. The following paragraphs detail each of the aforementioned subsystems.

In order to assure that the purity of the gas supply is maintained within acceptable limits, gas will be delivered from a series of compressed gas tanks supplied by an appropriate vendor. Tanks will be manifolded together as needed to provide the desired flow rates. There will be two source gas streams in this study – the first being the dry gas stream, and the second being a humid gas stream. The gas distribution system itself is illustrated in Figures 2 and 3. As indicated in the figures, each of the gas streams will be passed through an O_2 getter prior to delivery to the exposure chamber, ensuring that the O_2 content is maintained below 50 ppb.¹ Gas

¹ The source gas for the exposure system will be effectively 100% nitrogen (with appropriate additions of CO_2 and/or H_2S). As such, the gas stream will likely be sufficiently oxygen free so as to not require the use of getters during normal operation. However, during gas tank changes or other disturbances to the gas delivery system, air (and thus oxygen) may be introduced into the gas stream. In order to compensate for this effect, along with any

for both streams will be drawn from the supply tanks through mechanical flow regulating valves which ensure that the flow rate remains constant independent of the supply pressure (thus the supply pressure will not deviate as the supply tanks are depleted and decrease in pressure). The actual flow rates will be continuously monitored and logged via mass flow meters. Since the target humidity level within the test environment is 70%, 70% of the total gas flow sent to the exposure chamber will be in the form of N₂ which has been humidified to 100% relative humidity (which will later be mixed with the remaining 30% of the gas stream which will be dry). Humidification will be accomplished through the use of a simple saturator – the dry N₂ gas will be passed through a dispersion system and bubbled through warm (40°C) deionized water where it becomes saturated with moisture (at this point, the gas stream will be 40°C and 100% relative humidity). Once it has been through the humidifier, the gas will be passed into a condenser (similar in concept to the saturator) which is at the target temperature of 30°C. At this point, the gas will be brought to the target temperature and any liquid moisture will be removed from the gas stream. Once the humidified gas stream has passed through the condenser, it will be sent to the main mixing chamber prior to passing into the exposure chamber (described below).

The second leg of the gas delivery system consists of the dry contaminant stream. Here again mechanical flow regulators will be used to ensure a constant delivery rate of gas – in this case, both CO₂ (or a CO₂/ N₂ mixture) and dry N₂ will be utilized. The flow from both gas streams will be monitored with mass flow meters, and the flow rates logged as a function of time. The N₂ and CO₂ containing dry gas streams will then pass into a mixing chamber, after which they will be delivered to the temperature control chamber, where they will be mixed with the 100% relative humidity N₂ gas stream discussed above. The flow rate of the CO₂ stream will be set such that the desired CO₂ level is achieved within the exposure chamber.

The humid and dry gas streams described above will both flow into a second mixing chamber where they will mix and be brought to the desired temperature. After passing through the mixing chamber, the gas stream, now at the desired humidity and CO₂ concentration, will be delivered to the exposure chamber, which it will flow through, as illustrated in Figure 3. The exposure chamber will be located (along with the condenser and second gas mixing chambers described above) within a temperature controlled incubator. The temperature control system will be selected such that the temperature within the system is maintained irrespective of the external environment (i.e., the system should be capable of heating and cooling). The exposure chamber itself will be sized such that all of the proposed experiments (described below) can be housed within it. In addition, electrical and mechanical feed-throughs will be incorporated such that periodic removal of specimens, performance of rudimentary electrochemical experiments, and sampling of brine compositions can be performed.

In order to allow exposure to gas streams in addition to CO₂ – in this case, H₂S, another leg must be added to the gas delivery system. This is illustrated schematically in Figure 4. An additional flow control valve will be added which will deliver dry N₂ to a permeation device.

trace oxygen contamination of the nitrogen source gas, oxygen scavengers have been added to the gas supply stream.

The permeation device (permeation tube) is a device which emits a desired specie at a known rate. The permeation device will be placed inside a glass chamber which is held at a constant temperature. The N₂ flow rate into the permeation device chamber will be selected such that the gas concentration exiting the permeation chamber is at the desired level. A flow controller and vent valve combination will then be used to regulate the delivery of the contaminant specie to the dry gas mixing chamber described previously. The gas flows to each of the four reactors are illustrated schematically in Figure 5.

The final portion of the atmospheric corrosion system is the gas analysis segment, shown schematically in Figure 6. Compositional analysis will be performed on the exit stream from the reaction chamber to ensure that the desired concentration is maintained. As the aggressive species are more likely to be depleted/consumed in the reaction chamber, it is highly desirable that the concentration be monitored real-time, rather than periodically. The gas stream will be analyzed for the relative humidity, CO₂, and H₂S level. This may be accomplished utilizing commercially available analyzers capable of detecting H₂S in the low ppb and CO₂ in the low ppm concentration ranges (such devices have been successfully applied to atmospheric corrosion systems commonly used at Sandia in the Corrosion and Electrochemical Science Dept.). In order to minimize the number of detectors required, a series of solenoid valves coupled with control hardware and software (described below) will be used to enable periodic sampling of each gas stream, as illustrated in Figure 6.

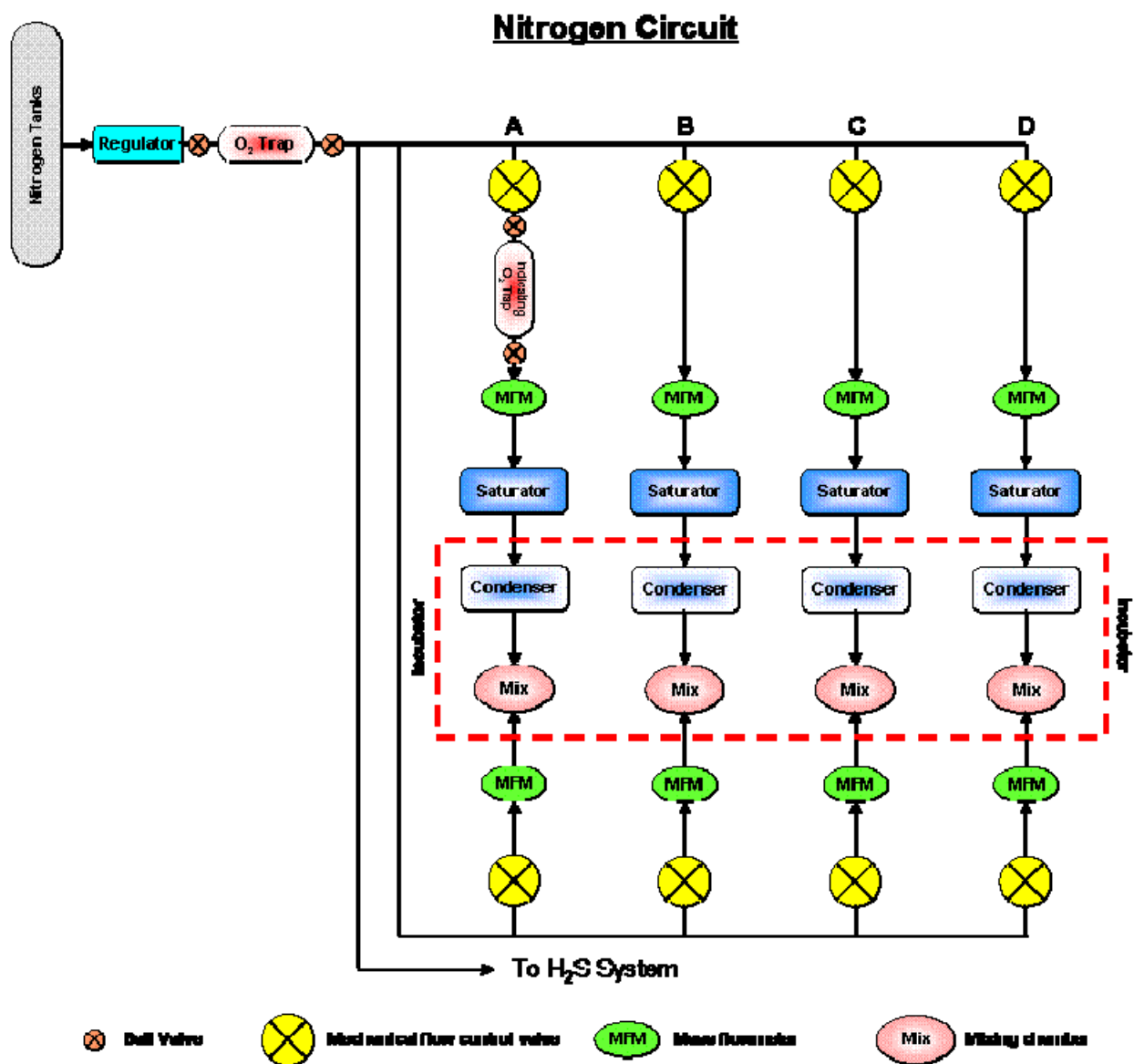


Figure 3. N₂ gas circuit for the gas exposure system. This circuit includes the wet N₂ streams (top portion) as well as the dry N₂ streams. Also shown are two O₂ traps – a large capacity trap in the main supply line, and an indicating trap in one of the wet supply lines.

Carbon Dioxide and Hydrogen Sulfide Circuits

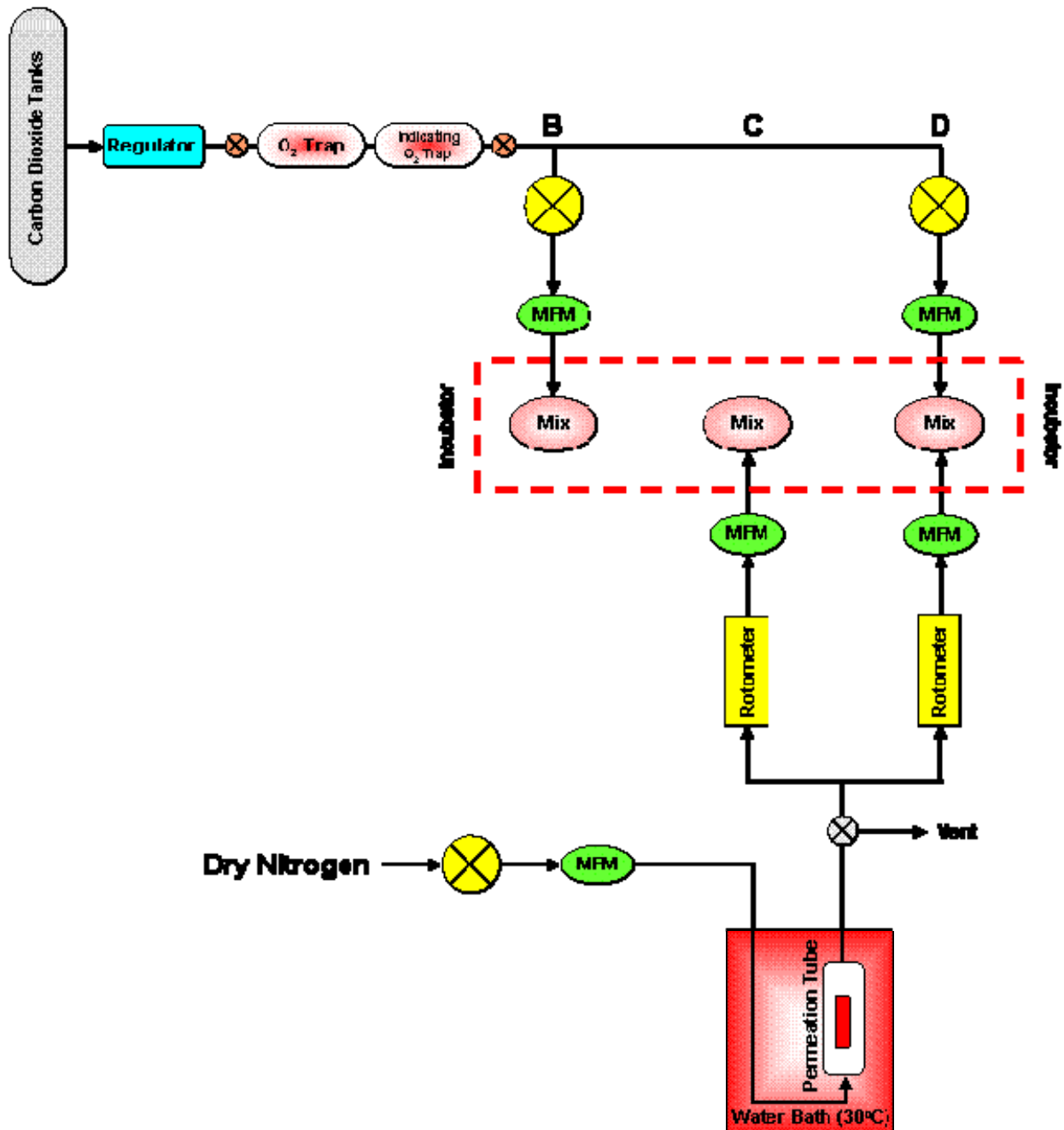


Figure 4. Contaminant gas streams for the gas exposure system. Upper portion of the figure illustrates the CO₂ supply (equipped with O₂ traps similar to those described above). The lower portion illustrates the H₂S gas supply system – note that the supply gas for this leg is dry N₂ and as illustrated in Figure 3.

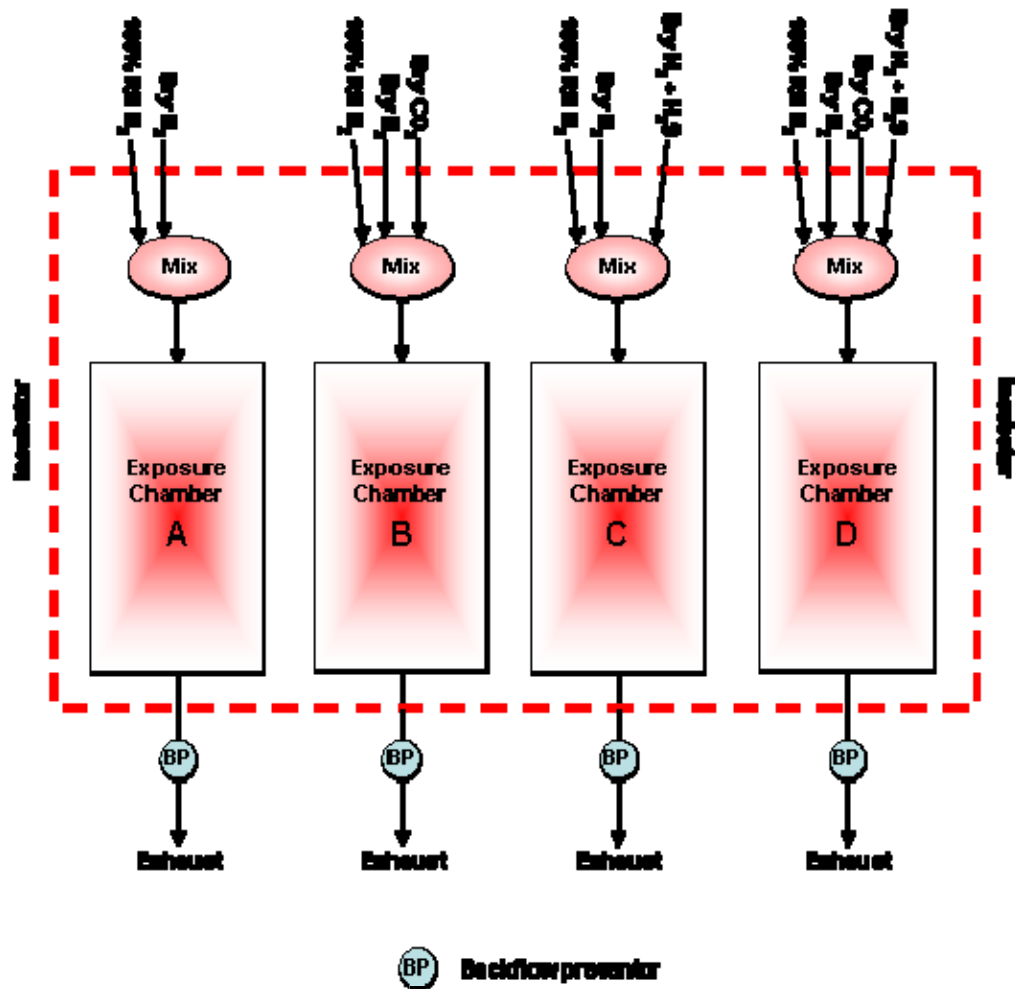


Figure 5. Schematic representation of the gas flow streams passing into each of the four exposure chambers.

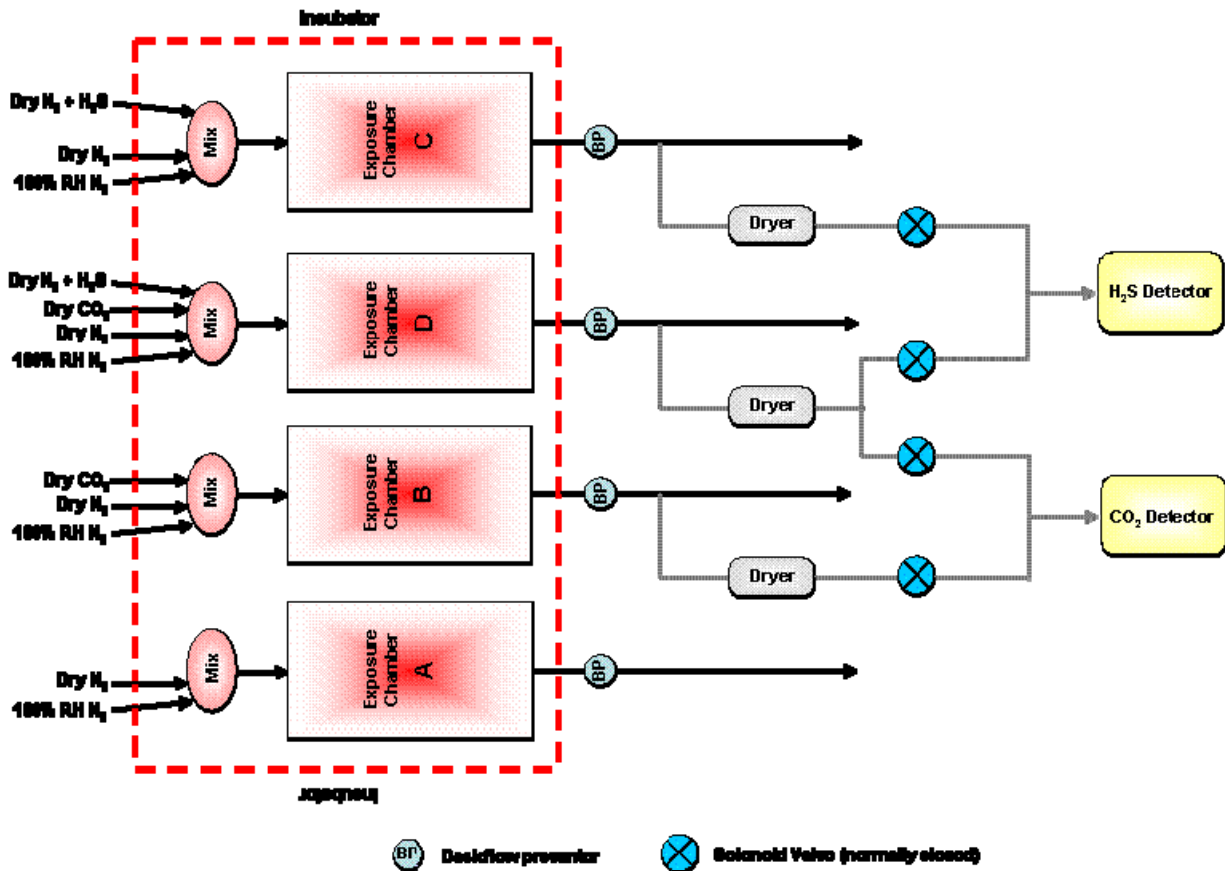


Figure 6. Schematic representation of the gas composition analysis system. This system consists of a series of perma-pure gas dryers, a gas manifold (controlled by solenoid valves) to route the gas to each analyzer, and the two gas analyzers themselves.

9.2.3 Task 3: Software Qualification - Monitoring System and Software for the Mixed Flowing Gas Exposure System

In this task, the data acquisition system and software will be constructed to monitor the mixed flowing gas system defined in the previous task. The procedures defined in NP 19-1 will be followed, and the required documentation generated. The text below summarizes the system and software requirements.

9.2.3.1 PURPOSE

This system will continuously monitor the gas flow rates and compositions throughout the course of the experiment. Warning notices will be incorporated to notify the user of any adjustments which are required to address any deviations from the desired gas composition. Note that the purpose of the system is to monitor only – all flow control will be accomplished through mechanical valving.

9.2.3.2 FORMAT

The data acquisition system will consist of the following components (all National Instruments hardware):

- SCXI-1000 4 slot chassis (system backbone)
- SCXI-1600 Data acquisition and control module
- SCXI-1112 8 channel thermocouple module
- SCXI-1100 32 channel multiplexer amplifier
- SCXI-1124 6 channel isolated DAC module

The data acquisition software will be a routine written in National Instruments LabVIEW – this software will be utilized to monitor mass flowmeters, monitor thermocouples, actuate solenoid valves for the gas sampling system, and acquire data from the gas analysis hardware. The QA process for the software will be conducted in accordance with the procedures defined in NP 19-1.

9.2.3.3 DETAILED TEST SYSTEM DESCRIPTION

In simple terms, there are four portions of the gas exposure system (described in section 9.2.2) – the gas supply, the humidity source, the exposure chamber, and the compositional analysis systems.

The gas source will consist of either pressurized tanks or an appropriate gas generator which supplies high purity N₂ or CO₂ gas (potentially at a range of pressures) to a series of mechanical flow valves. The flow valves route the gas to the other components of the system. The output from each mechanical flow valve is monitored by a mass flow meter, which will in turn be monitored by the software package described here.

The humidity source will take a dry gas stream and increase its humidity to 100%. This is accomplished by passing the gas through a saturator which is essentially a warm bath of deionized water (at a temperature greater than the exposure chamber temperature), then into a condenser which is at the same temperature as the exposure chamber, then finally into the test

chamber itself. In addition to the flow rates described above, the system will also monitor the temperature within each saturator, providing a warning indicator if the temperature drifts outside the acceptable temperature range, signaling the operator to make appropriate adjustments.

The composition analysis system has two subcomponents – the first are the composition analyzers themselves (for CO₂ and H₂S), and the second is a series of solenoid valves which route the gas streams from the exposure chambers to the appropriate detector. The software package will control the solenoid valves (see Figure 6 above) and route the gas stream to the appropriate detector, and acquire data from the detector.

The flow rates (from the flowmeters), temperatures in the saturators and exposure chamber (via thermocouples), and the composition of each gas stream will be monitored and recorded. Simple calculations will be performed to determine the anticipated supply gas compositions based upon measurements taken from the flowmeters. These values will be recorded and then compared to the measured gas composition. Should the two deviate from one another by an unacceptable amount (+/- 15% or 3ppb, whichever is greater, as defined in ASTM B827 (ASTM, 2003a)), a warning message will be displayed indicating that the user must appropriately document the deviation, then manually adjust the supply flows to re-achieve the desired test conditions.

9.2.3.4 PROGRAM PROCESSES/ACTIONS:

1. Monitor flow meters
 - a. Display flow rates on computer screen
 - b. Log data to an excel spreadsheet at a user defined time interval
 - c. Display warning/caution indicator if flows drift out of range
 - d. Present a calculated gas composition based upon flow rates
2. Monitor system temperatures
 - a. Display temperatures on computer screen
 - b. Log data to an excel spreadsheet at a user defined time interval
 - c. Display warning/caution indicator if any temperatures drift out of range
3. Monitor gas chemistry
 - a. Control solenoid valves in multiplexing system to select which gas stream is to be analyzed
 - b. Display measured concentrations on the computer screen
 - c. Log the measured and calculated concentrations of each component to a spreadsheet at a user defined time interval
 - d. Display a warning/caution indicator if the concentrations deviate more than a user defined percentage from the calculated inlet concentrations

9.2.3.5 VERIFICATION OF SOFTWARE FUNCTIONALITY

1. Apply series of known flow rates to each flow meter over a period of time and verify that the data acquisition system properly measures and records the data.

2. Apply series of known temperatures to each thermocouple over a period of time and verify that the data acquisition system properly measures and records the data.
3. Apply a temperature outside the predefined operating window and verify that the system warns the user and then responds properly when the correct parameters are re-established.
4. Verify that the system is able to cycle through the valves and supply a sample gas stream to each composition analyzer from each chamber which it is monitoring.
5. Apply gas of a known composition to each analyzer and verify that the system is able to correctly measure and record the data.
6. Apply gas of a known composition to the system which is outside the predefined operating window to verify that the system warns the user and then responds properly when gas of the proper concentration is supplied.
7. Allow system to run for an extended time period to verify that the code is stable.

9.2.4 Task 4: Evaluation of Carbonation of Fe in WIPP Internal Atmosphere and Likely Equilibrium Brines

Once the exposure system has been constructed and appropriate sample geometries identified, the long term experiments may be initiated. The goal of this task is to determine the tendency of the Fe-based alloys used to construct the drums utilized within the WIPP to consume CO₂ from the in-room environment through the formation of iron carbonates. Coupons will be made from material similar in composition to that found within the WIPP. Samples will be evaluated in three conditions – totally immersed within the brine, partially immersed within the brine, and suspended above the brine. A series of experiments will be performed in parallel for each of the brines defined in Task 1 above.

In addition to the primary corrosion coupons, a series of instrumented samples will be included such that the corrosion rate may be assessed as a function of time. The samples will include a set of three electrodes – a platinum wire (counter electrode), a chloridized silver wire (reference electrode) and a sample of the desired material – electrochemical impedance spectroscopy will be performed to assess the state of the surface as a function of time.

During the course of the experiment, samples will be periodically removed and the corrosion product analyzed to determine the extent of corrosion which has taken place, and assess the quantity of carbonate which has formed (and hence, CO₂ consumed). At a minimum, one set of samples will be removed in the middle of the test (approximately 1 year) and a second set upon completion of the test (approximately 2 years). Note that once removed from the system, samples will not be reintroduced (i.e., once a sample is out, it will stay out). In addition, brine samples will be periodically taken to establish to what degree the solution composition has been altered by the corrosion process. (It should be noted that samples from the bulk brine will not necessarily be indicative of the solution composition which exists at the metal solution interface within the corrosion product layer.) For all corrosion coupons removed from the system, the composition and quantity of corrosion product will be identified. In addition, a weight loss measurement will be taken and converted to an average dissolution rate. Finally, the metal surface will be photodocumented (both before and after the corrosion product has been removed).

9.2.5 Task 5: Evaluation of Carbonation of Pb in WIPP Internal Atmosphere and Likely Equilibrium Brines

The goal of this task is to determine the tendency of the Pb liners within some of the drums utilized within the WIPP to consume CO₂ from the in-room environment through the formation of lead carbonates. Two forms of samples will be evaluated – single Pb coupons compositionally similar to the actual Pb liners, and Pb-Fe galvanic couples (simulating the geometry which exists within the Pb lined drum). These samples will be evaluated in three conditions – totally immersed within the brine, partially immersed within the brine, and suspended above the brine. A series of experiments will be performed in parallel for each of the brines defined in task 1 above. Experiments will be performed following the procedures defined in ASTM G1 (ASTM, 2003b).

In addition to the primary corrosion coupons, a series of instrumented samples will be included such that the corrosion rate may be assessed as a function of time. The samples will include a set of three electrodes – a platinum wire (counter electrode), a chloridized silver wire (or other similar reference electrode) and a sample of the desired material – electrochemical impedance spectroscopy will be performed to assess the state of the surface as a function of time.

During the course of the experiment, samples will be periodically removed and the corrosion product analyzed to determine the extent of corrosion which has taken place, and assess the quantity of carbonate which has formed (and hence, CO₂ consumed). At a minimum, one set of samples will be removed in the middle of the test (approximately 1 year) and a second set upon completion of the test (approximately 2 years). Note that once removed from the system, samples will not be reintroduced (i.e., once a sample is out, it will stay out). In addition, brine samples will be periodically taken to establish to what degree the solution composition has been altered by the corrosion process. (It should be noted that samples from the bulk brine will not necessarily be indicative of the solution composition which exists at the metal solution interface within the corrosion product layer.) For all corrosion coupons removed from the system, the composition and quantity of corrosion product will be identified. In addition, a weight loss measurement will be taken and converted to an average dissolution rate. Finally, the metal surface will be photodocumented (both before and after the corrosion product has been removed).

9.2.6 Task 6: Systematic Evaluation of Fe Corrosion in Sulfide-Bearing Brines

The objective of this task is to quantify the effects of dissolved sulfide on the corrosion behavior of steel. The experiments will be carried out in a flow-through system over a flow-through, temperature, pH, ionic strength and sulfide interval. As discussed in more detail below the corrosion rate will be quantified by several independent methods. The paragenetic suite of phases will also be characterized by SEM.

9.2.7 Task 7: Determination of Fe Corrosion Products from Roselle (2013) Study

An attempt to understand the effects of the corrosion product can begin only if the corrosion products are positively identified, and the weight fraction of each iron phase is determined.

Obtaining qualitative and quantitative information regarding the elemental composition and phase identification can be used to aid in characterization of corrosion products. Compounds usually found in iron corrosion coatings include goethite (α -FeOOH), lepidocrocite (γ -FeOOH), magnetite (Fe_3O_4), siderite (FeCO_3), ferrous hydroxide ($\text{Fe}(\text{OH})_2$), ferric hydroxide ($\text{Fe}(\text{OH})_3$), ferrihydrite ($5\text{Fe}_2\text{O}_3 \cdot 9\text{H}_2\text{O}$), green rusts (e.g., $\text{Fe}_4(\text{II})\text{Fe}_2(\text{III})(\text{OH})_{12}(\text{CO}_3)$) and calcium carbonate (CaCO_3) (Benjamin et al., 1996). Depending on the composition of the water (in brine), corrosion of iron may result in the formation of relatively soluble Fe(II) solids such as siderite and ferrous hydroxide. In the presence of carbonic species, siderite (FeCO_3) is the stable ferrous solid (Singer and Stumm, 1970). Furthermore, green rusts are hydrated ferrous–ferric compounds having Cl^- or SO_4^{2-} or CO_3^{2-} anions (Olowe et al., 1988; Drissi et al., 1994; Génin et al., 1997; Refait et al., 1998). These compounds are formed during the partial oxidation of ferrous hydroxide in the presence of other anions. It should also be pointed out that in the first writing of TP 06-02, very little was known about “green rust”, Since the findings from Roselle, the importance of green rust is now understood, and in this Test Plan and Analysis Plan (AP)-175, the role played by this phase in corrosion of steel will be examined. The corrosion reactions will be established and compared to previous reaction pathways.

Analytical methods such as XRD analysis, SEM/EDS, UV-Vis, EPMA, Mossbauer and/or Raman Spectroscopy will be used to qualitatively and quantitatively identify the corrosion products and weight fraction of each iron phase that formed during Roselle’s corrosion experiments. This information will then be used to formulate the appropriate corrosion reactions for iron. Once the corrosion products have been determined according to this Test Plan Revision, the methods outlined in the Approach Section of AP-175, Rev. 0 will be used to calculate gas generation rates for each of Roselle’s experiments.

9.3 Test Matrix

9.3.1 General Environmental Parameters

Temperature: 28°C

Basis: Temperature measurements made within WIPP Room H (Munson, 1987)

Relative Humidity: 72%

Basis: Based upon the FMT calculations performed by Brush (Brush, 2005), the anticipated relative humidities in the headspace over each of the brines being evaluated in this study are effectively equivalent. As such, all of the brines for a given atmospheric condition will be held within the same mixed flowing gas chamber.

9.3.2 Materials to be Evaluated

Iron: ASTM A1008 and ASTM A36 carbon steels

Basis: The majority of the containers within the WIPP are drums of various sizes, all of which are constructed of ASTM A1008 compliant material. The second most prevalent Fe alloy is ASTM A36 carbon steel which is used in the large boxes, 10 drum overpacks, etc.

Lead: chemical-copper lead (UNS L51121)

Basis: While the Pb alloy used within the RH waste containers is not specifically called out, this grade is the one commonly used for chemical processing, corrosion performance, etc. (QQ-L-171e grade C)

9.3.3 Atmosphere

Atmosphere 1: N₂

Atmosphere 2: N₂ + CO₂

Atmosphere 3: N₂ + H₂S

Atmosphere 4: N₂ + CO₂ + H₂S

Basis: As discussed above, the predicted atmosphere within the WIPP resulting from microbial consumption of the CPR materials in the waste will be a combination of inert (e.g., CH₄) and active (e.g., CO₂ and H₂S) gasses. In these experiments, N₂ will be substituted for CH₄ as the inert carrier gas to ease ES&H concerns, with both CO₂ and H₂S as potentially aggressive species.

9.3.4 Brine Compositions

Chemistry 1: ERDA-6 (Synthetic Castile Formation brine)

Chemistry 2: GWB (Synthetic Salado Formation brine)

Basis: These two brines are the predicted compositions which will come into contact with the waste over time.

Chemistry 3: ERDA-6 after equilibration with Periclase, halite, and anhydride

Chemistry 4: GWB after equilibration with Periclase, halite, and anhydride

Basis: Equilibration of the two anticipated brine chemistries with the engineered barrier.

Organic Ligands (EDTA, Oxalate, Acetate, and Citrate)

Chemistry 5: Chemistry 1 + Organic Ligands

Chemistry 6: Chemistry 2 + Organic Ligands

Chemistry 7: Chemistry 3 + Organic Ligands

Chemistry 8: Chemistry 4 + Organic Ligands

Basis: Organic ligands, while typically omitted from WIPP exposure experiments, have been found to impact the electrochemical behavior of both Fe and Pb alloys. As such, all four of the previously defined brine chemistries will also be evaluated with the organic ligands present.

9.3.5 Sample Positioning

Atmospheric (exposed only to atmosphere)

Partially Inundated (located at waterline)

Inundated (submerged within brine under atmosphere)

Basis: Due to the limited quantity of brine which is predicted to permeate into the waste, it is reasonable to assume that not all of the material will come into contact with liquid brine. As such, all three materials identified above will be evaluated while inundated with brine, while exposed only to the humid atmosphere which will exist above the brine, and while partially immersed in the brine (half below the

surface of the brine, half above it). In the latter case, care will be taken to insure that the samples are not subject to splashing from the brines. Furthermore, care will be taken to minimize any sample stirring to avoid disturbing the corrosion product layers or altering the distribution of locally depleted species. Partially immersed samples have been added to the test matrix in an effort to more thoroughly explore the waterline results observed by Telander and Westerman (Telander and Westerman, 1993; 1997) where the nature and chemical composition of the corrosion product differed from regions away from the waterline. Furthermore, as the material within the WIPP will likely not be completely immersed in brine, these tests will broaden our understanding of the corrosion processes and products likely to be present.

9.3.6 Experimental design

Each of the alloys described above will be exposed to the four brines in each of the four atmospheres. Due to the similar humidity which would result at equilibrium over each brine, all four brines will be evaluated simultaneously in each atmosphere, necessitating the four chamber system described in Section 9.2.2. As such, within each chamber there will be:

- Samples of each material (minimum of three replicates) suspended in the atmosphere, away from the vessels containing brine
- Samples (minimum of three replicates) of each material in each of the four brines

9.3.7 Systematic Evaluation of Fe Corrosion in Sulfide-Bearing Brines

In the new experiments, we will investigate the effects of sulfide on steel corrosion, not by filling a chamber with H₂S(g) at a certain partial pressure, but by adding NaHS to solution. The experiments will be carried out in an anoxic glove box with solutions in closed containers to minimize the formation of H₂S(g). According to Barrett et al. (1988), the solubility of H₂S in water as a function of NaCl(m) at 90°C is:

Table 18. Solubility of H₂S in NaCl Solutions

NaCl (m)	Moles H ₂ S/kg H ₂ O	NaCl (m)	Moles H ₂ S/kg H ₂ O
0	0.01323	3	0.00993
1	0.01181	4	0.00943
2	0.01090	5	0.00886

According to Zheng et al. (2014b), the concentration of HS⁻ in solution depends on the fugacity of H₂S and the pH:

$$C_{HS^-} = K_{H_2S} f_{H_2S} / C_{H^+} \quad (63)$$

Where K_{H_2S} is the Henry's Law constant, f_{H_2S} is the fugacity of H₂S, and C_{H^+} is the concentration of H⁺ in solution.

K_{H_2S} can be calculated from the formula:

$$10^{(a+bT+cT^2+dT^{-1}+e\ln T_k)} \quad (64)$$

where a, b, c, d and e are constants (Table 19) and T_k is the temperature in Kelvin.

Table 19. Henry's Law Constants

Constant	value
a	782.43945
b	0.361261
c	-1.6722×10^{-4}
d	-20565.7315
e	-142.741722

Using a value of $10^{-6.9}$ for the fugacity of H_2S (as suggested elsewhere in this document), concentration of HS^- in equilibrium with the gas phase in the repository at $pH = 9$, is: 1.14×10^{-5} m. The envisioned experiments will evaluate how sulfide interacts and enhances corrosion of steel products in brine solutions.

In the new set of experiments, we will emphasize parameterization of the rate equation in brines of various ionic strength and sulfide concentration. In particular, the experiments will be run in a NaCl-free and synthetic NaCl brine solutions of 1, 2, 3, 4 and 5 molal concentration. The sulfide content will span concentrations of 0 to 1×10^{-3} molal S. Sulfide concentrations in the solution will added by mixing NaHS into deionized water. The solution pH will be manipulated using HCl or NaOH. To start, the solution pH will be set at 9 and future experiments will examine the effects of pH on steel corrosion.

9.3.7.1 Methodology

Steel coupons will be polished to <50 nanometers and the surface features will be inspected and recorded by vertical scanning interferometry (VSI). Imaging of the sample surfaces will also be conducted using SEM. Element mapping of the coupons will indicate how trace metals (Al, Cr, Cu, Mn, Mo and Ni) are distributed in the Fe matrix. The dimensions of the coupons will be measured with digital calipers and the SA (surface area) computed. Because the density of the coupons is known independently, the calculated volume of the coupons, from the measuring their dimensions, coupled with mass measurement, will yield a density value that can be compared with that which is independently known. If the two values accord, then it can be assumed that the computed SA is accurate. The coupons will then be placed in 180 mL capacity reactors (2.59 inch diameter, 2.98 inches high) in an anoxic glovebox. The reactors will be situated in a "dry bath" type heater block assembly that can accommodate four reactors. The temperature of the dry bath will be controlled by feedback thermocouple device that automatically adjusts the temperature to the set value. The reactors are Savillex jar-style containers with a lid containing two ports, one for ingress the other for egress of solution. Thus, these experiments differ substantially from those carried out by Greg Roselle in that the former were "static" and those proposed herein will be flow-through experiments. The principal virtue of flow-through experiments is that solution saturation state and pH are maintained at constant values, allowing for a more straight-forward evaluation of dissolution rates. A portion of the surface will be masked using Permatex silicone-based sealant; the reason for this is discussed

below. The effluent solution exiting the reactor will be collected continuously in sealed vessels. Because the sulfide in the input solution will react with iron in the reactor to make iron sulfides, we anticipate that the effluent solution will contain only low concentrations of sulfide. Accordingly, the amount of H₂S in the effluent solution container headspace will be very low and will not pose a significant environmental threat. Prior to addition of the steel coupons, three blank samples will be collected.

Input and effluent solutions will be analyzed in a variety of ways. Aliquots of the starting solution will be retained in capped vials and kept in the anoxic chamber until analyzed. Both input solutions, blanks, and effluent solutions will be assayed using UV/Vis for ferrous iron using the ferrozine method and sulfide using the copper sulfate method. Preparation of the solutions will be conducted in the anoxic chamber and calibration curves created on the day of analysis. Total iron, Al, Cr, Cu, Mn, Mo, Na, and Ni will be determined using ICP-AES and ICP-MS.

The rate of dissolution of the iron coupons will be determined in the following ways:

1. *By Chemical Assay.* The dissolution rate of the steel coupons [mol/(m²·s)] can be computed through knowledge of the concentration of Fe in solution (C_{Fe}), the flow-rate (v), and the surface area (SA) of the coupon:

$$\text{rate} = C_{Fe} \cdot v / SA \quad (65)$$

The dissolution rate is measured when the system comes to steady-state; i.e., when the concentration of Fe in solution becomes invariant with time. In a similar manner, the dissolution rate with respect to the release of the minor elements can also be computed using the above equation (the concentrations of these elements in the coupons are known). In general, the dissolution quantified using this equation accurately determines the rate, but because it is likely in this context that released Fe will reprecipitate in the form of an iron sulfide, the apparent rate may be too slow. In addition, the minor elements may partition into the iron sulfides, sorb onto the corroding surface of the coupon, or form their own precipitates. If this occurs, then the rates of release of these metals will also yield inaccurate rate data (although the effects might be minor).

2. *By Weight Loss Measurement.* The dissolution rate can be calculated from the loss of mass of the coupon over time. This is the method discussed in Roselle (2009; 2010; 2011a; 2011b) and we will follow this methodology. The shortcomings of this method have, at their root, the same problem as with element release (#1 above); if Fe reprecipitates in the form of sulfides, the actual weight loss measured may not be a true indication of the dissolution rate. In fact, the data in these reports documented weight *gains* in some of the coupons from the experiments. Clearly, another method for determining rates on iron coupons dissolving into solution is needed.

3. *By Measurement of Surface Retreat.* An alternative method for determining dissolution rates of materials is to directly measure the surface retreat. In order to do this, a reference surface, against which surface retreat can be compared, must be preserved, and a

method for measuring minute height differences between the reference and reaction surfaces must be employed. Such a technique for determining the dissolution of minerals has been documented (e.g., Arvidson et al, 2003; Lüttge et al., 2003). The method includes masking a portion of the surface of the mineral with a water-proof adhesive, such as the commercially-available silicone-based adhesives, and then subjecting the mineral to dissolution experiments in which the unmasked portion of the mineral surface dissolves and retreats. At the termination of the experiment the mineral is withdrawn from the reactor and the masking agent removed. The height difference between the preserved reference and the reacted and retreated surface can then be measured with an interferometer, a device that resembles a microscope, but is outfitted with special objectives that utilize reflected light from the surface to measure very small height differences. Because the magnitude of the height difference is proportional to the rate of dissolution, the rate can be determined rapidly and without the need for time-consuming sample preparation.

Rates [g/(m²·s)] can be determined by:

$$rate = \rho \Delta h / \Delta t \quad (66)$$

where ρ is the sample density, Δh is the height difference and Δt is the elapsed time.

Because the surface retreat is a direct measurement, the rate of corrosion that is commonly reported in the engineering literature (retreat velocity), in units of mm/y, can easily be determined. The potential drawback of this method is that if a thick corrosion layer develops on the steel surface and if secondary mineral formation coats the surface, the actual surface retreat measurement may be affected. However, even this potential effect can be dealt with by carefully cutting the coupon and measuring the thickness of the corrosion layer using an SEM.

The dissolution rates of the coupons, determined by these three methods, will be compared and the most accurate values will be recommended. Experiments will be conducted in duplicate to ensure the consistency of results. Because the rate of dissolution is slow at room temperature, the experiments will be carried out at higher temperatures (90°, 70° and 50°) before they are conducted at 30°C. In this way, we can project the rates to lower temperature, which will help us in determining if the rates at 30°C are truly at steady-state. In addition, the activation energy of dissolution can also be calculated, further parameterizing the rate equation.

The activation energy of the corrosion reaction can be quantified by regressing rate data as a function of inverse temperature using an Arrhenius-type equation:

$$\log (k_1/k_2) = E_a/2.303R*[1/T_2 - 1/T_1] \quad (67)$$

where k_1 and k_2 are the rate coefficients (mol/sec) at temperature (T in K) 1 and 2, respectively, E_a is the experimental activation energy (kJ/mol) and R [kJ/(mol·K)] is the gas constant.

In order to properly calculate gas generation rates, a proposed mechanism of corrosion pathways, from the characterization of the steel corrosion products from Roselle's 2013 work, is

needed. Thus, a variety of coupons will be selected to represent conditions, in the WIPP for the following possible characterization.

1. SEM/EDS - Use of a scanning electron microscope (SEM) is advantageous because it generates high resolution images to reveal morphology. In some cases, phases can be identified by their morphological expression alone (e.g., magnetite as dioctahedral pyramids). The top surface of the dried coupons was previously studied using scanning electron microscopy SEM/EDS and reported (Roselle, 2009; 2010; 2011a, 2011b, 2013).
2. XRD - X-Ray diffraction analysis examines powder samples to characterize crystalline materials. Powder diffraction is a type of XRD that analyzes uniformly sized, fine powder samples typically containing multiphase and randomly oriented crystals. Since iron oxides readily form stable crystalline phases, X-ray diffraction will be the preferred method for compound identification.
3. Wet Chemistry Method - The Fe(II)/Fe(III) ratio of the powdered corrosion coating can be measured by wet chemistry methods. Samples will be dissolved in an acidic solution concentrated HCl and de-ionized (DI) water. The ferrous and total iron concentrations can then be determined using bathophenanthroline, following the method proposed by Lee and Stumm (1960). A UV/Vis Spectrophotometer will be used to analyze the absorbance of the prepared samples.
4. Mossbauer and/or Raman Spectroscopies - Mossbauer and Raman spectroscopies can be used for studying corrosion coatings and both have proven useful for uniquely identifying the different iron oxides present (Oh et al 1996; Leidheiser et al 1982; Yamashita et al 1994; and Dunnwald and Otto 1989). The advantage of Raman spectroscopy over XRD for phase identification is that Raman can obtain diagnostic spectra on amorphous phases, as well as crystalline. The XRD technique can provide a diffractogram of an amorphous material, but with peak broadening and a decrease in peak intensity, it is typically very difficult to make accurate identifications. Therefore, in these circumstances, Raman spectroscopy would be preferred. Mossbauer spectroscopy is also extremely useful for identifying phases, even if they are not fully crystalline. Mossbauer spectroscopy, when performed at very low analytical temperatures, can distinguish between Fe(II) and Fe(III) (or mixed redox phases) based upon characteristic absorption spectra. These techniques will be employed upon resource availability.
5. EPMA – Electron probe microanalysis can be used to establish the composition of small areas on the steel coupons. EMPA is one of several particle-beam techniques. All elements (except H, He, and Li) can be detected because each element has a specific set of X-rays that it emits. This analytical technique has a high spatial resolution and sensitivity, and individual analyses are reasonably short, requiring only a minute or two in most cases. Additionally, the electron microprobe can function like a scanning electron microscope (SEM) and obtain highly magnified secondary- and backscattered-electron images of a sample.

The entire range of experimental variables pertaining to the steel experiments is summarized in Table 20. This combination of experimental conditions, material types and time segments results in 144 unique experiments. In addition, three replicate coupons were used for each of the experimental conditions resulting in a total of 432 coupons. From this set of steel coupons an appropriate sampling pool will be selected for characterization testing.

Table 20. Experimental Test Matrix	
Condition	Variable
Material Type	ASTM A1008 Steel
	Brine
	GWB
	GWB with organics
	ERDA-6
Sample Positioning	ERDA-6 with organics
	Fully Innundated
	Partially Submerged
Atmosphere	Humid Atmosphere
	0 ppm CO ₂ (balance N ₂)
	350 ppm CO ₂ (balance N ₂)
	1500 ppm CO ₂ (balance N ₂)
Time Segment	3500 ppm CO ₂ (balance N ₂)
	6 months
	12 months
	18 months
Fixed Properties	24 months
	Temperature -26 °C

The characterization of iron phases using these techniques can be applied to further study corrosion products formed on different steels and in different atmospheric environments.

10 SAMPLE CONTROL – DATA QUALITY CONTROL

10.1 Sample Control

The sample control for the work under this Test Plan will follow NP 13-1. Each sample will be appropriately labeled. Sample preparation, utilization, and final disposition will be documented. When samples are not in the possession of individuals designated as responsible for their custody, they shall be stored in a secure area with associated documentation (e.g. SNL WIPP Activity/Project Specific Procedure (SP) Form SP 13-1-1, “Chain of Custody”).

10.2 Data Acquisition Plan

Data collection procedures are specific to individual instruments. For details of the data acquisition for a particular instrument, see the SP or User’s Manual for that instrument. Any data acquired by a data acquisition system (DAS) will be attached directly to the Scientific Notebook or compiled in separate loose leaf binders with identifying labels to allow cross reference to the appropriate Scientific Notebook, as indicated in the Scientific Notebooks Procedure NP 20-2. If the instrument allows data to be recorded electronically, copies of the data disks will be submitted to the Waste Isolation Pilot Plant (WIPP) Records Center according to NP 17-1 “Records.” If possible, data files may be transferred to an electronic storage device (e.g. ZIP disks or CD ROM) for submittal to the records center. For instruments that do not have direct data printout, the instrument readings will be recorded directly into the scientific notebook or in a separate loose leaf binders (scientific notebook supplements per NP 20-2) with identifying labels to allow cross reference to the appropriate Scientific Notebook, as indicated in the Scientific Notebooks Procedure NP 20-2. Current versions of the DAS software will be included in the SNL WIPP Baseline Software List, as appropriate.

Quality control of the Scientific Notebooks will be established by procedures described in NP 20-2 “Scientific Notebooks.” Methods for justification, evaluation, approval, and documentation of deviation from test standards and establishment of special prepared test procedures will be documented in the Scientific Notebooks. Procedures including use of replicates, spikes, split samples, control charts, blanks and reagent controls will be determined during the development of experimental techniques.

The numerical data will be transferred from data printouts, electronic media, and scientific notebooks to Microsoft Excel (Office 2003 version or later) spreadsheets. Data transfer and reduction shall be performed in such a way to ensure that data transfer is accurate, that no information is lost in the transfer, and that the input is completely recoverable. A copy of each spreadsheet will be taped into the scientific notebook.

10.3 Data Identification and Use

All calculations performed as part of the activities of this test plan will be documented in scientific notebooks. The content and organization shall follow the Scientific Notebook Procedure NP 20-2. The notebooks will be reviewed periodically for technical and QA content and adequacy, as explained in the Scientific Notebook Procedure NP 20-2.

11 EQUIPMENT

11.1 Measuring and Test Equipment (M&TE)

A calibration program will be implemented for the work described in this test plan in accordance with NP 12-1, "Control of Measuring and Test Equipment." This M&TE calibration program will meet the requirements in procedure NP 12-1 for: (1) receiving and testing M&TE; (2) technical operating procedures for M&TE; (3) the traceability of standards to nationally recognized standards such as those from the National Institute of Standards and Technology; (4) maintaining calibration records. In addition, NP 13-1 (Control of Samples and Standards) and SP 13-1 (Chain of Custody) identify requirements and appropriate forms for documenting and tracking sample possession. The spread-sheet and other computer based data handling will follow NP 9-1 (Analyses).

A variety of measuring and analytical equipment will be used for the work described in this test plan. This equipment includes that listed below, as well as equipment not yet purchased. A complete equipment list, including serial numbers, will be maintained in the scientific notebooks.

11.2 Weighing Equipment

Several balances may be used for this project. These include a Mettler AT-261 five-decimal place electronic balance, an ANC three-decimal place balance, and top loading balances and scales with maximum ranges of 2 to 30 kg. Balance calibration checks will be performed daily or prior to use (whichever is less frequent) using NBS-traceable weight sets, which, in turn, are calibrated by the SNL Mechanical Calibration Laboratory every two years. The balance calibration will be performed according to the procedure SP 12-1 (Use of Laboratory Balances and Scales). Balance calibration checks will be recorded in the current Balance Logbook, and a note indicating the page number of the calibration check and other pertinent information will be made within the appropriate Scientific Notebook.

11.3 Temperature Measuring Equipment

Mercury thermometers are used in the facility. A calibration check of these thermometers is performed annually against an ERTCO High Precision digital thermometer (model 4400), which is itself calibrated by the SNL Primary Standards Laboratory every year. The results of these calibration checks are recorded in the current Thermometer Logbook.

11.4 Liquid Measuring Equipment

Standard Laboratory Class A glassware (pipettes, volumetric flasks, etc.) will be used at all times. In addition, several adjustable Eppendorf pipettes are available for use in the laboratory. The calibration of pipettes will be checked routinely against a calibrated balance, and the results documented in the appropriate scientific notebook.

11.5 Other Analytical Equipment

11.5.1 Ovens and Furnace

Six Precision Telco Lab ovens are being used to hold samples at elevated temperatures. Temperature is monitored, maintained, and recorded on a daily schedule in the Oven Temperature logbook. A Fisher Isotemp furnace is used to determine Loss on Ignition (LOI).

11.5.2 pH Meters and Autotitrators

Solution pH may be measured using pH meters and/or autotitrators. A Mettler Model MA235 pH/Ion Analyzer and a Mettler Model DL25 Autotitrator will be used for this purpose. The range for all pH meters is 0.00 to 14.00. Electrodes will be calibrated before each use or daily (whichever is less frequent) with pH 4, 7, and/or 10 buffers manufactured by Fisher Scientific with unique lot numbers and expiration dates; traceable to the National Institute of Standards and Technology (NIST). The accuracy of the buffers is ± 0.01 pH units; buffer values will be adjusted for laboratory temperatures as per buffer instruction sheets if necessary. Calibration checks will be recorded in the scientific notebook. Measuring pH in concentrated brines is difficult, and a procedure will be developed to calibrate pH meters. The pH meters will be used according to the procedure SP 12-14 (Use of pH Meters and Electrodes). There is currently no procedure describing the use of the Mettler Model MA235 pH/Ion Analyzer and the Mettler Model DL25 Autotitrator. If this equipment is used, a procedure will be produced. Until that time, detailed procedure descriptions based on the instrument manual will be documented in laboratory notebooks.

11.5.3 Equipment for Chemical Analysis

Three instruments may be used for chemical analyses. The first is a Perkin Elmer Optima 3300 DV inductively-coupled plasma optical emission spectrometer (ICP-OES); the second is a Cary 300 UV-Visible Spectrophotometer; and the third, is a UIC, Inc. Carbon Analyzer, consisting of an acidification module, a furnace module, and a CO₂ coulometer. These instruments will be user-calibrated each time they are used and documented in their respective Logbook and in the scientific notebooks. The Carbon Analyzer will be used according to the procedure SP 12-2 (Use and Maintenance of the UCI, Inc. Model CM5014 CO₂ Coulometer, CM5130 Acidification Module and CM5120 Furnace Apparatus). If the two other pieces of equipment are used in this work, procedures will be generated. Until that time, detailed procedure descriptions based on the instrument manual will be documented in laboratory notebooks.

11.5.4 Equipment for Mineralogical, and Textural Characterization

The mineralogy and texture may be characterized using either an Olympus BX60 Polarizing Microscope or a JEOL JSM 5900LV scanning electron microscope (SEM). Calibration standards will be used to verify instrument magnification when these instruments are used. Bulk sample mineralogy will be determined using a Bruker AXS D-8 Advance X-Ray Diffractometer (XRD). A mineral standard will be run periodically to verify diffraction line positions. Calibration results will be documented in the instrument Logbooks and the scientific notebooks.

12 TRAINING

All personnel involved in the experiments described in this Test Plan will be trained and qualified for their assigned work. This requirement will be implemented through NP 2-1, “Qualification and Training.” Evidence of training to assigned NPs, SPs, this test plan, and any other required training will be documented through Form NP 2-1-2, Training Record. Specifically, the following NPs and SPs are applicable:

- NP 2-1 – “Qualification and Training”
- NP 6-1 – “Document Review Process”
- NP 9-1 – “Analyses”
- NP 12-1 – “Control of Measuring and Test Equipment”
- NP 13-1 – “Control of Samples and Standards”
- NP 17-1 – “Records”
- NP 20-2 – “Scientific Notebooks”
- SP 13-1 – “Chain of Custody”
- CPG-CHEM-TWD-2011-001-002 – “ES&H Standard Operating Procedure, Activities in the Sandia National Laboratories/Carlsbad Laboratory, Building NPHB (U).”

13 HEALTH AND SAFETY

The work proposed in this test plan will be performed in the Sandia National Laboratories – Carlsbad Program Group laboratory and will conform with SNL ES&H and follow the ES&H Standard Operating Procedure CPG-CHEM-TWD-2011-001-002, or the most current version. The hazards associated with the experiments proposed in this test plan can be broken down into three areas – electrical, chemical, and thermal. The concerns and mitigation strategies for each of these areas are described below.

13.1 Electrical

As with most active systems, there will be numerous leads run from power supplies and other electrical equipment in order to operate the experiments. All of the wiring will be covered/shielded such that there are no exposed, energized wires during normal operation of the system. All the electrical outlets will be grounded, and those within 6 feet of water sources are ground-fault-interrupt (GFI) protected. Some analytical instruments have built-in power supplies, generating voltages up to 60 kV (XRD). The power supply design prevents exposure of the users to an electrical hazard. No direct contact with energized circuits greater than 50 volts is expected to be encountered during the operation of this experiment.

13.2 Chemical

13.2.1 General Chemical Compounds

There are a number of chemical hazards associated with the experimentation described in this document. The hazards associated with each chemical are found in the MSDS files, which are kept in the laboratory.

The brines used during this experimentation are not a direct hazard for those performing the experimentation. But the disposal of the brines will be handled as part of the hazardous wastes stream, in accordance with the governing discharge into the Carlsbad sanitary sewer system, as currently described in the laboratory SOP (Wall, 2005), or the most current version. Secondary containment will be used to minimize the potential for unintended release of the brine in the chambers and benches.

13.2.2 Inert Gases

The work will involve the large quantities of inert gases (nitrogen and carbon dioxide) which will be used for the bulk of the exposure environment. The danger associated with these gases is exclusion of oxygen from the work area. While the risk is small due to the low flow rates involved (less than 4000 sccm (standard cubic centimeters per minute (i.e., milliliters per minute)) during normal operation), there could be unforeseen circumstances which lead to the release of larger quantities. In order to mitigate this hazard, oxygen level monitors as well as local ventilation will be utilized.

If one or several O₂ alarms are triggered, stay out of the area until the alarm shut off. If the alarm does not shut off the facility manager and laboratory manager shall be notified.

13.2.3 Hydrogen Sulfide

13.2.3.1 HAZARDS OF H₂S AND REGULATION

This section is not intended to replace the information provided by the H₂S material safety data sheet (MSDS); it merely highlights important information regarding H₂S(g). The reader is strongly encouraged to read the most recent H₂S MSDS.

H₂S(g) which will be used in several of the exposure chambers of this work. H₂S(g) is a colorless, highly toxic, flammable gas that is responsible for the foul odor of rotten eggs. This gas is slightly heavier than air, so it tends to concentrate at the bottom of poorly ventilated spaces. H₂S is considered highly toxic because it can poison different body systems; comparable to the effect of hydrogen cyanide, it blocks oxygen and stops cellular respiration. Additionally, H₂S can be difficult to detect without a proper alarm system, because its breathing may temporary paralyze the olfactory nerve making it impossible to smell the gas after an initial strong exposure. In case of poisoning, several treatments can be applied, among which the immediate inhalation of amyl nitrite or of pure oxygen. **Error! Reference source not found.** presents the symptoms observed after the exposure to different H₂S(g) concentrations.

Table 21. Symptoms Observed after Different H₂S Exposure

H ₂ S concentration exposure	Symptoms
0.0047 ppm	Recognition threshold; 50% of humans can detect the characteristic rotten egg odor of hydrogen sulfide
10 – 20 ppm	Slight eye irritation
50 –100 ppm	Eye damage
150 – 250 ppm	Olfactory nerve paralyzed after few inhalations; Sense of smell disappears
320 – 530 ppm	Pulmonary edema; Possible death
530 – 1000 ppm	Loss of breathing
800 ppm	Lethal concentration for 50% of humans after 5 minutes exposure (LC50)
> 1000 ppm	Immediate collapse after one breath

A variety of H₂S exposure limits have been established, from a Threshold Limit Value (TVL) of 10 ppm, as defined by the American Conference of Governmental Industrial Hygienists (ACGIH), to a PEL of 20 ppm, as defined from the Occupational Safety and Health Administration (OSHA) (ceiling).

H₂S(g) is also highly flammable, forming an explosive mixture with air, in concentration from 4.0 % (40,000 ppm) to 46 % (460,000 ppm). H₂S autoignites in the presence of oxygen at 260 °C.

13.2.3.2 SAFETY IMPLEMENTATION

A number of steps will be taken to minimize the hazards associated with this material. First, the gas will be supplied via a permeation device, rather than as a tank of compressed gas. This dramatically reduces the total quantity of the gas present in the laboratory, as well as limiting its release rate. The permeation device releases H₂S(g) at a known rate (usually expressed in ng/min); H₂S(g) flows at a known rate across the chamber containing the permeation tube, which in turn generates a gas stream of known H₂S(g) concentration. The gas

stream is diluted with a dry gas feed into the chamber in order to achieve the desired concentration.

In addition, the concentrations of hydrogen sulfide in the exposure chambers will be kept below 10 ppm (the current OSHA PEL is 20 ppm (ceiling) and the ACGIH TVL is 10 ppm). The H₂S(g) partial pressures applied to a system depends on the CO₂(g) partial pressures used. For example, if we use 350 and 1000 ppm CO₂(g) partial pressures in the chambers, we will use 1.3 and 3.6 ppm H₂S(g) partial pressures; this is based on the calculations presented in Section 7.2.4 (i.e. $\log(f_{\text{CO}_2} / f_{\text{H}_2\text{S}}) = 2.44$). If we use different CO₂(g) partial pressures, the H₂S(g) partial pressures will change accordingly. As with the carbon dioxide and nitrogen, the overall H₂S(g) flow rates will also be very low. The contaminant supply stream from the permeation tube will be below 1000 sccm, and the overall flow rate will be below 4000 sccm.

A series of barriers will be used to ensure that any gas which is released is vented safely. The H₂S(g) diluted stream will flow in the chambers containing the samples. The chambers outflow will be vented through a ventilation system, described in the next section. The H₂S(g) chambers will be kept in a temperature controlled–incubator. The incubator will be kept in a segregated room of the laboratory, where only H₂S–related work will be performed; this room will feature its own separated ventilation system, as described below.

The H₂S room ventilation system will be reviewed and approved by a SNL Industrial Hygienists, prior to beginning the actual experimental work. The ventilation system does not need to be explosion–resistant, because we will not use explosive concentrations of H₂S.

Several hydrogen sulfide monitors will be installed to warn of any H₂S release; the monitors will be connected to an automatic notification system (i.e. building alarm or automatic paging system), to ensure sufficient warning. The H₂S monitors will be placed as follows: one in the temperature controlled–incubator, one within the H₂S room but outside the incubator, one right outside the H₂S room, and one in the building corridor leading to the laboratory hosting the H₂S room.

The staff working with H₂S is required to wear the appropriate personal protection equipment (PPE):

- Eye protection: Wear splash resistant safety goggles with a faceshield.
- Clothing Wear appropriate chemical resistant clothing, such as cotton lab coat.
- Gloves: Wear appropriate chemical resistant gloves, made of materials such as butyl rubber, polyvinyl chloride, or neoprene.

Staff must ensure that H₂S is kept from incompatible materials, which are described in the H₂S MSDS.

H₂S will be stored and handled in accordance with all current regulations and standards, as described in the H₂S MSDS. It will be stored in a cool, dark, well-ventilated, and dry place, separated from incompatible materials.

All personnel engaged in working in the laboratory building will be notified of the presence and dangers of H₂S, as well as the measures to be taken in case of H₂S release and personnel injuries due to H₂S.

13.2.3.3 MEASURES AFTER ACCIDENTAL RELEASE

If one or several H₂S alarms are triggered:

1. All personnel must immediately evacuate the laboratory building,
2. The Carlsbad fire department is contacted by dialing 911,
3. The following people are notified: 6822 manager, facility manager, laboratory manager.

In case of inhalation, the person must leave the contaminated area immediately; preferably to go outside the building. The Carlsbad fire department is to be contacted by dialing 911. The person will receive medical attention.

If a staff member is found unconscious in or near the H₂S room of the laboratory, it will be assumed that it is due to H₂S exposure, even if no H₂S alarm was triggered. In such case:

1. All personnel must immediately evacuate the laboratory building,
2. The Carlsbad fire department is contacted by dialing 911,
3. The following people are notified: 6822 manager, facility manager, laboratory manager.
4. No SNL personnel will attempt to enter the H₂S room until it is declared safe by emergency response personnel and approved by 6822 manager, facility manager, and laboratory manager.

In case of skin contact, wash skin with soap and water for at least 15 minutes while removing contaminated clothing and shoes. Get medical attention, if needed. Thoroughly clean and dry contaminated clothing and shoes before reuse.

In case of eye contact, flush eyes with plenty of water for at least 15 minutes. Then contact Carlsbad fire department, dialing 911 to get immediate medical attention. If possible, have a co-worker contacting 911 while flushing the eyes.

In case of large amount ingestion, dial 911 to get immediate medical attention.

13.3 Thermal

There are two thermal hazards associated with this experimentation. The first is the H₂S to SO₂ converter used with the H₂S analyzer. The reactor itself is heated to a relatively high temperature (300 °C) in order to complete the conversion. The reactor is shielded within the equipment case, so there is no risk of accidental exposure during normal operation of the system. The second thermal hazard is represented by the heating mantles used for the gas saturation system. While the normal operating condition is below 40 °C, unforeseen circumstances may result in the temperature rising above this level. As such, signage clearly indicating the potential danger will be used.

13.4 Pressure

All pressure systems will be documented by Pressure Safety Data Packages (PSDPs), which have been reviewed by the Pressure Safety Advisor, as required by the SNL Pressure Safety Manual. (MN471000)

13.5 Readiness Review

Prior to begin the experimental work, a Readiness Review will be implemented, following the Readiness Review Process, as described in Section 13D of the SNL ES&H Manual.

14 PERMITTING/LICENSING

There are no special licenses or permit requirements for the work described in this Test Plan.

15 REFERENCES

- Arvidson, R.S., Ertan, I.E., Amonette, J.E. and Luttge, A. (2003) Variation in calcite dissolution rates: A fundamental problem? *Geochimica et Cosmochimica Acta* 67, 1623-1634.
- ASTM, 2003a. Standard Practice for Conducting Mixed Flowing Gas (MFG) Environmental Tests, ASTM B827-97, American Society for Testing and Materials (ASTM) International
- ASTM, 2003b. Standard Practice for Preparing, Cleaning, and Evaluating Corrosion Test Specimens, ASTM G1-2003, American Society for Testing and Materials (ASTM) International
- Babb, S.C., and C.F. Novak. 1997 and addenda. "User's Manual for FMT Version 2.3: A Computer Code Employing the Pitzer Activity Coefficient Formalism for Calculating Thermodynamic Equilibrium in Geochemical Systems to High Electrolyte Concentrations." Albuquerque, NM: Sandia National Laboratories. ERMS 243037.
- Bai, P., Zheng, S., Zhao, H., Ding, Y., Wu, J. and Chen, C. (2014) Investigations of the diverse corrosion products on steel in a hydrogen sulfide environment. *Corrosion Science* 87, 397-406.
- Barnes, H.L. and Langmuir, D. (1978) Geochemical prospecting handbook for metals and associated elements. Natl. Science Foundation Grant No. AER77-06511 AO2, Annual Report.
- Barrett, T.J., Anderson, G.M. and Lugowski, J. (1988) The solubility of hydrogen sulphide in 0-5 m NaCl solutions at 25° – 95°C and one atmosphere. *Geochimica et Cosmochimica Acta* 52, 807-811.
- Bourrié, G., Trolard, F., Génin, J.-M.R., Jaffrezic, A., Maître, V. and Abdelmoula, M. 1999. Iron control by equilibria between hydroxyl-Green Rusts and solutions in hydromorphic soils. *Geochimica et Cosmochimica Acta* 63, 3417-3427.
- Bourrié, G., Trolard, F., Refait, P. and Feder, F. 2004. A solid-solution model for Fe(II)-Fe(III)-Mg(II) green rusts and fougérite and estimation of their Gibbs free energies of formation. *Clays and Clay Minerals* 52, 382-394.
- Brush, L.H. 2005. "Results of Calculations of Actinide Solubilities for the WIPP Performance Assessment Baseline Calculations." Analysis report, May 18, 2005. Carlsbad, NM: Sandia National Laboratories. ERMS 539800.
- Brush, L.H., and Y.-L. Xiong. 2003. "Calculation of Organic Ligand Concentrations for the WIPP Compliance Recertification Application." Analysis report, April 14, 2003. Carlsbad, NM: Sandia National Laboratories. ERMS 527567.

- Bull Run Metal. 2004. TRU-Shield™ Lead-Lined Storage Containers. Sandia National Laboratories WIPP Record Center. ERMS 541709.
- Burns, T. 2005. “Estimated Containers in the Waste Isolation Pilot Plant (WIPP) Based on TWBID, Rev. 2.1, Data version 4.15.” Analysis Report, January 24, 2005. Carlsbad, NM. Los Alamos National Laboratory. ERMS 538501.
- Chivot, J. 2004. *Fonctions Thermodynamiques, Diagrammes de Solubilité, Diagramme E-pH des Systèmes Fe-H₂O, Fe-CO₂-H₂O, Fe-S-H₂O, Cr-H₂O et Ni-H₂O en Fonction de la Temperature*. Collection Sciences et Techniques. Châtenay-Malabry, France: Agence Nationale pour la Gestion des Déchets Radioactifs.
- Choppin, G.R., A.H. Bond, M. Borkowski, M.G. Bronikowski, J.F. Chen, S. Lis, J. Mizera, O. Pokrovsky, N.A. Wall, Y.X. Xia, and R.C. Moore. 2001. *Waste Isolation Pilot Plant Actinide Source Term Test Program: Solubility Studies and Development of Modeling Parameters*. SAND99-0943. Albuquerque, NM: Sandia National Laboratories.
- Cotsworth, E. 2004. Untitled letter with enclosure to R.P. Detwiler with third set of CRA comments and requests for additional information, September 2, 2004. Washington, DC: U.S. Environmental Protection Agency Office of Air and Radiation. ERMS 536771.
- Cramer, S.D. and J.P. Carter., 1980. “Corrosion in Geothermal Brines of the Salton Sea Known Geothermal Resource Area”, *Geothermal Scaling and Corrosion, Honolulu, Hawaii, April 4-5, 1979*. Eds. L.A. Casper and T.R. Pinchback. ASTM International, Philadelphia, PA.
- Crawford, B.A. 2005a. “Waste Material Densities in TRU Waste Streams from TWBID Revision 2.1 Version 3.13, Data Version D.4.15.” Analysis Report, April 13, 2005. Carlsbad, NM: Los Alamos National Laboratory. ERMS 539323.
- Crawford, B.A. 2005b. “Tables Containing Lead Data from TWBID Rev.2-1 D4.15”. Memorandum to J. Trone, October 20, 2005. Carlsbad, NM: Los Alamos National Laboratory. ERMS 541735.
- D'Appolonia Consulting Engineers, Inc. (1983). Brine reservoirs in the Castile Formation Waste Isolation Pilot Plant (WIPP) project, Southeastern New Mexico. Westinghouse Electric Corporation – Waste Isolation Division Carlsbad, NM., report TME 3153.
- Francis A.J., J.B. Gillow, and M.R. Giles. 1997. *Microbial Gas Generation under Expected Waste Isolation Pilot Plant Repository Conditions*. SAND96-2582. Albuquerque, NM: Sandia National Laboratories.
- Gascoyne, M. (2004). Hydrogeochemistry, groundwater ages and sources of salts in a granitic batholith on the Canadian Shield, southeastern Manitoba. *Applied Geochemistry* 19, 519–560.

- Garrels, R.M., and C.L. Christ. 1990. *Solutions, Minerals, and Equilibria*. Boston, MA: Jones and Bartlett.
- Gaucher, E.C., Tournassat, C., Pearson, F.J., Blanc, P., Crouzet, C., Lerouge, C. and Altmann, S. 2009. A robust model for pore-water chemistry of clayrock. *Geochimica et Cosmochimica Acta* 73, 6470-6487.
- Golden, J. 2004a. "Specification for the Fabrication of the Standard Waste Box." Carlsbad, NM: Washington TRU Solutions.
- Golden, J. 2004b. "Specification for the Fabrication of the Ten Drum Overpack." Carlsbad, NM: Washington TRU Solutions.
- Golden, J. 2005. "Specification for the Fabrication of the Standard Large Box 2 (SLB2)." Carlsbad, NM: Washington TRU Solutions.
- Gonzalez, J. L., Ramirez, R., Hallen, J. M. and Guzman, R. A. (1997) Hydrogen-induced crack growth rate in steel plates exposed to sour environments. *Corrosion* 53, 935-943.
- Hertelendy, N.A. 1984. *Rockwell Hanford Operations User's Manual for Remote Handled Transuranic Waste Container*. Rockwell International document no. RHO-RE-MA-7, September 1984.
- Huang, F., Li, X. G., Liu, J., Qu, Y. M., Jia, J. and Du, C. W. (2011) Hydrogen-induced cracking susceptibility and hydrogen trapping efficiency of different microstructure X80 pipeline steel. *Journal of Material Science* 46, 715-722.
- Jové Colón, C. F., Weck, P. F., Sassani, D. C., Zheng, L., Rutqvist, J., Steefel, C. I., Kim, K., Nakagawa, S., Houseworth, J., Birkholzer, J., Caporuscio, F. A., Cheshire, M., Rearick, M. S., McCarney, M. K., Zavarin, M., Benedicto-Cordoba, A., Kersting, A. B., Sutton, M., Jerden, J. L., Frey, K. E., Copple, J. M. and Ebert, W. L. *Evaluation of Used Fuel Disposition in Clay-Bearing Rock (FCRD-UFD-2014-000056)*, 2014, Sandia National Laboratories, SAND2014-18303 R: Albuquerque, New Mexico. 434 pp.
- Koyama, M., Akiyama, E. and Tsuzaki, K. (2012) Effect of hydrogen content on the embrittlement in a Fe-Mn-C twinning-induced plasticity steel. *Corrosion Science* 59, 277-281.
- Kubal, M., F. Panacek. 1995. "Potential-pH Diagram for Fe-H₂O-Citric Acid System," *British Corrosion Journal*. Vol 30, no. 4, 309-311.
- Lide, D.R. 2004-2005. *CRC Handbook of Chemistry and Physics*, 85rd edition. Boca Raton, FL: CRC Press
- Liu, M., Wang, J., Ke, W. and Han, E.-H. (2014) Corrosion behavior of X52 anti-H₂S pipeline steel exposed to high H₂S concentration solutions at 90 °C. *Journal of Material Science and Technology* 30(5), 504-510.

- Lüttge, A., Winkler, U. and Lasaga, A.C. (2003) Interferometric study of the dolomite dissolution: A new conceptual model for mineral dissolution. *Geochimica et Cosmochimica Acta* 67, 1099-1116.
- Mariner, P. E. 2007. *In-Drift Precipitates/Salts Model (ANL-EBS-MD-000045 Rev. 03)*. Sandia National Laboratories: Albuquerque: OCRWM Lead Laboratory for Repository Systems, 358 pp.
- Martell, A.E., R.M. Smith, and R.J. Motekaitis. 1998. *Critically Selected Stability Constants of Metal Complexes Database, Version 5.0*. College Station, TX: Texas A&M University Press.
- Molecke M.A. N.R. Sorensen, and G.G. Wicks. 1993. *Waste Isolation Pilot Plant Materials Interface Interactions Test: Papers Presented at the Commission of European Communities Workshop on In Situ Testing of Radioactive Waste Forms and Engineered Barriers*. SAND93-1055. Albuquerque, NM: Sandia National Laboratories.
- Munson, D.E., R.L. Jones, D.L. Hoag, and J.R. Ball. 1987. *Heated Axisymmetric Pillar Test (Room H): In Situ Data Report (February, 1985 - April, 1987), Waste Isolation Pilot Plant (WIPP) Thermal/Structural Interactions Program*. SAND87-2488. Albuquerque, NM: Sandia National Laboratories.
- NEA. 2013. *Chemical Thermodynamics of Iron, Part I*. Nuclear Energy Agency (NEA) volume 13a, NEA no. 6355. OECD Publications, 92130 Issy-les-Moulineaux, France.
- Nemer, M.B. and J.S. Stein. 2005. "Analysis Package for BRAGFLO: 2004 Compliance Recertification Application Performance Assessment Baseline Calculation." Carlsbad, NM: Sandia National Laboratory. ERMS 540527.
- Nemer, M.B., Stein, J.S., and Zelinski W. 2005. "Analysis Report for BRAGFLO Preliminary Modeling Results with New Gas Generation Rates Based Upon Recent Experimental Results." Carlsbad, NM: Sandia National Laboratories. ERMS 539437.
- Parker, V.B. and Khodakovskii, I.L. 1995. Thermodynamic properties of the aqueous ions (2+ and 3+) of iron and the key compounds of iron. *Journal of Physical and Chemical Reference Data* 24, 1699-1745.
- Pletcher, D., D. Sidorin, B. Hedges., 2005, "A Comparison of the Corrosion of Carbon and 13% Chromium Steels in Oilfield Brines Containing Acetate." *CO₂ Corrosion in Oil and Gas Production Symposium, Proceedings of the NACE Corrosion/2005 conference, held in Houston, TX, April 3-7, 2005*, National Association of Corrosion Engineers (NACE) International, Houston, TX, Paper no. 05301.
- Popielak, R.S., R.L. Beauheim, S.R. Black, W.E. Coons, C.T. Ellingson and R.L. Olsen. 1983. *Brine Reservoirs in the Castile Formation, Waste Isolation Pilot Plant Project, Southeastern New Mexico*. TME 3153. Carlsbad, NM: U.S. Department of Energy WIPP Project Office.

- Pourbaix, M. 1974. *Atlas of electrochemical Equilibria in Aqueous Solutions*. Houston, TX: National association of Corrosion Engineers.
- Qi, Y., Luo, H., Zheng, S., Chen, C., Lv, Z. and Xiong, M. (2014) Comparison of tensile and impact behavior of carbon steel in H₂S environments. *Materials and Design* 58, 234-241.
- Robie, R.A., B.S. Hemingway, and J.R. Fisher, 1979. *Thermodynamic properties of minerals and related substances at 298.15K and 1 bar (10⁵ pascals) pressure and at higher temperatures*. Geological Survey bulletin 1452, Washington: U.S. Govt. Print. Off. 456 pp.
- Robinson, K.L. 1996. "Preparing Synthetic Brines for Chemical Retardation and Transport Experiments." Unpublished technical operating procedure, TOP-544. Albuquerque, NM: Sandia National Laboratories.
- Roselle, G. T. (2009) *Iron and Lead Corrosion in WIPP-Relevant Conditions: Six Month Results*. Milestone Report, October 7, 2009. Carlsbad, NM: Sandia National Laboratories. ERMS 546084.
- Roselle, G. T. (2010) *Iron and Lead Corrosion in WIPP-Relevant Conditions: 12 Month Results*. Milestone report, October 14, 2010, Carlsbad, NM: Sandia National Laboratories. ERMS 554383.
- Roselle, G. T. (2011a) *Iron and Lead Corrosion in WIPP-Relevant Conditions: 18 Month Results*. Milestone report, January 5, 2011, Carlsbad, NM: Sandia National Laboratories. ERMS 554715.
- Roselle, G. T. (2011b) *Iron and Lead Corrosion in WIPP-Relevant Conditions: 24 Month Results*. Milestone report, May 3, 2011, Carlsbad, NM: Sandia National Laboratories. ERMS 555246.
- Saltykov, S.N., G.V. Makarov, E.L. Toroptseva, and Y.B. Filatova. 1989. "Anodic Behavior of White Iron Phases in Oxalic Media." *Protection of Metals*. Vol. 40, no. 1, 56-61.
- Sankarapavinasam, S., F. Pushpanaden, M.F. Ahmed. 1989. "Dicarboxylic Acids as Corrosion Inhibitors for Lead in HClO₄," *Bulletin of Electrochemistry*, Vol. 5, no. 5, 319-323.
- Sankarapavinasam, S., F. Pushpanaden, and M.F. Ahmed. 1989. "Hydrazine and Substituted Hydrazines as Corrosion Inhibitors for Lead in Acetic Acid," *British Corrosion Journal*. Vol. 24, no. 1, 39-42.
- Shukla, J., and K.S. Pitre. 2004. "Corrosion of Carbon Steel in Inhibited Acidic Medium: A New Voltammetric Approach," *Bulletin of Electrochemistry*. Vol. 20, no 7, 309-313.
- Snider, A.C. 2003. "Verification of the Definition of Generic Weep Brine and the Development of a Recipe for This Brine." Analysis report, April 8, 2003. Carlsbad, NM: Sandia National Laboratories. ERMS 527505.

- Stefánsson, A., Arnórsson, S. and Sveinbjörnsdóttir, Á.E. 2005. Redox reactions and potentials in natural waters at disequilibrium. *Chemical Geology* 221, 289-311.
- Stein, J.S. 2005. "Estimate of Volume of Brine in Repository That Leads to a Brine Release." Memorandum to L.H. Brush, April 19, 2005. Carlsbad, NM: Sandia National Laboratories. ERMS 539372.
- Telander, M.R., and R.E. Westerman. 1993. *Hydrogen Generation by Metal Corrosion in Simulated Waste Isolation Pilot Plant Environments*. SAND92-7347. Albuquerque, NM: Sandia National Laboratories.
- Telander, M.R., and R.E. Westerman. 1997. *Hydrogen Generation by Metal Corrosion in Simulated Waste Isolation Pilot Plant Environments*. SAND96-2538. Albuquerque, NM: Sandia National Laboratories.
- Turrero, M.J., A.M. Fernández, J. Peña, M.D. Sánchez, P. Wersin, P. Bossart, M. Sánchez, A. Melón, A. Yllera, A. Garralón, P. Gómez, P. Hernán (2006). Pore-water chemistry of a Paleogene continental mudrock in Spain and a Jurassic marine mudrock in Switzerland: sampling methods and geochemical interpretation. *J. Iberian Geol.* 32, 233–258.
- U.S. Congress. 1992. "WIPP Land Withdrawal Act." Public Law 102-579, 110 Stat. 2422, as amended by 104-201 (1996). Washington, DC: U.S. Congress.
- U.S. DOE. 2004. Title 40 CFR Part 191 Compliance Recertification Application for the Waste Isolation Pilot Plant, Vol. 1-8. DOE/WIPP 2004-3231. Carlsbad, NM: U.S. Department of Energy Carlsbad Field Office.
- Uhlig, H.H., and R.W. Revie. 1985. *Corrosion and Corrosion Control: An Introduction to Corrosion Science and Engineering*. New York, NY: John Wiley and Sons.
- Wall, D. 2005. ES&H Standard Operating Procedure, Activities in the Sandia National Laboratories/Carlsbad program Group Laboratory, Building NPHB (U). SP473548. Carlsbad, NM. Sandia National Laboratories.
- Wang, Z., R.C. Moore, A.R. Felmy, M.J. Mason, and R.K. Kukkadapu. 2001. "A Study of the Corrosion Products of Mild Steel in High Ionic Strength Brines," *Waste Management*. Vol. 21, 335–341.
- WIPP Performance Assessment Department. 2001a. "Design Document for PAPDB Version 1.00." Carlsbad, NM: Sandia National Laboratories. ERMS 518615.
- WIPP Performance Assessment Department. 2001b. "User's Manual for PAPDB Version 1.00." Carlsbad, NM: Sandia National Laboratories. ERMS 518617.
- Wolery, T. J. and Jové-Colón, 2007. *Qualifications of Thermodynamic Data for Geochemical Modeling of Mineral–Water Interactions in Dilute Systems (ANL-WIS-GS-000003 Rev.*

- 01). Sandia National Laboratories: Albuquerque; OCRWM Lead Laboratory for Repository Systems, 412 pp.
- Woolsey, G., 2005. "Lead Lined Drum Projections." Memorandum to N. Wall, October 20, 2005. Carlsbad, NM: Washington TRU Solutions. ERMS 54658.
- Xia, Y., L. Rao, D. Rai, and A.R. Felmy. 2001. "Determining the Distribution of Pu, Np, and U Oxidation States in Dilute NaCl and Synthetic Brine Solutions," *Journal of Radioanalytical and Nuclear Chemistry*. Vol. 250, no. 1, 27–37.
- Younes, C. M., Steele, A. M., Nicholson, J. A. and Barnett, C. J. (2013) Influence of hydrogen content on the tensile properties and fracture of austenitic stainless steel welds. *International Journal of Hydrogen Energy* 38, 4864-4876.
- Zheng, S., Zhou, C., Chen, X., Zhang, L., Zheng, J. and Zhao, Y. (2014a) Dependence of the abnormal protective property on the corrosion product film formed on H₂S-adjacent API-X52 pipeline steel. *International Journal of Hydrogen Energy* 39, 13919-13925.
- Zheng, Y., Brown, B. and Nešić, S. (2014b) Electrochemical study and modeling of H₂S corrosion of mild steel. *Corrosion* 70, 351-365.

This work of authorship was prepared as an account of work sponsored by an agency of the United States Government. Accordingly, the United States Government retains a nonexclusive, royalty-free license to publish or reproduce the published form of this contribution, or allow others to do so for United States Government purposes. Neither Sandia Corporation, the United States Government, nor any agency thereof, nor any of their employees makes any warranty, express or implied, or assumes any legal liability or responsibility for the accuracy, completeness, or usefulness of any information, apparatus, product, or process disclosed, or represents that its use would not infringe privately-owned rights. Reference herein to any specific commercial product, process, or service by trade name, trademark, manufacturer, or otherwise does not necessarily constitute or imply its endorsement, recommendation, or favoring by Sandia Corporation, the United States Government, or any agency thereof. The views and opinions expressed herein do not necessarily state or reflect those of Sandia Corporation, the United States Government or any agency thereof.

Sandia National Laboratories is a multi-program laboratory managed and operated by Sandia Corporation, a wholly owned subsidiary of Lockheed Martin Corporation, for the U.S. Department of Energy's National Nuclear Security Administration under contract DE-AC04-94AL85000.

Parties are allowed to download copies at no cost for internal use within your organization only provided that any copies made are true and accurate. Copies must include a statement acknowledging Sandia Corporation's authorship of the subject matter.